SEDIMENTATION OF FINE SIC PARTICLES DURING LIQUID PROCESSING OF Al/SiC COMPOSITES

SEDIMENTATION OF FINE SIC PARTICLES DURING LIQUID PROCESSING OF Al/SiC COMPOSITES

Ву

Kwame Owusu-Boahen, B.Sc., M.Sc.

A Thesis

Submitted to the School of Graduate Studies in partial fulfilment of the Requirements for the Degree of Master of Engineering.

McMaster University

March 1994

MASTER OF ENGINEERING (1994) McMASTER UNIVERSITY

(Materials Engineering)

Hamilton, Ontario

TITLE: Sedimentation of Fine Silicon Carbide Particles During Liquid

Processing of Al/SiC Composites

AUTHOR: Kwame Owusu-Boahen

B.Sc. (University of Science and Technology, Kumasi, GHANA)

M.Sc. (Technion - Israel Institute of Tchnology, Haifa, ISRAEL)

SUPERVISOR: Professor G.A. Irons

NUMBER OF PAGES: xix, 113

ABSTRACT

The settling of fine SiC particles (2.5 - 20 vol%) during liquid processing of Al/SiC composites has been studied by an electrical resistance technique. Settling rate data show that the settling of fine SiC in aluminum does not obey Richardson-Zaki relation, characteristic of non-flocculated systems. Rather the data reveal two distinct settling regimes, a (non-linear) rapidly decreasing settling rate regime (of higher than Richardson-Zaki predicted rates) and a linear (below Richardson-Zaki predicted rates) regime. The final settled bed in the aluminum-fine SiC with a concentration of only 0.28 volume fraction SiC, lacks the compactness of random close-packed arrangement (0.62 volume fraction), characteristic of non-flocculated systems. The system, in essence, cannot be non-flocculating and the suspicion is that there is an appreciable level of flocculation or clustering among these fine particles. At low SiC volume fractions (where settling rates are higher than predictions of the Richardson-Zaki relation) the flocs/aggregates probably settle individually. At high volume fractions of SiC (where settling is slower than expected), it is most probable that the aggregates settle together as a coherent network structure.

ACKNOWLEDGEMENT

The author wishes to express his sincere gratitude to his supervisor, Prof. G.A. Irons for his invaluable guidance, advice and inspiration during the course of this work.

Financial support of the Canadian International Development Agency (CIDA) and the Natural Science and Engineering Research Council of Canada (NSERC), and material donation from ALCAN International are gratefully acknowledged.

A word of thanks to Dr. G.S. Hanumanth for the informal discussions of the work and to Mr. O. Kelly for his help during the experimental work.

Finally, thanks go to all, far and near, who in diverse ways helped to bring this work to a successful conclusion.

TABLE OF CONTENTS

	LIST OF SYMBOLS	viii
	LIST OF FIGURES	xi
	LIST OF TABLES	xix
CHAPTER 1	INTRODUCTION	1
CHAPTER 2	LITERATURE REVIEW	3
2.1	Sedimentation in an Aqueous Systems	3
2.1.1	The Richardson-Zaki Equation	7
2.2	System of Flocculated Particles	8
2.2.1	van der Waals Interaction	8
2.2.2	Electrical Interaction	11
2.2.3	Combined Interaction	12
2.2.4	Kinetics of Flocculation	14
2.2.4.1	Perikinetic Flocculation	15
2.2.4.2	Ortokinetic Flocculation	15
2.2.4.3	Differential Settling	18
2.2.4.4	Collision Efficiency	18

2.2.5	Settling of Flocculated Systems	22
2.2.5.1	Dilute Range	22
2.2.5.2	Beyond Dilute Range	27
2.2.5.3	Floc Volume Fraction and Final Sediment	33
2.3	Particle Sedimentation in Alloy system	36
CHAPTER 3	EXPERIMENTAL PROCEDURE	40
3.1	Apparatus and Materials	40
3.2	Experimental Procedure	42
CHAPTER 4	RESULTS AND ANALYSIS	46
4.1	Resistance Versus Time Graphs	47
4.1.1	2.5 vol% SiC MMC	47
4.1.2	5 vol% SiC MMC	47
4.1.3	7.5 vol% SiC MMC	48
4.1.4	10 vol% SiC MMC	49
4.1.5	15 vol% SiC MMC	50
4.1.6	20 vol% SiC MMC	51
4.2	Sedimentation Patterns	51
43	Plot of Settling Rate Data	53

4.4	Chemical Analysis	55
CHAPTER 5	DISCUSSION	87
5.1	The Probe	87
5.2	Interface Position versus Time Curves	89
5.3	Settling Rate Data	91
5.4	Modelling of Settling of Fine SiC Particles in	
	Aluminum	94
5.5	Future Work	95
5.5.1	Settling Rates	96
5.5.2	The Transition Layer	96
CHAPTER 6	SUMMARY AND CONCLUSIONS	98
REFERENCES		99
APPENDIX I	Micrographs of MMCs	101
APPENDIX II	•	107
II.1	Poiseuile Equation	107
II.2	Kozeny-Carman Equation	110

LIST OF SYMBOLS

A	Hamaker constant (J)
C_{ij}	ratio of volume concentration of component i to component j.
	$C_{AS} = \theta_A/\theta_S$; $C_{AF} = \theta_A/\theta_F$; $C_{SF} = \theta_S/\theta_F$
D_0	diameter of container tube (m)
\mathbf{D}_{y}	yield diameter (m), defined by equation (42)
d	average diameter (m)
е	elementary charge (C)
F	Force (N)
G	shear rate (s ⁻¹)
g	acceleration due to gravity (9.8 m/s ²)
J	collision frequency (s ⁻¹)
k_0	shape factor in Konezy-Carman equation.
L_{P}	tortuosity factor
n	number of particles
P	power input (eg., in stirred vessel)
p	pressure (N/m²)
r _H	pore hydraulic radius
Т	absolute temperature (K)

time (s) t interaction energy (J) V velocity (m/s) v Stokes velocity (m/s) v_{o} spatial coordinate (m) X Z height of slurry interface (m) initial height of column (m) Z_{0} yield height (m), defined by equation (43) Z_{y} z valency of ion

Greek Symbols

α_0	limiting orthokinetic collision frequency (s ⁻¹)
β	friction coefficient (kg/m ³ s)
γ	dimensionless surface potential function
Δ	small change
ζ	zeta surface potential function
θ	volume fraction
κ	Debye-Huckel parameter or reciprocal double layer thickness (m ⁻¹)

```
\mu viscosity (kg/m s)

\rho density (kg/m³)

\sigma_y compressive strength of aggregate network (N/m²)

\tau_y yield stress (N/m²), for a plastic suspension, \tau \rightarrow \tau_y as shear rate \rightarrow 0.

\epsilon void fraction

\epsilon dielectric constant of suspending medium

Subscripts
```

Α aggregate E electrical floc F friction f L liquid pore p S solids Т total U underneath

W wall

LIST OF FIGURES

Figure 2.1	Typical particle sedimentation behaviour (a) Physical	4
	appearance, (b) Height of interfaces as a function of time.	
Figure 2.2	The characteristic velocity as a function of particle fraction v_{AB} , v_{BC} and v_{CD} are velocities of the interface between the regions A and B, B and C, and C and D, respectively, as described in Figure 2.1.	6
Figure 2.3	Model for the interaction of two particles at close approach (d< <a). between="" d,="" distance="" is="" of="" particles.<="" separation,="" shortest="" surface="" td="" the=""><td>10</td></a).>	10
Figure 2.4	Potential energy diagram for the interaction of particles. The van der Waals attraction, V_A , electrical repulsion, V_E , and the total energy, V_T , are shown as a function of particle separation, d.	13
Figure 2.5	Model for orthokinetic collision in uniform, laminar shear.	16

Figure 2.6	Orthokinetic collision efficiency as function of particle size at	21
	various values of surface potential, γ_0 , for hydrosol, $A = 10^{-9}$	
	J, $\mu = 0.001$ Pa.sec., $\varepsilon = 78$, $\lambda = 100$ nm, $\kappa = 0.1$ nm ⁻¹ , and G	
	$= 2 \sec^{-1} [21].$	
Figure 2.7	Plot of floc diameter and floc effective density.	23
Figure 2.8	Floc-aggregate structural model.	24
Figure 2.9	Control volume and height-density relationships. Left; Height	26
	vs density profile at time t. Right; Settling tube showing	
	control volume. extending from the interface downward whose	
	density is constant.	
Figure 2.10	Correlation of settling rates by equation (44) for kaolin-water	30
·•	system.	
Figure 2.11	Plot of v _a '/θ _a against θ _a for water-kaolin system [22].	32

Figure 2.12	X-ray data of Gaudin and Fuerstenau [23] showing density of	3.5
	final settled bed of a flocculated (aqueous) system. The lower	
	the ratio I/I ₀ , the denser the dispersion at the particular height.	
Figure 2.13	Position of the clarified front and the rising sediment interface	35
	as a function of time during sedimentation of (a) 0.10 and (b)	
	0.20 volume fraction composite.	
Figure 3.1	Schematic diagram of the experimental apparatus.	44
Figure 3.2	Schematic diagram of the four-point probe.	45
Figure 4.1	Variation of resistance with nominal SiC volume fraction.	58
Figure 4.2	Variation of resistance with time at 5 cm below the melt	59
	surface.	
Figure 4.3	Variation of resistance with time at 5 cm below the melt	60
	surface for 2.5 vol% SiC MMC.	

Figure 4.4	Variation of resistance with time at 15 cm below the melt surface for 5 vol% SiC MMC.	61
Figure 4.5	Variation of resistance with time at 5 cm below the melt surface for 5 vol% SiC MMC.	62
Figure 4.6	Variation of resistance with time at 10 cm below the melt surface for 5 vol% SiC MMC.	63
Figure 4.7	Variation of resistance with time at 16 cm below the melt surface for 5 vol% SiC MMC.	64
Figure 4.8	Variation of resistance with time at 6 cm below the melt surface for 7.5 vol% SiC MMC.	65
Figure 4.9	Variation of resistance with time at 12 cm below the melt surface for 7.5 vol% SiC MMC.	66
Figure 4.10	Variation of resistance with time at 17 cm below the melt surface for 7.5 vol% SiC MMC.	67

Figure 4.11	Variation of resistance with time at 6 cm below the melt surface for 10 vol% SiC MMC.	68
Figure 4.12	Variation of resistance with time at 12 cm below the melt surface for 10 vol% SiC MMC.	69
Figure 4.13	Variation of resistance with time at 17 cm below the melt surface for 10 vol% SiC MMC.	70
Figure 4.14	Variation of resistance with time at 6 cm below the melt surface for 15 vol% SiC MMC.	71
Figure 4.15	Variation of resistance with time at 12 cm below the melt surface for 15 vol% SiC MMC.	72
Figure 4.16	Variation of resistance with time at 18 cm below the melt surface for 15 vol% SiC MMC.	73
Figure 4.17	Variation of resistance with time at 7 cm below the melt surface for 20 vol% SiC MMC.	74

Figure 4.18	Variation of resistance with time at 13 cm below the melt surface	75
	for 20 vol% SiC MMC.	
Figure 4.19	Variation of resistance with time at 19 cm below the melt surface for 20 vol% SiC MMC.	76
Figure 4.20	Time to pass from the initial volume fraction region B, to the clarified region A, for 2.5 vol% SiC MMC.	77
Figure 4.21	Time to pass from the initial volume fraction region B, to the clarified region A, for 5 vol% SiC MMC.	78
Figure 4.22	Time to pass from the initial volume fraction region B, to the clarified region A, for 7.5 vol% SiC MMC.	79
Figure 4.23	Time to pass from the initial volume fraction region B, to the clarified region, A for 10 vol% SiC MMC.	80
Figure 4.24	Time to pass from the initial volume fraction region B, to the clarified region A, for 15 vol% SiC MMC.	81

Figure 4.25	Time to pass from the initial volume fraction region B, to the	82
	clarified region A, for 20 vol% SiC MMC.	
Figure 4.26	Plot of floc volume fraction against particle (SiC) volume fraction.	83
Figure 4.27	Plot of settling rate according to equation (49).	84
Figure 4.28	Comparison of nominal, probe and chemical estimations of SiC volume fractions in the MMCs.	85
Figure 4.29	Variation of SiC volumetric fraction (by chemical analysis) with time for 15 vol% SiC MMC.	86
Figure I.1	Micrograph of 2.5 vol% SiC MMC (× 64).	101
Figure I.2	Micrograph of 5 vol% SiC MMC (× 64).	102
Figure I.3	Micrograph of 7.5 vol% SiC MMC (× 64).	103

Figure I.4	Micrograph of 10 vol% SiC MMC (× 64).	104
Figure I.5	Micrograph of 15 vol% SiC MMC (× 64).	105
Figure I.6	Micrograph of 20 vol% SiC MMC (× 64).	106
Figure I.1	Cylinder of radius r, moving inside a slightly larger cylinder of radius $r + \delta r$.	108

LIST OF TABLES

Table 1	Relationship between volumetric fraction and weight of SiC	4]
	in 23.4 kg of aluminum.	
Table 2.	Data for estimation of floc volume fraction in 7.5, 15 and 20	54
	vol% SiC MMCs.	
Table 3.	SiC volumetric fractions (by chemical analysis) after passage	57
	of clarification front at various positions approximately in	
	melt heights below surface.	
T-11- 4	A Si Constitutation frontian (by chemical analysis) in the	57
Table 4.	Average SiC volumetric fraction (by chemical analysis) in the	٥,
	final sediment of 7.5, 15 and 20 vol% SiC MMCs.	

CHAPTER 1

INTRODUCTION

The need to improve upon the strength-weight ratio of materials in aerospace, automobile and many other applications, has led to ingenious ways by which light ductile metals, can be reinforced with hard ceramics, to produce what is known as metal matrix composites (or MMCs). The improved mechanical properties of MMCs have been researched extensively and documented elsewhere [1-3]. Comparatively, there has been little research on the fundamentals of MMC processing.

Where very high strengths and modulus are required for specialized applications, especially at temperatures of about 100°C and above, aligned fibre reinforcements or laminated sheets has been used to obtain superior, yet highly directional properties. For more general applications, on the other hand, MMCs are reinforced with discontinuous chopped fibres, whiskers, platelets or particles, which offer essentially isotropic properties with improved strengths and stiffness compared to the unreinforced alloys. Several processing routes are used in the production of MMCs. Composites for more general use are produced by a method involving the stirring of ceramic particles into a metal melt, which is the simplest and potentially cheapest means by which MMCs may be produced. ALCAN has commercialized a process, the DUR ALCAN, which has an annual capacity of about a million pounds (450 tons), based on this technique. By this process, SiC or alumina is added to aluminum in the molten form [4], and is currently the method used in the fabrication of (MMC) automobile brake rotors.

- Despite its apparent simplicity, the process has three major inherent problems.
- 1. Most particles are not easily wetted by the molten metal [5].
- 2. Particles either float or sink in the melt depending on the particle-to-liquid density ratio.
- 3. The viscosities of the mixture are very high and also time-and shear ratedependent [6].

The subject of sedimentation in aqueous systems has received quite extensive studies in the field of chemical engineering. Knowledge on the subject of settling and sedimentation of particles in liquid alloy systems, however, is very sketchy. The first documented study of the problem of SiC sedimentation during MMC processing was in 1990 by Lafreniere and Irons [7], in which the settling and sedimentation of coarse SiC particles (90 μ m) in aluminum melt was investigated. The current research is a follow up of their (Lafreniere and Irons) work, but this time, using finer SiC particles (14 μ m) characteristic of industrial MMC production.

CHAPTER 2

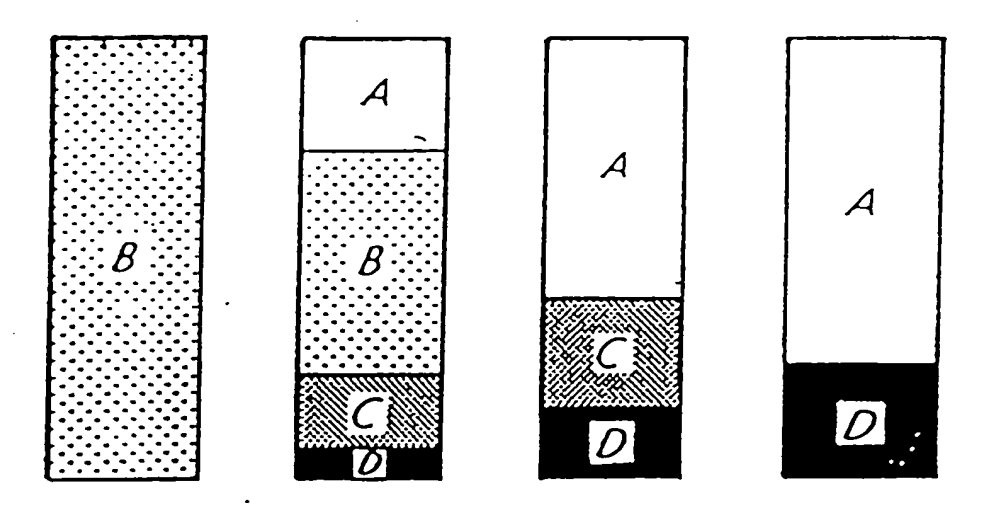
LITERATURE REVIEW

2.1 SEDIMENTATION IN AN AQUEOUS SYSTEM

The terminal velocity of a single spherical particle falling in an infinite viscous fluid expressed by the well-known Stokes equation is,

$$v_0 = \frac{d_s^2(\rho_s - \rho_L)g}{18\mu_L} \tag{1}$$

The subject of settling and sedimentation of particles in aqueous systems has received much attention in the field of chemical engineering for some time now. A qualitative description of such a process is given below (Figure 2.1). Initially, the column contains a two-phase mixture B. As settling of the particles takes place, clear liquid A begins to form at the top and a dense sediment D at the bottom. Between B and D, there is often a region of non-uniform density, labelled C. If the particles are of fairly uniform size, there is a sharp discontinuity between the layers A and B, and this moves with the velocity of the settling particles. There may or may not be a discontinuity between B and C. Eventually, the upper discontinuity meets the lower one, and the region B disappears. Thereafter, there is a slow compaction of regions C and D until sediment reaches its maximum density throughout.



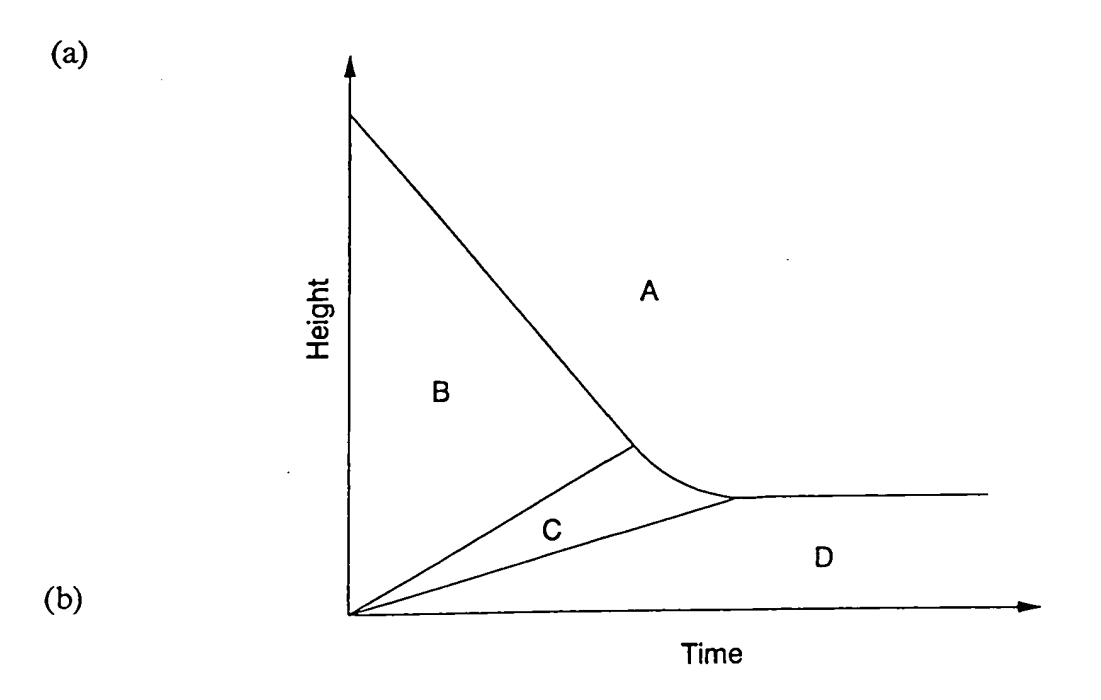


Figure 2.1 Typical particle sedimentation behaviour. (a) Physical appearance, (b) Height of interfaces as a function of time.

When the concentration of the particles (uniformly sized) is very small and their distance apart is large compared to their size, the speed of fall v, obtained by Einstein and many other authors gives,

$$v = v_0 (1 - \alpha \theta_s) \tag{2}$$

where $\alpha = 2.5$ for hard spheres. At relatively large concentrations of particles, on the other hand, the settling of a particle will be influenced by the presence of other particles in the suspension leading to what is commonly known as hindered settling. Robinson [8], Steinour [9] and Hawksley [10], all found that, the settling velocity v, of the particles (during hindered settling) was,

$$v - v_0 \phi(\varepsilon)$$
 (3)

thus, the deviation from the Stokes velocity is a function of the free area ε , available for the flow of the displaced liquid.

Kynch's theory of sedimentation [11] was based on the single assumption that the settling velocity of the particles at any point depended only on the local concentration of particles. From the continuity equation, he deduced that a particular value of concentration is propagated upwards through the dispersion and that the speed of fall of any surface is that of the particles in it. The theory further predicts the presence of discontinuities (or shocks) in the particle concentration where there is a sudden finite change of concentration at certain levels. This model basically ignores the sediment rising from the bottom. However, in spite of this extreme simplification, the method has historically been used in industries with success. Therefore it must represent some sort of reasonable approximation of the real case.

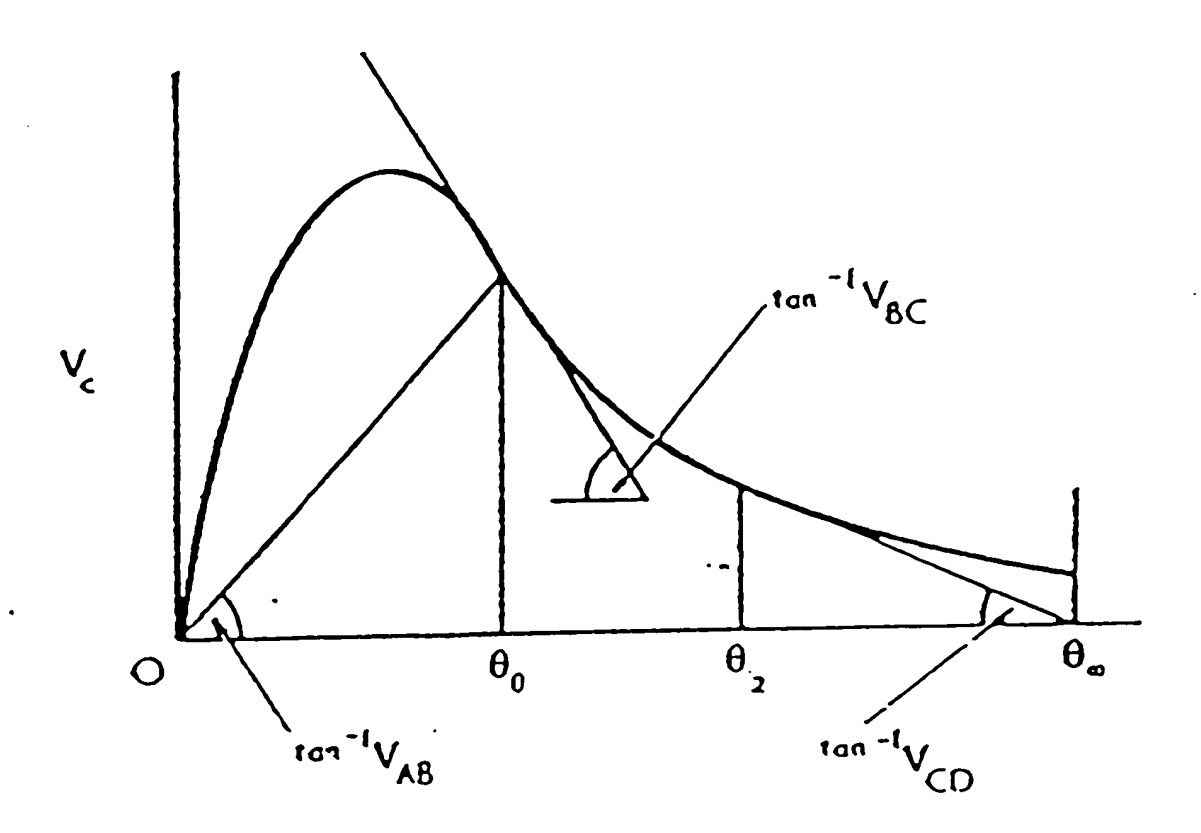


Figure 2.2 The characteristic velocity as a function of the particle fraction. v_{AB} , v_{BC} and v_{CD} are velocities of the interfaces between the regions A and B, B and C, and, C and D, respectively, as described in Figure 2.1.

A graphical method of analyzing sedimentation was developed by Wallis [12] based on the idea of continuity waves and shocks, and a characteristic velocity $v_{\rm c}$ defined by,

$$v_C - v\theta_S(1 - \theta_S) \tag{4}$$

A single plot of the characteristic velocity versus the solid fraction, θ_s , together with the initial concentration allow the sedimentation behaviour of any initially uniform two-component system to be predicted. This characteristic curve (shown in Figure 2.2) must be determined experimentally and the approach makes no reference to the forces acting in the system.

2.1.1 The Richardson-Zaki Equation

Richardson and Zaki [13] offered perhaps the most useful study. From the Stokes relation in equation (1), they deduced by dimensional analysis, an empirical relation,

$$v = v_0 \theta_L^n = v_0 (1 - \theta_S)^n \tag{5}$$

It has to be stressed that the relation can be applied satisfactorily to systems of non-flocculated particles and several authors have obtained values of n between 4.6 and 5 for such systems.

2.2 SYSTEMS OF FLOCCULATED PARTICLES

Flocculation occurs only if particles (1) collide with each other and (2) can adhere when brought together by collision. To a large extent these processes, termed transport and attachment steps may be regarded as independent and can be treated separately. When two particles approach each other, several types of interactions come into play which have a major effect on the flocculation process. The two most familiar kinds of interaction are the van der Waals attraction and electrical repulsion which form the basis of the DLVO (Deryagin & Landu [14] and Verwey & Overbeek [15]) theory of colloidal stability. The other interactions are conveniently termed "extra" or "non-DLVO" interactions. Practically all these interactions are of quite a short range, almost never extending over distances greater than the size of the particles.

2.2.1 van der Waals Interaction

The universal van der Waals attractive forces between atoms and molecules also operate between macroscopic objects. Without these forces, flocculation of particles would usually be prevented by the hydrodynamic interaction. The interaction between macroscopic bodies arise from spontaneous electric and magnetic polarizations, giving a fluctuating electromagnetic field within the media and in the gap between them. For two spheres of radii a_1 and a_2 , separated by a distance d (see figure 2.3), the interaction energy at close approach (d << a) is given by,

$$V_A - A_{12} \frac{a_1 a_2}{6d(a_1 + a_2)} \tag{6}$$

where V_A is the interaction energy between the two spheres and A_{12} is the Hamaker [16] constant for media 1 and 2, which the spheres are composed. For identical spheres, of radius, a_1 , the result is simply,

$$V_A - A_{11} \frac{a_1}{12d} \tag{7}$$

The above result applies to interaction of media across a vacuum. For interaction through a liquid medium the Hamaker constant is modified and for media 1 and 2 separated by medium 3, we have,

$$A_{122} - A_{12} + A_{33} - A_{13} - A_{23} \tag{8}$$

A₁₃ is the Hamaker constant for materials 1 and 3, etc., given by,

$$A_{13} - (A_{11}A_{33})^{1/2} (9)$$

Depending on the relative magnitudes of the individual constants, the presence of a third medium can significantly reduce the interaction. For similar materials, 1, interacting across a medium 3,

$$A_{131} - (A_{11}^{1/2} - A_{33}^{1/2})^2 \tag{10}$$

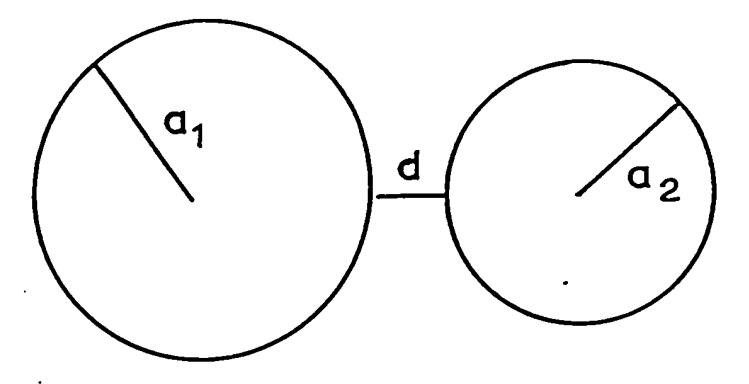


Figure 2.3 Model for the interaction of two particles at close approach (d << a). The separation, d, is the shortest distance between the surface of the particles.

This led Hamaker to conclude that van der Waals interaction between similar materials would always be attractive.

2.2.2 Electrical Interaction

Most particles in a dispersion are charged. In such a case, the charge on a particle's surface is balanced by an equivalent number of oppositely charged counterions in the liquid medium. The distribution of ions around the charged particles is not uniform and gives rise to an electrical double layer. Counterions close to the particles surface constitute the *Stern layer* and the remainder is distributed more broadly in a *diffuse layer*.

When two charged particles approach each other, their diffuse layers overlap and in the case of identical particles, a repulsion is experienced between them. The precise way in which the double layers respond to each other depends on a number of factors the most important of which is the surface potential of the particles. A simple relation expressing the relation between this interaction and the various factors is given by,

$$V_E - 64 \frac{a_1 a_2}{a_1 + a_2} \pi \epsilon \left(\frac{kT}{ze}\right)^2 \gamma_1 \gamma_2 \exp(-\kappa d) \tag{11}$$

The terms γ_1 and γ_2 are dimensionless functions of the surface potentials (taken as zeta functions here): $\gamma_1 = \tanh(ze\zeta_1/4kT)$, etc. The pre-exponential term depends on the zeta function of the particles and is always positive (repulsion) if the potentials are of like signs and negative (attraction) if they are of opposite signs. For identical particles the equation reduces to,

$$V_E - 32\pi \epsilon a_1 \left(\frac{kT}{ze}\right)^2 \gamma_1 \exp(-\kappa d), \qquad (12)$$

and for small values of surface potential (or ζ), this simplifies further to,

$$V_F = 2\pi \epsilon a_1 \zeta^2 \exp(-\kappa d) \tag{13}$$

showing the influence of ζ more clearly.

2.2.3 Combined Interaction

If it is assumed that the contributions of the van der Waals and electrical interactions are additive, they may simply be combined to give the total interaction. Then for identical spherical particles, combining equations (7) and (12) gives an expression for the total interaction energy V_T as,

$$V_T = 32\pi \epsilon a \left(\frac{kT}{ze}\right)^2 \gamma^2 \exp(-\kappa d) - A \frac{a}{12d}$$
 (14)

In Figure 2.4, the repulsion and attractive energies are plotted against separation distance, as the total interaction. The plot is a classical case of a situation where the repulsion outweighs the attraction over the important range of separation. An important feature of the plot is that there is a potential energy barrier and two colliding particles would need to have sufficient energy to overcome this barrier for an aggregate to be formed. In principle, van der Waals attraction is infinitely strong on contact of particles and the primary minimum should be of infinite depth. However, short range

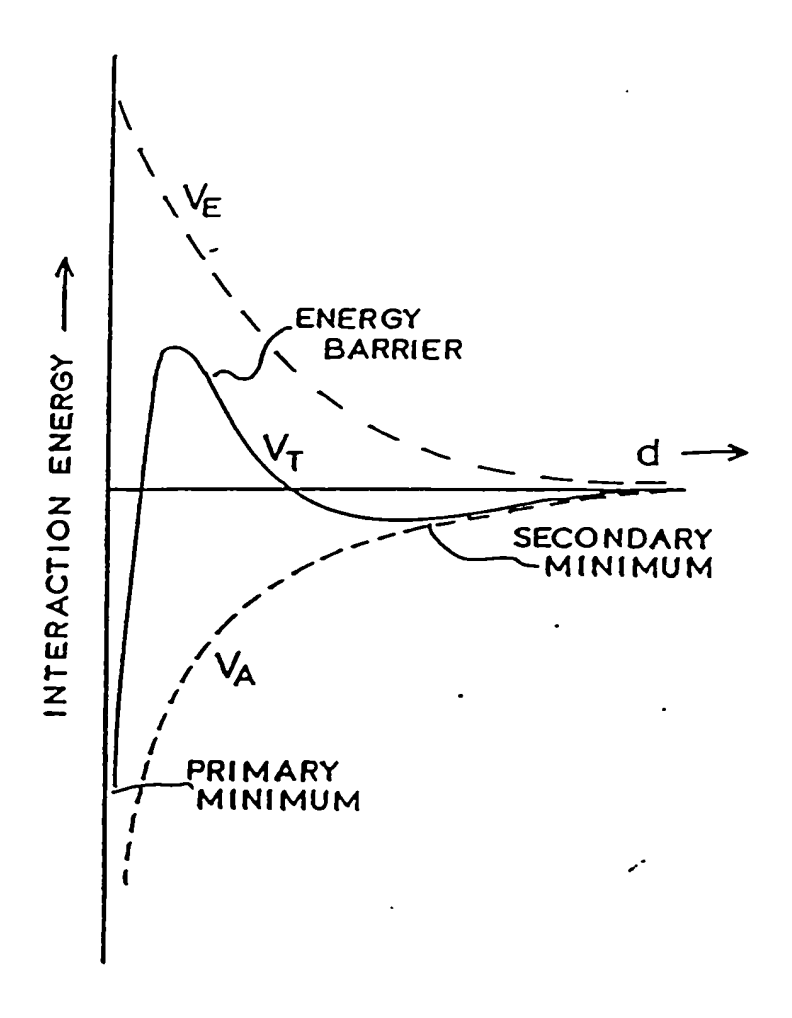


Figure 2.4 Potential energy diagram for the interaction of particles. The van der Waals attraction, V_A , electrical repulsion, V_E , and the total energy, V_T , are shown as a function of particle separation, d.

effects limit the closeness of approach and hence the depth of the primary minimum may in some cases, be quite shallow.

Another important feature of the plot is a secondary minimum. This is due to the different dependencies of the electrical and van der Waals interactions, with the result that attraction must outweigh repulsion at some separation distance. So that, in principle flocculation could occur without the particles coming into close contact. In practice this effect will be most significant with particles that are not too small. With small particles the depth of the minimum will be limited by the relative weak van der Waals attraction.

2.2.4 Kinetics of Flocculation

It is convenient to think of a dispersion as initially of identical particles, which after a period of aggregation will contain aggregates of various sizes. The rate of flocculation will depend on the various particle transport mechanisms, namely;

- 1. Brownian diffusion (perikinetic flocculation)
- 2. Fluid motion (orthokinetic flocculation)
- 3. Differential settling.

2.2.4.1 Perikinetic Flocculation

Particles in suspension are subject to random displacement (Brownian motion) due to thermal energy of the system. As a result particles will collide from time to time which may result in flocculation. The rate of flocculation resulting from this mode of particle transport is quite slow for fairly dilute suspensions. Smoluchowski [17] has shown that for identical particles the rate of decline of the total particle concentration resulting from floc formation is independent on the particle size, thus;

$$-\frac{dn_T}{dt} - (\frac{4kT}{3\mu})n_T^2 - k_F n_T^2$$
 (15)

where k_F (= 4kT/3 μ) is known as the flocculation rate constant. This is due to the fact that as particle size increases, particle diffusion decreases but collision radius increases. The two opposing effects on collision rate, however, exactly balance for equal particles.

2.2.4.2 Orthokinetic Flocculation

It is a common observation that flocculation rate can be enormously increased by stirring a suspension and this is because particle transport due to fluid motion has been introduced. This effect is simpler to discuss for laminar fluid motion. However, the result for laminar flow can be adapted to other conditions. Particles in the dispersion can be assumed to follow fluid streamlines and the collision frequency depends on the velocity gradient or shear rate, G. The collision frequency can be calculated quite simply by considering a central sphere, radius a, and flowing particles of radius a, it is assumed

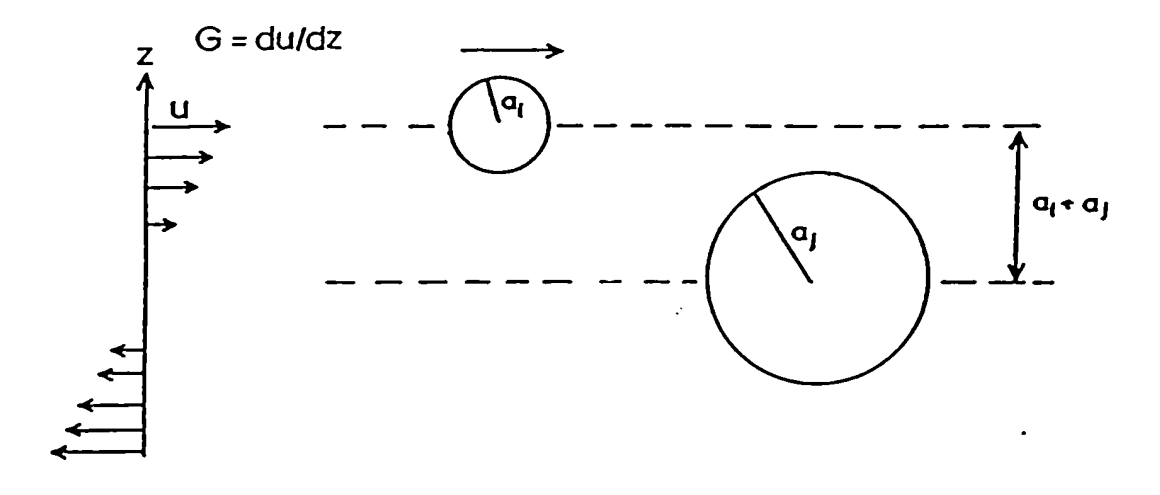


Figure 2.5 Model for orthokinetic collision in uniform, laminar shear. Flowing particles of radius a_i, travelling in streamlines collide with a central sphere of radius a_j.

that all of the particles on streamlines that bring their centres within a distance $(a_i + a_j)$ of the centre of the central sphere will collide with it (see Figure 2.5), and the collision frequency is given by;

$$J_{ij} - k_{ij} n_i n_j \tag{16}$$

where

$$k_{ij} - \frac{4}{3}G(a_i + a_j)^3 \tag{17}$$

is the appropriate rate constant.

The initial rate of decline of the total particle concentration, n_T , for a monodisperse suspension is given by,

$$-\frac{dn_T}{dt} - \frac{16}{3}n^2Ga^3 \tag{18}$$

The expressions make clear why fluid motion is so effective in promoting collisions, especially for larger particles. The dependence of the rate on the third power of particle size is in marked contrast to the perikinetic case, where the size has little or no effect.

When fluid motion is not laminar, Camp and Stein [18] have proposed that the mean velocity gradient could be calculated from the power input, P, to the fluid (e.g., in a stirred vessel):

$$\overline{G} - (\frac{P}{\mu V})^{1/2} \tag{19}$$

where V is the volume of the fluid. The mean velocity gradient can be inserted into equation (17) to give the collision frequency as,

$$J_{ij} - \frac{4}{3} n_i n_j (\frac{P}{\mu V})^{1/2} (a_i + a_j)^3$$
 (20)

the modified Smoluchowski result for collision frequency.

It has been argued [19] that this approach can only apply to particles smaller than the Kolmogoroff microscale of turbulence, a characteristic length which depends on the energy input and viscosity of the fluid. In practice [20], flocs can grow considerably larger than this and collision of such flocs should be governed by inertial effects. By contrast with equation (20), the collision rate is expected to depend on the two thirds power of the energy input rather the square root and should be independent of viscosity and hence temperature. The question of floc break-up cannot be ignored, in turbulent flocculation, and it is generally found that flocs grow only to a certain limiting size, depending on the shear rate and "strength" of the flocs. Flocs larger than this limiting size are broken down to smaller units.

2.2.4.3 Differential Settling

Particles of different size or density will settle at different rates and the resulting relative motion can cause particle collisions and hence flocculation. The collision frequency is estimated by assuming that Stokes law applies and that particle motion is linear up to contact with another particle. The result for spherical particles of same

density, is

$$J_{ij} - \frac{2\pi g(\rho_S - \rho_L)}{9\mu} (a_i + a_j)^3 (a_i - a_j) n_i n_j$$
 (21)

Clearly, differential settling will be more important when the particles are fairly large and dense, and in such cases, the mechanism can be very important in promoting flocculation.

2.2.4.4 Collision Efficiency

Practically, not all collisions result in aggregate formation. This leads to the introduction of the concept of collision efficiency factor, α_0 , which represents the fraction of collisions which will result in aggregate formation. The collision efficiencies for perikinetic and orthokinetic flocculation of the same system are not necessary the same - they depend on quite different factors.

When two particles approach each other in a medium, it becomes increasingly difficult for the liquid to be removed from the narrowing gap between them. In the limit of contact (zero separation) an infinite force would have to be applied to "squeeze out" the last layer of liquid. At greater distance (up to many particle diameters), this hydrodynamic or viscous interaction can still have effect in retarding the approach of particles. In perikinetic flocculation, the hydrodynamic effect is manifested as a reduced diffusion coefficient of the approaching particles.

For orthokinetic flocculation, hydrodynamic effects are rather more important and can give a greater reduction in rate. Essentially, the effect is to cause particles in shear flow to deviate from rectilinear paths as assumed by Smoluchowski (see Figure 2.5). The exact form of the trajectory of two particles depend on the nature of the particles and the suspending fluid and the shear rate. The influence of the presence of a particle on the trajectories of neighbouring particles has been analyzed by van der Ven and Mason [21] and have come up with this semi-empirical representation of the retarded van der Waals attraction to the limiting orthokinetic collision efficiency for a range of conditions, thus,

$$\alpha_0 - f(\frac{\lambda}{a}) C_A^{0.18} \tag{22}$$

where λ is a "characteristic wavelength" of interaction (given by $2\pi c/\omega_v$, ~ 100 nm for most materials, c is velocity of light and ω_v , dispersion frequency). $f(\lambda/a)$ is a function of λ/a (for which values are given in [21]) and,

$$C_A = \frac{A}{36\pi \mu G a^3} \tag{23}$$

It can be seen that the collision efficiency is reduced as particle size and shear rate are increased. The decrease of collision efficiency with particle size drops to zero beyond a critical size. Figure 2.6 shows the variation of collision efficiency with particle size.

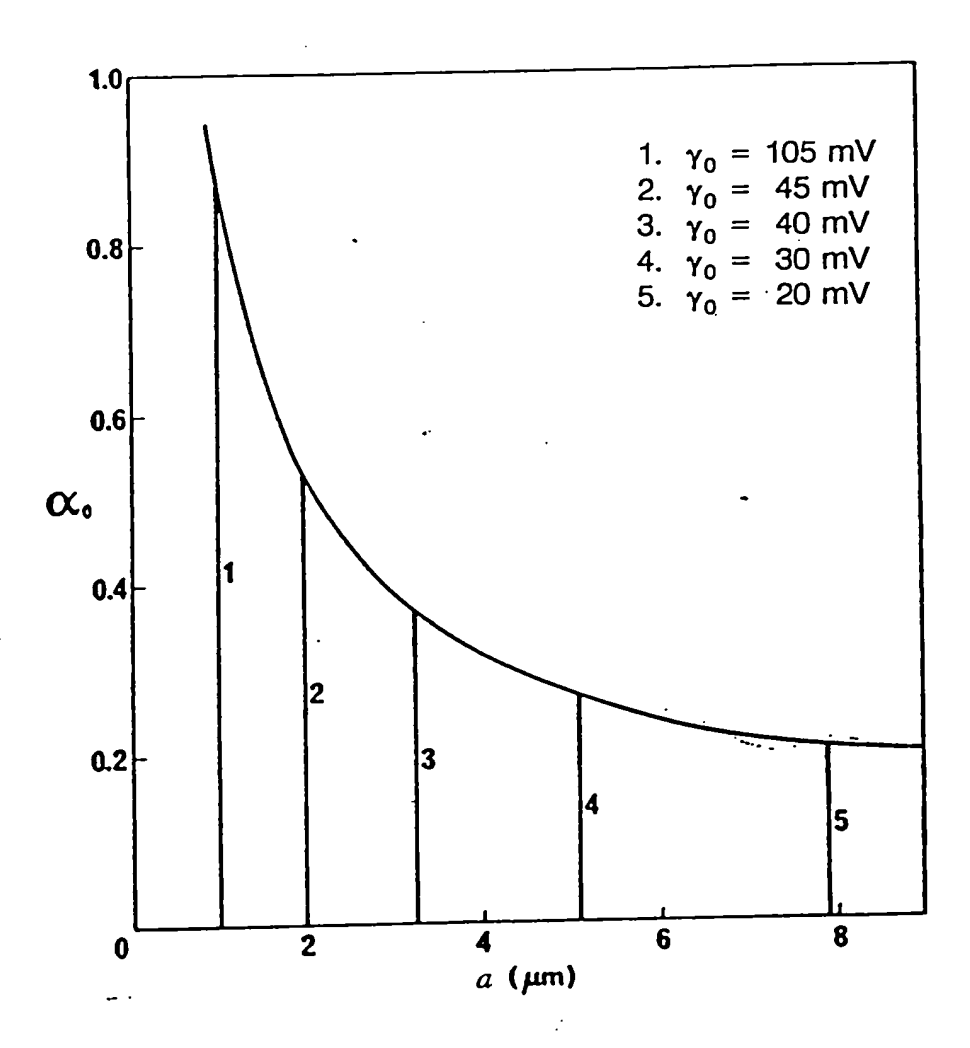


Figure 2.6 Orthokinetic collision efficiency as function of particle size at various values of surface potential, γ_0 , for hydrosol, $A = 10^{-9}$ J, $\mu = 0.001$ Pa.sec., $\epsilon = 78$, $\lambda = 100$ nm, $\kappa = 0.1$ nm⁻¹, and G = 2 sec⁻¹ [21].

2.2.5 Settling of Flocculated Systems

For the settling of flocculated systems, Michael and Bolger [14] have offered a model based on the premises that in a flocculated suspension the basic flow units are not the primary particles but are small clusters of particles (plus enclosed liquid) herein called flocs. These flocs have a certain amount of mechanical strength and so are able to retain their identity under the very mild surface shear forces and collisions experienced in gravity settling. The average floc size increases with increasing concentration of particles and decrease with increasing shear rate [25]. An increase in floc size is accompanied by a large decrease in (floc) density and Figure 2.7 show how the floc effective density ($\rho_e = \rho_F - \rho_L$) decreases with increasing floc size [29].

At low shear rates the flocs tend to group into clusters, referred to as aggregates. These aggregates may join together to form extended networks which may extend to the walls of the container and give the suspension its plastic and structural properties (Figure 2.8). The size of the aggregate would depend on the rates at which aggregates grow by collision and are broken down by viscous shear forces.

2.2.5.1 Dilute Range

In the dilute range, the model offers a modification to the Richardson-Zaki equation. If it is assumed that the average diameter of an aggregate is relatively independent of solid concentration over the "dilute" range, and that d_A does not change

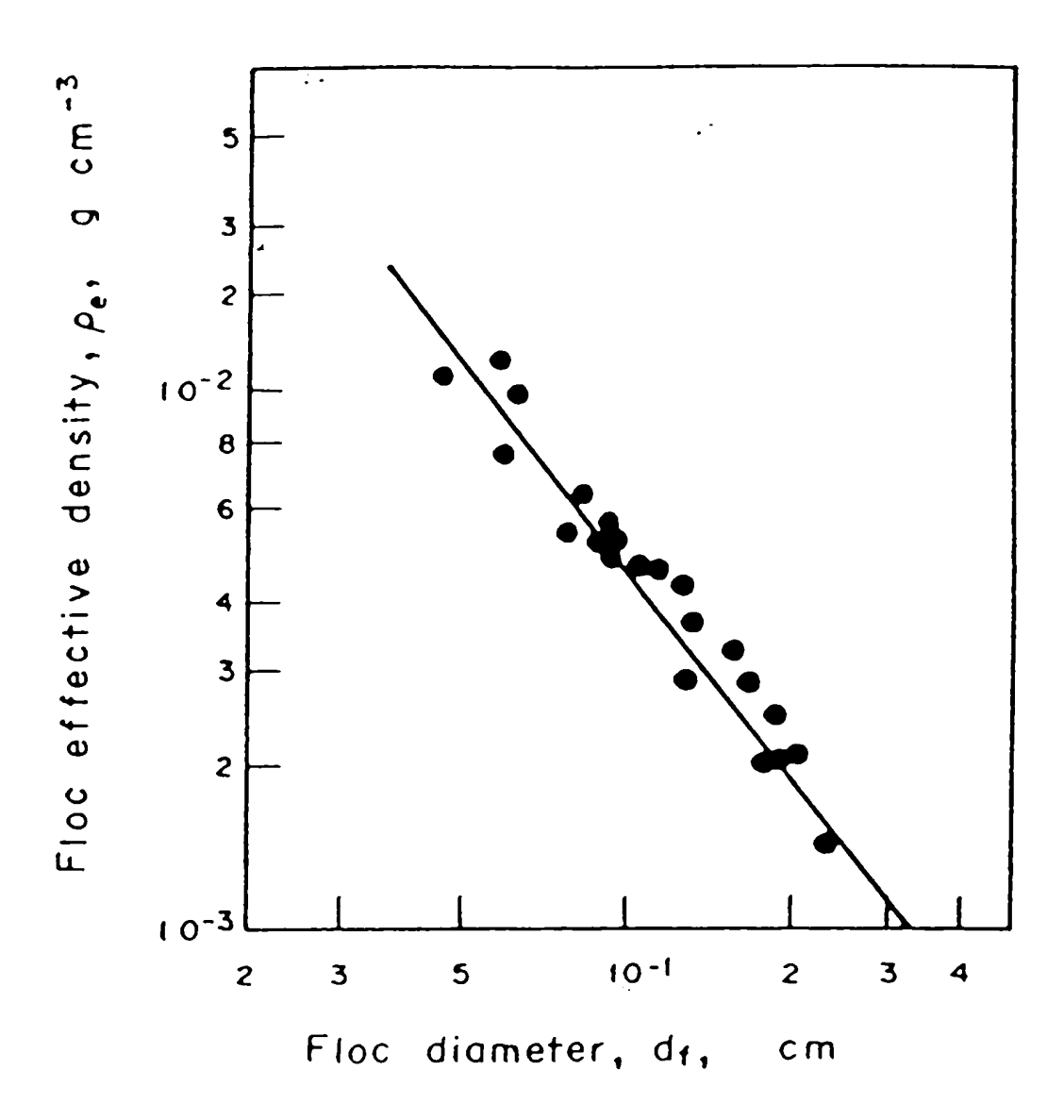


Figure 2.7 Plot of floc diameter and floc effective density (for kaolinite aluminum floc).

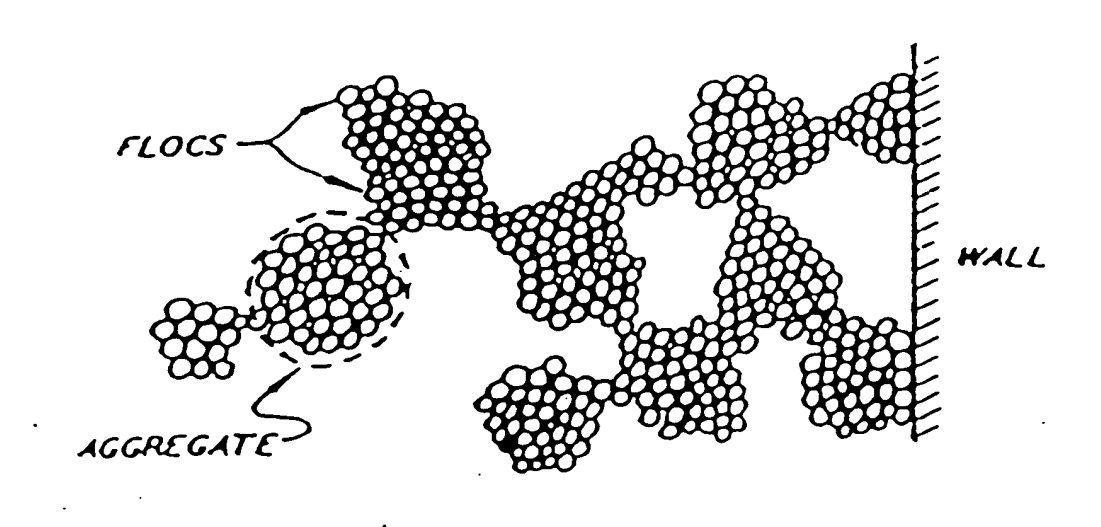


Figure 2.8 Floc-aggregate structural model.

once settling has began, then settling rate of the aggregates settling together according to equation (5) would be,

$$v_1 - v_{0,A} (1 - \theta_A)^n \tag{24}$$

where v_{0,A}, the Stokes velocity of a single aggregate is given by,

$$v_{0,A} = \frac{g(\rho_A - \rho_L)d_A^2}{18\mu_L}$$
 (25)

From a material balance on the solid, it follows that,

$$\rho_D - \rho_L - \theta_A(\rho_A - \rho_L) - \theta_S(\rho_S - \rho_L) \tag{26}$$

and,

$$\frac{\theta_A}{\theta_S} - \frac{\rho_S - \rho_L}{\rho_A - \rho_L} - C_{AS} \tag{27}$$

C_{As} is the ratio of volume of aggregate to volume of solid in aggregate and equation (24) can be rewritten as,

$$v_1 = v_{0A} (1 - C_{AS} \theta_S)^n \tag{28}$$

From which,

$$v_1^{1/n} - v_{0,A}^{1/n} (1 - C_{AS} \theta_S)$$
 (29)

Thus, plot of $v_1^{1/n}$ versus θ_s should yield a straight line. $v_{0,A}$ can be obtained from the ordinate intercept from which the average aggregate diameter d_A can be estimated. C_{AS} is obtained from the abscissa intercept.

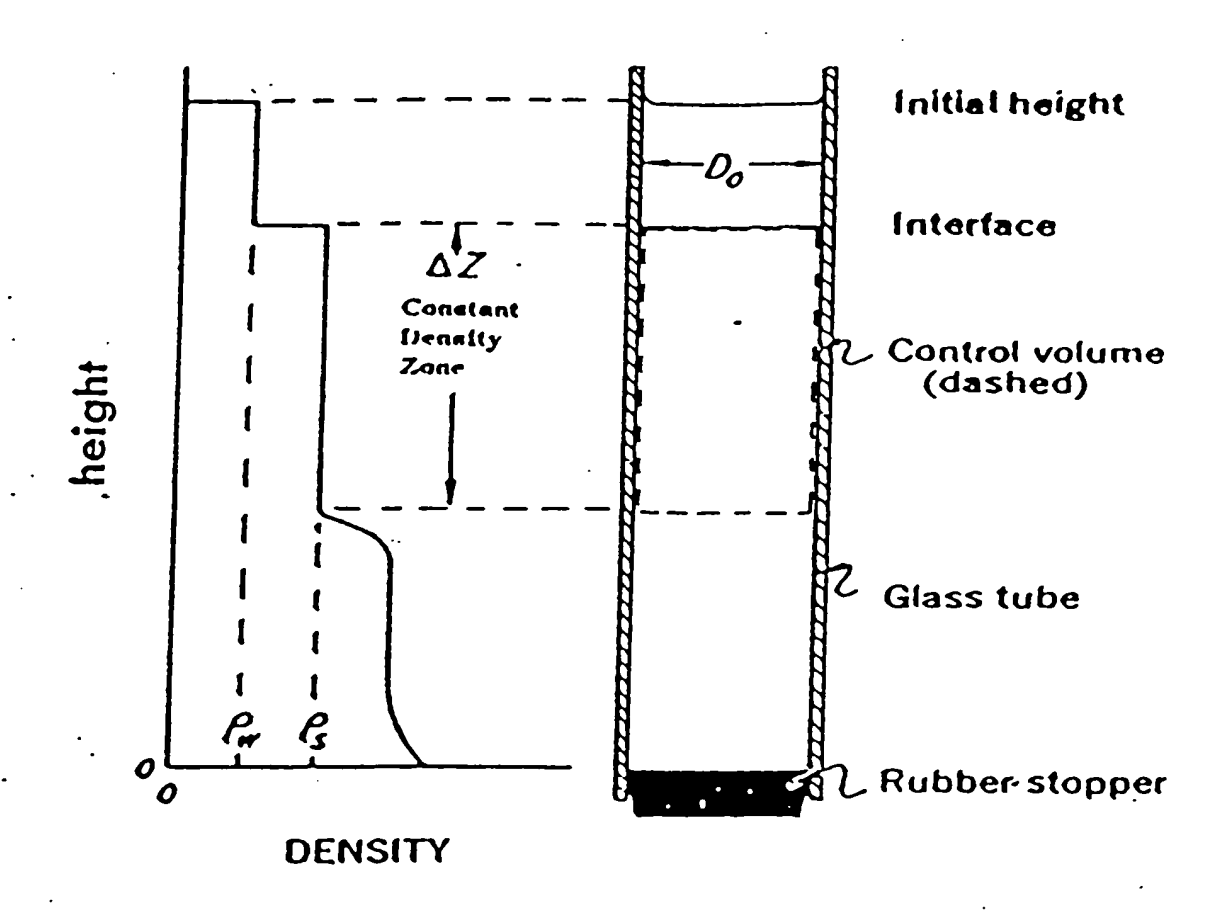


Figure 2.9 Control volume and height-density relationships. Left; Height vs density profile at time t. Right; Settling tube showing control volume.

2.2.5.2 Beyond Dilute Range

As the concentration increases beyond the "dilute" range, the aggregates settle as a coherent network. During the early free-fall settling period there exist a region equal to the density of the original dispersion at time t=0 [12]. Consider a control volume of length ΔZ (Figure 2.9), moving downward with velocity v_2 . This volume may be regarded as a plug of slurry supported by fluid friction and buoyancy forces. In addition, the aggregate networks may extend to the walls and bottom of the container, so that it is also supported by resting on the underlying material and by shear forces at the walls.

The total force exerted by the underlying material on the control volume is,

$$F_U - \frac{\pi}{4} D_0^2 \sigma_y \tag{30}$$

If the movement is treated as pure plug flow, the shear stress at the container wall should just equal the shear stress τ_y , of the original slurry. Thus the wall support force is,

$$F_{W} - \pi D_0 \Delta Z \tau_{y} \tag{31}$$

The net weight W_{net} , the weight of the aggregates minus the weight of the displaced liquid is,

$$W_{net} = \frac{\pi}{4} D_0^2 \Delta Z g(\rho_A - \rho_L) \theta_A \tag{32}$$

combining equations (26) and (32),

$$W_{net} - \frac{\pi}{4} D_0^2 \Delta Z g(\rho_S - \rho_L) \theta_S \tag{33}$$

The pressure gradient through the control volume resulting from the flow of displaced liquid up through the spaces between the aggregates may be estimated by applying the Kozeny-Carman equation to the case of pore flow. The geometric factors which must be evaluated are the pore shape factor, k_0 ; the pore hydraulic radius, r_H ; and the tortuosity factor, L_P .

$$r_H = \frac{\text{flow area}}{\text{wetted perimeter}} = \frac{\varepsilon}{S} = \frac{\text{void fraction}}{\text{specific surface area}}$$
 (34)

$$L_{p} = \frac{length\ of\ effective\ fluid\ path\ through\ pores}{length\ of\ straight\ flow\ path} \tag{35}$$

If v_2 is the settling velocity of the interface, then the average velocity, v_L of liquid in the pores is,

$$v_L = \frac{v_2}{\varepsilon} L_P \tag{36}$$

Substituting these relationships into the Poiseuille equation, the Kozeny-Carman equation (see appendix II) predicts that,

$$\frac{dp}{dZ} - k_0 \mu_L \nu_2 L_P^2 \frac{S^2}{\varepsilon^3} \tag{37}$$

The total upward force exerted on the control volume due to friction is then,

$$F_f = \frac{\pi D_0^2}{4} \Delta Z \frac{dp}{dZ}.$$
 (38)

At equilibrium, the net weight W_{net} is balanced by the forces F_U , F_w and F_P thus,

$$W_{net} - F_U - F_W - F_f = 0 (39)$$

and by combining and rearranging these equations, the general settling equations are,

$$v_2 - v_2' \left[1 - \frac{D_y}{D_0} - \frac{Z_y}{Z_0}\right] \tag{40}$$

where,

$$v_2' - \frac{g(\rho_S - \rho_L)\varepsilon^3 \theta_S}{k_0 \mu_L L_p^2 S^2},\tag{41}$$

$$D_{y} - \frac{4\tau_{y}}{g(\rho_{S} - \rho_{L})\theta_{S}} \tag{42}$$

and

$$Z_{y} = \left(\frac{\sigma_{y}}{g(\rho_{s} - \rho_{L})\theta_{s}}\right) \left(\frac{Z_{0}}{\Delta Z}\right). \tag{43}$$

Physically, v_2 ' is the settling rate in an infinitely large container. The yield diameter D_y , can be calculated directly from equation (42) by using a concentric viscometer to estimate the yield stress τ_y , of the aggregate network. It is possible to determine the yield height, Z_y , empirically. At any particular phase during the free settling period, the value of the ratio $\Delta Z/Z_0$ in equation (43) should depend upon the aggregate concentration and

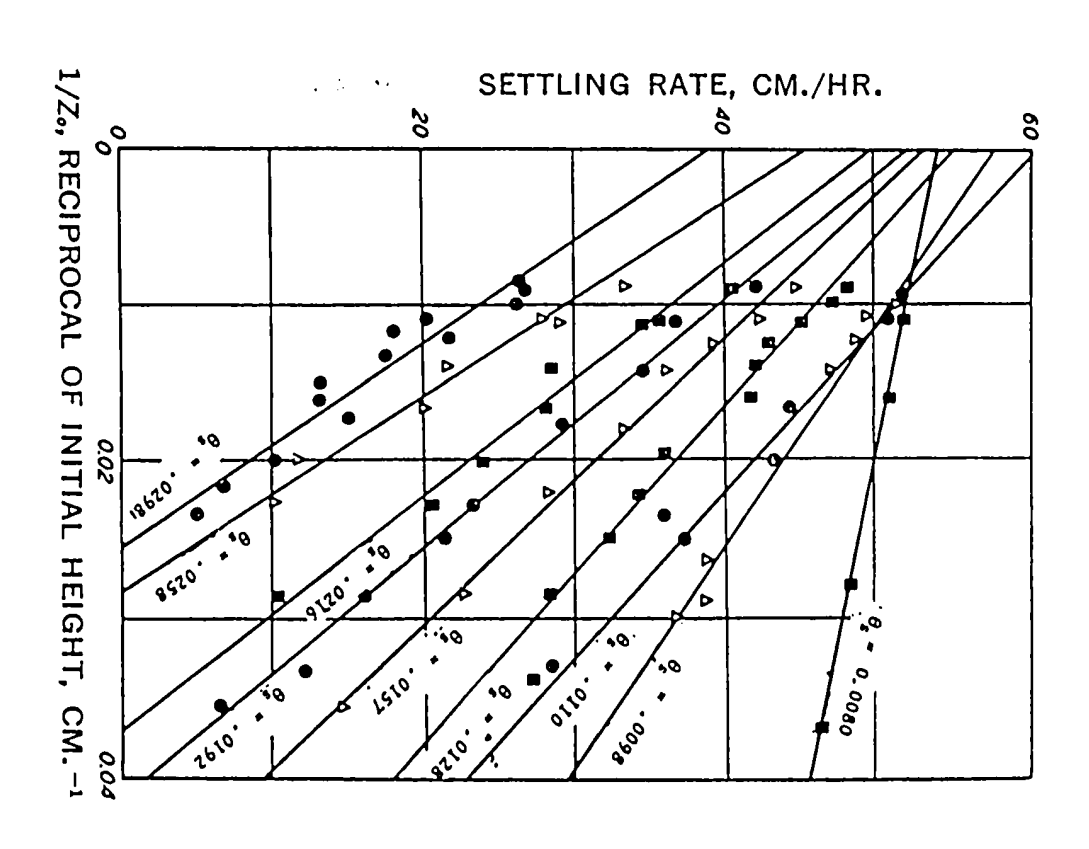


Figure 2.10 Correlation of settling rates by equation (44) for kaolin-water system.

properties, but independent of Z_0 . Thus for practical importance, the settling rate equation may be written as,

$$v_2 - v_2' \left[1 - \frac{Z_{yl}}{Z_0}\right] \tag{44}$$

 $Z_y \rightarrow Z_{y1}$, as $t \rightarrow t_1$. At any fixed solid concentration, Z_{y1} should be a constant. Application of equation (44) is shown in Figure 2.10 for kaolin-water system. The plot of v_2 against $1/Z_0$ yields a straight line at each θ_s . v_2 ' and Z_{y1} may be determined from the ordinate intercepts of these lines.

Given enough time, in a vessel of infinite extent, the liquid paths tend to approach the configuration of smooth, vertical tubes rising up through the continuous aggregate region. For this limiting liquid tube and aggregate shell configuration, the geometric constants in the Kozeny-Carman equation reduce to $L_p = 1$ and $k_0 = 2$, for smooth, straight cylinders. The void fraction, ε , is the volume of the supernatant liquid outside the aggregates, i.e., the volume of flow tubes. Therefore:

$$\varepsilon = 1 - \theta_A = 1 - C_{AF}\theta_F \tag{45}$$

$$S - n_p \pi d_p - \frac{4\varepsilon}{d_p} \tag{46}$$

Substituting in equation (41), the settling rate, in an infinitely large tube is given by,

$$v_2' = \frac{g(\rho_S - \rho_L)d_P^2 \theta_S}{32\mu_L} (1 - C_{AF} \theta_F)$$
 (47)

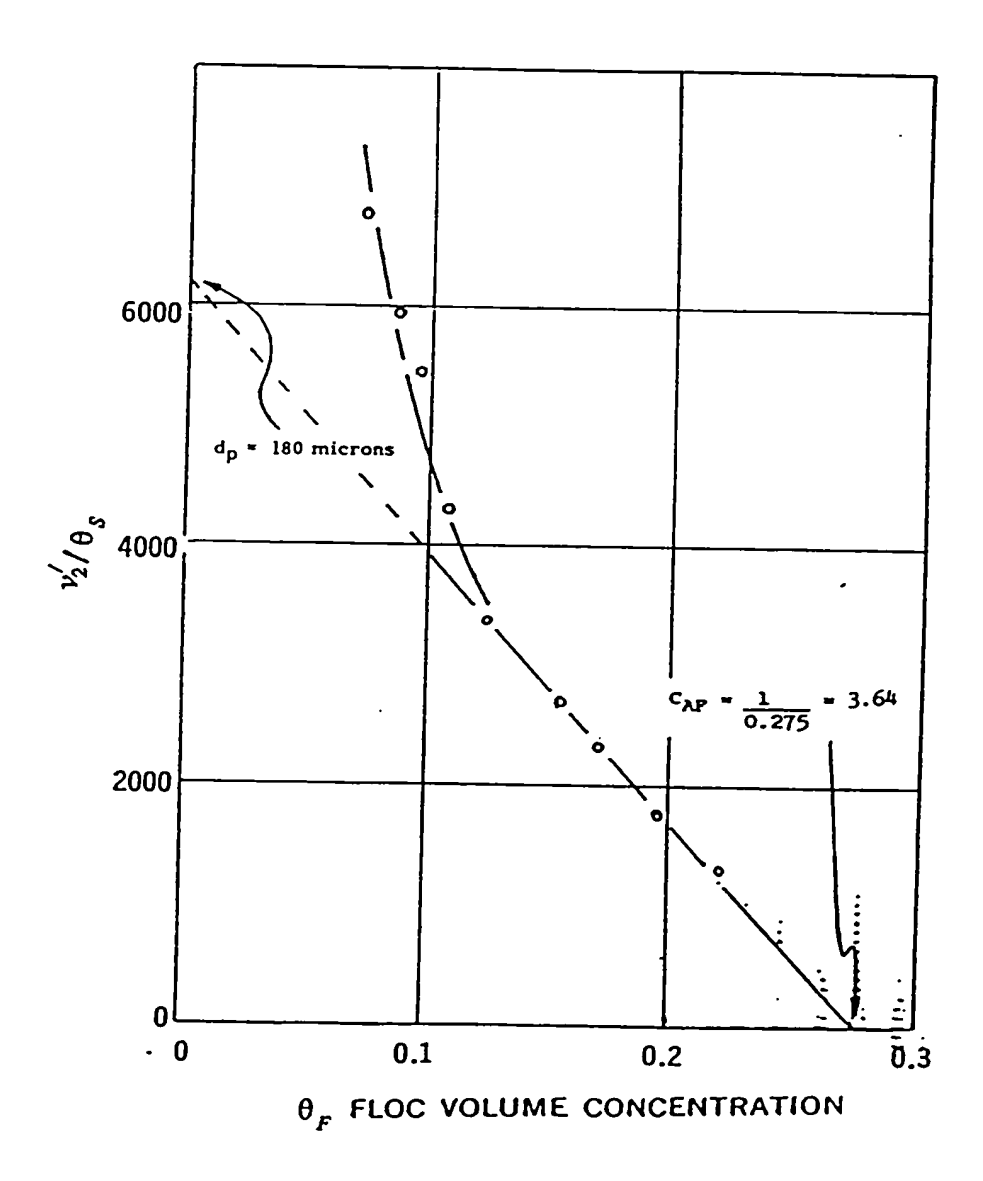


Figure 2.11 Plot of v_2'/θ_s against θ_F for water-kaolin system [22].

or

$$\frac{v_2'}{\theta_s} - K(1 - C_{AF}\theta_F) \tag{48}$$

where C_{AF} is the ratio of aggregate to floc volume and the constant K is given by,

$$K = \frac{g(\rho_S - \rho_L)d_p^2}{32\mu_L} \tag{49}$$

So if d_p and C_{AF} are assumed to be constant with respect to volume fraction of particles, then a plot of V_2'/θ_s versus θ_F should give a straight line. From the ordinate intercept, the average pore diameter, d_p can be estimated and from the abscissa intercept, C_{AF} can also be estimated.

2.2.5.3 Floc Volume Fraction and Final Sediment

X-ray density data of Gaudin and Fuerstenau [23], shown in Figure 2.12, show that the density of the final settled bed is not uniform with respect to height. It consists of a lower uniform density region plus an upper, non-uniform, decreasing density zone. If the lower uniform density region is considered to be made up of random close-packed flocs (floc volume fraction in this region is 0.62), then final volume of the bed should be,

$$\frac{\pi}{4}D_0^2 Z_f - \frac{\pi}{4}D_0^2 \frac{Z_0 \theta_F}{0.62} + \frac{\pi}{4}D_0^2 b \tag{50}$$

 $\theta_{\rm F}$ is the floc volume fraction originally present in the suspension before settling occurs and b is the small additional height added by the presence of the upper, non-uniform, low density zone. From equation (49),

$$Z_f = \frac{Z_0 \theta_F}{0.62} + b \tag{51}$$

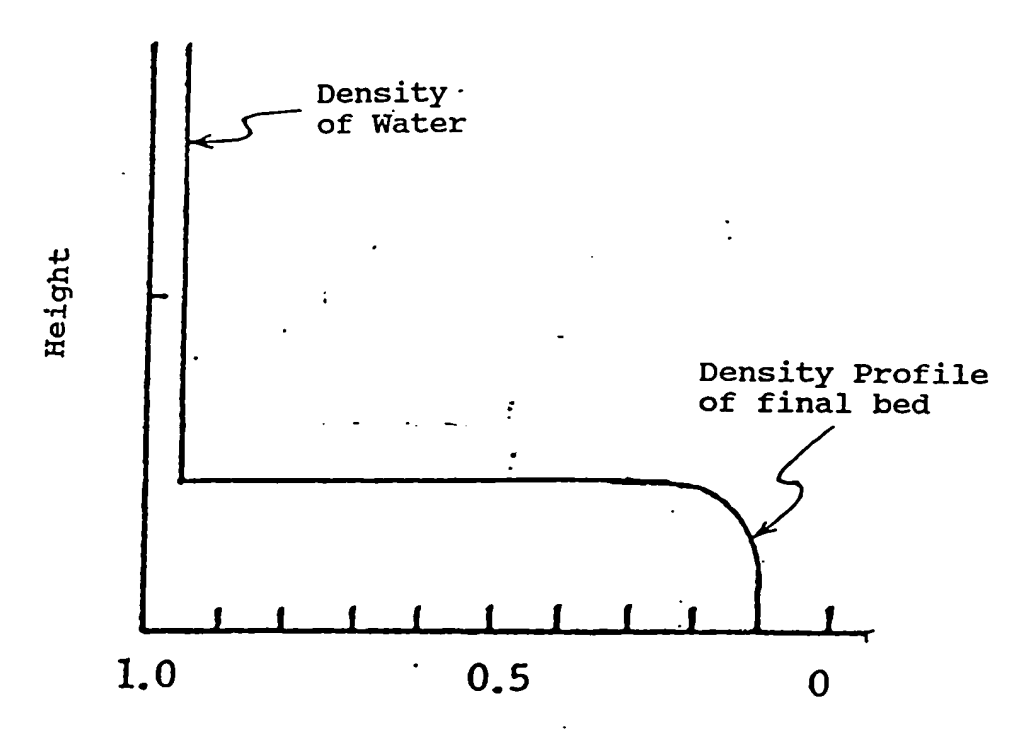
 Z_0 is the (initial) height of dispersion and Z_f is the final height of the settled bed. The value of b can be estimated by introducing the identity $\theta_F = C_{FS}\theta_S$ into equation (51) to yield,

$$Z_f = \frac{C_{FS}}{0.62} Z_0 \theta_S + b. \tag{52}$$

The ordinate intercept on the plot of Z_f against $Z_0\theta_S$ at each concentration should give b, and the floc volume fraction for the particular concentration is easily evaluated. A simple method is to measure two final sediment heights for two initial heights (Z_{01} and Z_{02}) at each concentration and then calculate θ_F , from equation (52) in the form,

$$\theta_F = 0.62(\frac{Z_{fl} - Z_{f2}}{Z_{01} - Z_{02}}) \tag{53}$$

 Z_{f1} and Z_{f2} are the two final sediment heights.



 I/I_0 , Ratio of Transmitted to Incident Radiation

Figure 2.12 X-ray data of Gaudin and Fuerstenau [23] showing density of final settled bed of a flocculated (aqueous) system. The lower the ratio I/I₀, the denser the dispersion at the particular height.

2.3 PARTICLE SEDIMENTATION IN AN ALLOY SYSTEM

Particle sedimentation studies have always involved aqueous systems. In the first ever documented study of sedimentation of particles in liquid alloy systems, Lafreniere and Irons [7] employed the graphical method of Wallis to characterize the sedimentation of 90 µm SiC particles in molten aluminum alloy. Settling rates obtained at various volume fractions from 0.05 to 0.3 were found to be lower than the Stokes velocity. A near-perfect fit to the Richardson-Zaki equation was obtained with n of about 5.3 and the concentration of particles in the final sediment was found to be as dense as about 54% solid by volume.

Hanumanth et al [24] have recently developed a model to describe the sedimentation of SiC particles in molten aluminum. The model basically considers the fundamental forces that are acting on the solid and liquid phases and works towards the settling rates through mass and momentum equations.

Conservation of mass.

$$\frac{\partial \theta_{s}}{\partial t} + \frac{\partial (v_{s}\theta_{s})}{\partial x} - 0 \qquad (solids)$$

$$\frac{\partial \theta_L}{\partial t} + \frac{\partial (v_L \theta_L)}{\partial x} - 0 \quad (liquid) \tag{55}$$

Conservation of momentum;

$$\rho_{S} \frac{\partial(v_{S}\theta_{S})}{\partial t} + \rho_{S} \frac{\partial(v_{S}^{2}\theta_{S})}{\partial x} + \theta_{S} \frac{\partial p}{\partial x} - \rho_{S}\theta_{S}g + F_{D} = 0 \quad (solids)$$
 (56)

$$\rho_{L} \frac{\partial (v_{L} \theta_{L})}{\partial t} + \rho_{L} \frac{(\partial v_{L}^{2} \theta_{L})}{\partial x} + \theta_{L} \frac{\partial p}{\partial x} - \rho_{L} \theta_{L} g - F_{D} = 0 \quad (liquid)$$
 (57)

The drag force F_D which may be a function of relative velocity, viscosity and volume fraction is expressed as,

$$F_{p} = \beta(\nu_{s} - \nu_{r}) \tag{58}$$

where β , the friction coefficient extracted from equation (5), the Richardson-Zaki equation gives,

$$\beta = \frac{18\mu_L \theta_S}{d_S^2} (1 - \theta_S)^{-2.65}.$$
 (59)

The model surprisingly agrees well with experimental data (see Figure 2.13) from the work of Lafreniere and Irons in spite of the fact that the drag coefficient represents an extrapolation from aqueous systems. The implication is that there is no significant clustering, as far as these large particles are concerned, during settling. This inference is further reinforced by the fact that the final sediment concentration was found to be as high as 0.54 volume fraction SiC, close to the value of 0.62, characteristic of random close-packed arrangement, which could not be achieved in the presence of any appreciable clustering.

A weakness however, of the model is on the issue of the transition zone at the

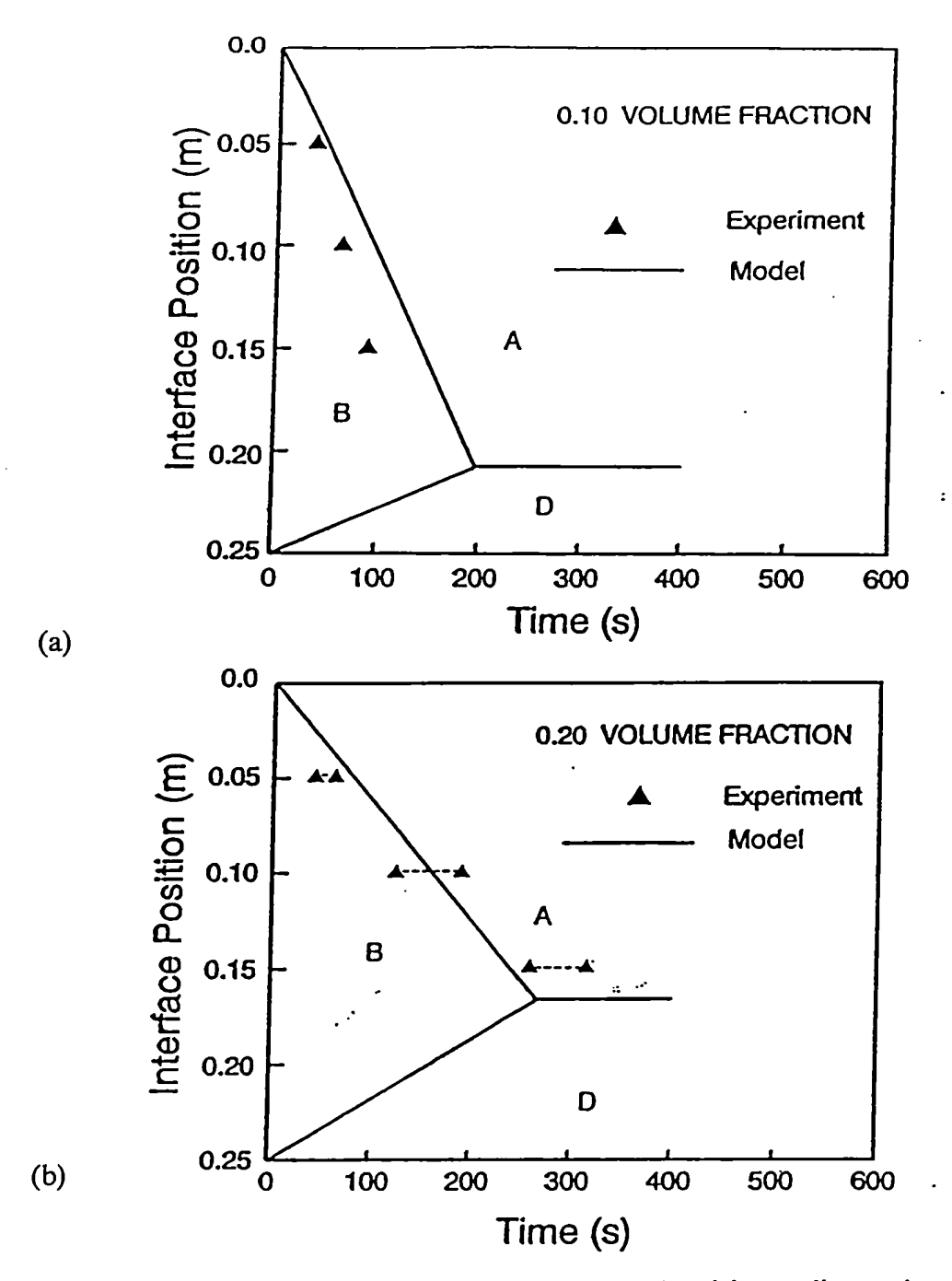


Figure 2.13 Position of the clarified front and the rising sediment interface as a function of time during sedimentation of (a) 0.10 and (b) 0.20 volume fraction composite.

interface between the clarified liquid and the rest of the dispersion. Although, it concedes that this zone may be caused by the distribution of particle size, the model predicts that the zone would be vanishing with increasing SiC volume fractions, contrary to experimental observation. Hence, extrapolation of these results to finer particles 10-15 µm, typical of commercial MMCs, should be made cautiously, because surface forces are quite significant and the fine particles may exhibit some appreciable level of clustering.

CHAPTER 3

EXPERIMENTAL PROCEDURE

3.1 APPARATUS AND MATERIALS

The sedimentation experiments were carried out in a clay-graphite crucible of 25.4 cm internal diameter and 47.5 cm height which was placed inside a resistance-heated furnace (Figure 3.1). The melt surface was exposed to air. The crucible was covered with a thermal insulator leaving a small opening to carry the shafts of the probe and impeller. The SiC particles were mixed into the melt with a pitched-blade turbine impeller, fabricated from graphite and driven by a variable AC motor. The impeller shaft was made of mild steel and enclosed in a graphite sleeve to avoid contact with the aluminum melt. All joints were sealed with a high-temperature ceramic adhesive.

The resistance measurements were taken automatically by a commercially available portable, high accuracy micro-ohmmeter (TECRAD DMO-350). Measurements of electrical resistance lower than 0.2 ohms require use of the four point probe, which has the advantage of eliminating errors by cable and contact resistance. The measuring technique incorporates two distinct circuits: a constant current source and a voltage measuring circuit. The constant current (in the form of a brief pulse lasting for only 30 ms each time) is passed into the specimen via the two outer electrodes of the probe and the voltage measuring is made through the two inner electrodes. The probe (Figure 3.2) used in the experiments is a modification of that developed by

Lafreniere. This new version of the probe was constructed of graphite and the electrodes and their connecting wires made entirely of tungsten wires, 1.4 mm in diameter (without any soldering to silver wires). The modification reduced the sensitivity of the probe, however, it improved stability and reproducibility.

The particle size distribution of the green silicon carbide particles used in the experiments (supplied by Ritchey Supply Ltd., Missisaga, Canada) was measured with a Horiba CAPA-700 particle analyzer (Horiba Ltd., Kyoto, Japan). The mean Stokes equivalent diameter was found to be 14µm with a standard deviation of 9µm. A commercial foundry alloy, A356 (supplied by ALCAN), often used for MMCs, was used. The major alloying elements are 7.3 wt% silicon and 0.33 wt% magnesium.

Table 1 Relationship between volumetric fraction and weight of SiC in 23.4 kg of aluminum.

SiC (%)	2.5	5	7.5	10	15	20
Wt (g)	780.4	1588.7	2529.7	3347.6	5305.1	7517.9

3.2 EXPERIMENTAL PROCEDURE

Initially 23.4 kg of the alloy was charged into the crucible to produce a melt depth of 20 cm. The melt was maintained at 660°C and the impeller lowered into the melt. An extra 320 g of magnesium turnings is gradually added and stirred for about 20 minutes. Subsequently the silicon carbide particles were added to the melt and mixed at a speed of 525 rpm for about 3 hours. At about 15 minutes to the end of the mixing the probe was lowered into the dispersion (to ensure that the probe was at same temperature with melt by the time resistance measurement begins) to a depth of one-quarter (1/4) the melt height from the (melt) surface.

At the end of the mixing time the mixer was stopped, the impeller was taken out of the melt and simultaneously, the resistance measurement was started. The resistance was measured every 10 seconds, until the settling interface had passed the probe. During the experiment, a pin sample of the molten mixture was sucked periodically into a pyrex tube near the centre of the bulk at same horizontal level with the probe. The samples were used for carbon analysis to determine the SiC content of the MMC at various times during the settling. The procedure was carried out for two other different probe locations, one-half (1/2) and three-quarter (3/4) melt height below the surface. The above procedure was done for the various SiC volume fractions, indicated in table 1.

The pin samples were removed from the glass shell and any glass adhering to it removed by grinding and used to determine the SiC content of the samples. The density of the sample was measured using a standard specific gravity bottle. Following this, the

carbon concentration in weight percent was determined by combustion in a Leco volumetric carbon analyzer (Leco Corporation, Michigan, U.S.A.). The SiC volume fraction (ϕ_{siC}) was calculated using the expression:

$$\phi_{SIC} - (\frac{W_C}{100}) \times \frac{atomic\ weight\ of\ SiC}{atomic\ weight\ of\ carbon} \times \frac{\rho_C}{\rho_{SiC}}$$
 (60)

where W_c is weight percentage of carbon in the sample, ρ_c is the density of the sample and ρ_{sic} is the density of silicon carbide.

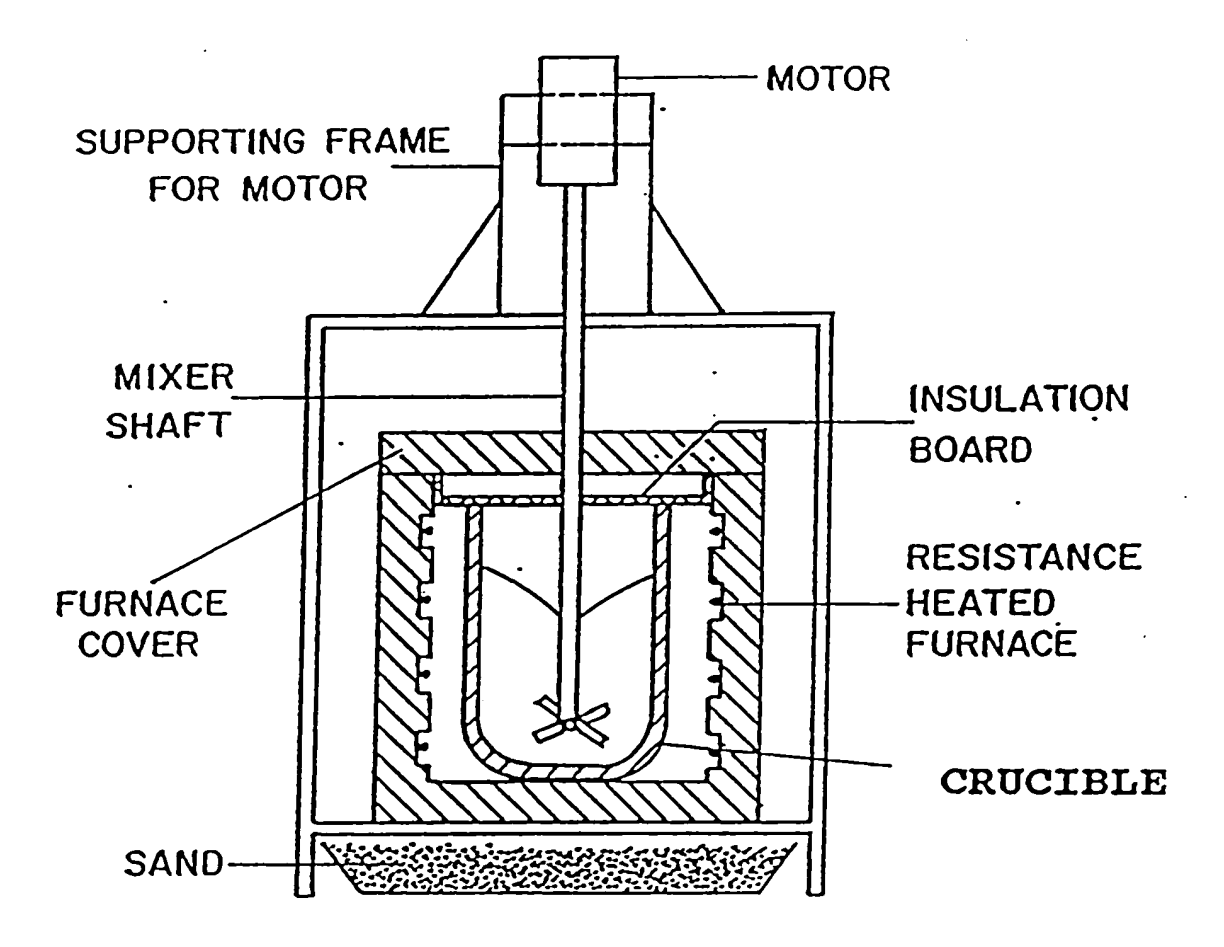


Figure 3.1 Schematic diagram of the experimental apparatus.

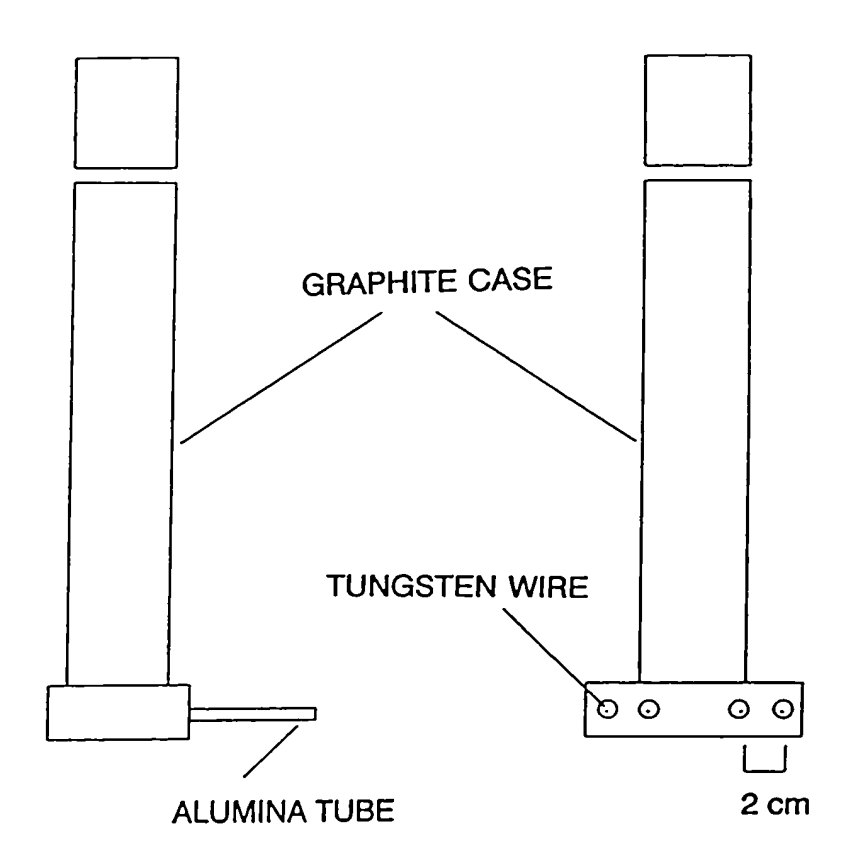


Figure 3.2 Schematic diagram of the four-point probe.

CHAPTER 4

RESULTS AND ANALYSIS

The output of the probe shows variation of resistance with time at a particular depth inside the dispersion. Time at which changes in resistance are experienced are noted and used to reconstruct the settling event in the dispersion. The resistance measured by the probe is a combination of the resistances of the aluminum alloy and the amount of SiC around the probe, (and possibly the presence of the probe itself). Since the probe was kept at the same position during an experiment, only the change in the volumetric fraction of the SiC particles (and corresponding aluminum melt) in the vicinity of the probe during the sedimentation process, can be responsible for any change in resistance. The temperature of the melt was kept constant.

Calibration curve of the probe is shown in Figure 4.1. This probe was used in experiments involving the 5, 10, 15 and 20 vol% SiC MMC. The curve essentially shows how resistance varies with nominal volumetric fraction of SiC particles. With no SiC, the melt resistance is about 2.5 micro-ohm. When 5 vol% SiC was added the resistance increased to about 2.9 micro-ohms. Further increases were observed with increasing SiC volume fraction. The increase in resistance with volume fraction of the SiC is quite linear. In essence, the probe can be used to estimate the volumetric fraction of SiC in the melt.

4.1 RESISTANCE VERSUS TIME CURVES

4.1.1 2.5 vol% SiC MMC

The melt height was about 20 cm and outputs of the probe at 5, 10 and 16 cm below the melt surface are shown in figures 4.2 to 4.4. The resistance, in all the three cases, stayed fairly constant at about 3.49 micro-ohms during the initial stages of the experiment. With the onset of sedimentation, the resistance began to decrease due to particle settling. In each of the three outputs, the resistance dropped gradually to a steady value of around 3.4 micro-ohms. The three curves, in terms of shape, look alike, the main difference lies in the time of transition from the initial constant resistance to that of the clarified aluminum alloy. At 5 cm below the melt surface, the transition started after about 100 seconds and lasted for about 150 seconds. At 10 cm below the melt surface, the transition period began after about 200 seconds to 300 seconds. At 15 cm below the melt surface, transition started after 250 seconds and lasted for 450 seconds.

4.1.2 5 vol% SiC MMC

The melt height of the 5 vol% SiC MMC was about 21.5 cm and probe locations were 5, 10 and 16 cm below the melt surface, with outputs shown in figures 4.5 to 4.7. The resistance, in all the three cases, stayed fairly constant at about 2.9 micro-ohms during the initial stages of the experiment. With the onset of sedimentation, the

resistance began to decrease due to particle settling. In each case, the resistance dropped gradually to a steady value of around 2.5 micro-ohms. As observed above, the three curves look alike in terms of shape, the main differences being the time of transition from the initial constant resistance to that of the clarified aluminum alloy. At 5 cm below the melt surface, the transition started after about 800 seconds and lasted for about 500 seconds. At 10 cm below the melt surface, the transition period began after about 1500 seconds to 2400 seconds, lasting for about 900 seconds. At 15 cm below the melt surface, transition started after 1500 seconds and lasted for 1300 seconds.

4.1.3 7.5 vol% SiC MMC

The melt height was about 21.5 cm and outputs of the probe at 5, 10 and 16 cm below the melt surface are shown in figures 4.8 to 4.10. During the initial stages of the experiment, resistance in the dispersion stayed fairly constant at about 4 micro-ohms at all three depths. With the onset of sedimentation, the resistance began to decrease due to particle settling. The resistances later, at 5 and 10 cm below melt surface dropped gradually to a steady value of about 3.75 micro-ohms. Transition time were 500 and 1000 seconds at 5 cm below melt surface, and 1100 and 1900 seconds at 10 cm below the melt surface. At 15 cm below melt surface, the transition times were 2000 and 3200 seconds.

4.1.4 10 vol% SiC MMC

The melt height was about 23 cm and probe locations were 6, 12 and 17 cm below the melt surface respectively. Curves of similar shapes were obtained at 6 and 12 cm below the melt surface (figures 4.11 and 4.12 respectively). As seen above, the only difference is in the transition times. At 6 cm below the melt surface, the resistance stayed constant at an approximate value of 3.35 micro-ohms, for about 1300 seconds and started to decrease as the particles passed the probe. This transition period lasted for 1400 seconds. The resistance then stayed constant at around 2.6 micro-ohms, indicating the passage of the clarified front at the probe position. The resistance of 3.35 micro-ohms corresponds to the initial SiC volumetric fraction of 10%, and the steady state resistance after the drop corresponds to that of the clarified melt. At 12 cm below the surface, the transition period starts after about 2000 seconds and lasted for almost 2500 seconds. The final resistance recorded was about 2.7 micro-ohms.

The output of the probe at 17 cm below the melt surface (figure 4.13) was slightly different from the two mentioned above. After staying constant for at about 3.35 micro-ohms for a period of 2000 seconds, the resistance increased slightly to a value of about 3.5 micro-ohm, indicating a slight increase in the SiC concentration at the probe location. The transition period lasted for about 4000 seconds and the clarified front finally reached the probe after 8000 seconds of settling. The steady state resistance was about 2.7 micro-ohms.

4.1.5 15 vol% SiC MMC

The melt height was about 24.5 cm and resistance measurements were taken at 6, 12 and 18 cm below melt surface respectively. The outputs of the probe for 15 vol% MMC, at the three depths given in figures 4.14 to 4.16, show three different curves. At 6 cm below the surface, the resistance stayed at a constant value of about 3.8 microohms for 2800 seconds and went through the transition period for another 2200 seconds. After the passage of the clarification front at the probe position, the resistance settled at 2.6 micro-ohms.

At 12 cm below the melt surface, figure 4.15, the resistance stayed constant at a value of 3.6 micro-ohms for 2000 seconds and then increased slightly, to a local maximum of 3.8 micro-ohms. The period of increasing resistance lasted for another 2000 seconds, followed by a period of decreasing resistance. The transition from the local maximum to the final steady state when the clarification has passed the probe lasted for 4500 seconds. The final steady state resistance was 2.8 micro-ohms.

Figure 4.16 shows the output of the probe at 18 cm below the melt surface. At this depth, the figure reveals that there was no decrease in resistance. The resistance stayed constant for a period of 2000 seconds and then began to increase. The increase was gradual and the curve flattened out, when the resistance had reached a value of about 4.6 micro-ohms, after 9000 seconds of settling. The resistance stayed constant thereafter.

4.1.6 20 vol% SiC MMC

The height of the melt was about 26 cm and the readings were taken at 7, 13 and 19 cm below the melt surface respectively. At 7 cm below the melt surface (Figure 4.17), the resistance stayed approximately constant at 3.8 micro-ohms during the first 3500 seconds and then rose to a local maximum of about 4.7 micro-ohms after 7500 seconds of the settling process. The resistance, thereafter began to decrease gradually until the clarified melt had passed the probe. The resistance then stayed constant for rest of the time at about 2.9 micro-ohms.

The shapes of the curves obtained at 13 and 19 cm below melt surface (Figures 4.18 an 4.19 respectively) are similar in shape. At 13 cm below melt surface resistance stayed constant for about 2000 seconds and began to increase gradually until it reached a value of about 4.6 micro-ohms after 14000 seconds of settling. At this period, the final sediment had reached the probe location. At 19 cm below the melt surface, the initial constant resistance is about 4.2 micro-ohms, remained at this for a little over 1000 seconds, rose gradually to a value of about 4.65 micro-ohms in 7000 seconds, and then stayed constant at this value for the rest of the time.

4.2 SEDIMENTATION PATTERNS

Sedimentation patterns are constructed from the probe outputs. These patterns are plots of the positions of the various interfaces inside the dispersion against time.

Settling rates of the particles in the melt are estimated from these plots.

Figures 4.20 to 4.22 show sedimentation pattern of 2.5, 5 and 7.5 vol% SiC MMCs respectively. These patterns look similar and show the evolution of these MMCs from a dispersion of initial uniform density B, to the clarified melt A. During this evolution, there was always a transition zone. This zone is marked as A1 in the diagram. The zone widened with time as the particles travel down the crucible. Settling rate of the 2.5 vol% SiC MMC is about 0.035 cm/s. For the 5 and 7.5 vol% SiC MMCs, settling rates are 0.006 and 0.0049 cm/s respectively. An estimate of the thickness of the transition zone at 5 cm below the melt surface are 4, 3.13 and 3.5 cm respectively for the 2.5, 5 and 7.5 vol% SiC MMCs.

In the sedimentation of the 10 vol% SiC MMC (Figure 4.23), an extra zone labelled C can be identified. Solid concentration in this zone may vary from that of B at the C/B interface to that of the final sediment at regions close to the bottom of the crucible. The settling rate is estimated at 0.003 cm/s. The transition zone at 5 cm below melt surface is about 3.65 cm thick.

As many as five zones are identified, in the sedimentation pattern of the 15 vol% SiC MMC, These are A, A1, B, C and the final sediment zone, labelled D. The resistance recorded inside the final sediment is about 4.6 micro-ohms, which corresponds to about 27 vol% SiC (from extrapolation of figure 4.1). The height of this sediment estimated from extrapolation of figure 4.16 is about 11.5 cm. Calculation of the final sediment concentration based on this height using the SiC volume conservation

equation, thus,

$$\theta_{S_t} h_t - \theta_{S_t} h_t \tag{61}$$

where h is height and the subscripts i and f represent initial and final conditions respectively, gives about 28.3 vol% SiC. The two values of the final sediment concentration can be taken to be in a fairly reasonable agreement. An estimate of settling rate gives about 0.0019 cm/s. The transition zone A1 is estimated to be about 3.7 cm, at 5 cm below melt surface.

In the sedimentation pattern of the 20 vol% SiC too, five zones are identified in the sedimentation patterns of, A, A1, B, C and D. The region A is shallow, whilst the final sediment stretches from the bottom to cover almost three-quarters of the total melt height. An estimation of average SiC concentration of the final sediment using figure 4.1 puts this at about 30 vol%. Equation (61) gives about 28 vol% SiC. Settling rate is comparatively very slow, estimated at 0.00067 cm/s. The thickness of the zone A1 at 5 cm below melt surface is estimated to be about 3.4 cm.

4.3 PLOT OF SETTLING RATE DATA

Table 2 gives estimates of the floc volume fractions in the 7.5, 15 and 20 vol% SiC MMCs. Figure 4.26 is a plot of floc volume fraction against the volume fraction of particles using this data. There appears to be a linear relationship between the two quantities (possibly, a proportional relation). The floc-solid coefficient, C_{FS} , obtained from the slope of this plot is about 2.

Table 2. Data for estimation of floc volume fraction in 7.5, 15 and 20 vol% SiC MMCs.

$\theta_{\rm s}$	Z ₀₁ (cm)	Z ₀₂ (cm)	Z _n (cm)	Z ₁₂ (cm)	$\theta_{_{\mathrm{F}}}$
0.075	20	22.5	5.3	6	0.16
0.15	24.5	26.5	11.5	12.46	0.29
0.20	26	28	14.6	15.9	0.41

A plot of the settling data according to equation (48) is seen in Figure 4.27. The plot, essentially, can be viewed as consisting of two distinct regimes, a regime of rapidly decreasing settling rates followed by a linear regime. Settling rates in this regime are typically higher than predictions of the Richardson-Zaki equation. At 2.5 vol\% SiC ($\theta_{\rm F}$ ~ 0.05), where the settling rate was too high to be shown in the plot, it is as much as 9.2 times the prediction of the Richardson Zaki equation. The deviation diminishes with increasing SiC concentration and at 7.5 vol% SiC, settling rate is only about 1.7 times the Richardson-Zaki prediction. The second part of the settling data gives a straight line in accordance with the equation (48). Settling rates in this regime are more or less close to or below predictions of the Richardson-Zaki equation. Settling rate of the particles at 10 vol% SiC (θ_F ~ 0.2) is only about 1.2 times Richardson-Zaki prediction. Setting rates at 15 ($\theta_F \sim 0.3$) and 20 ($\theta_F \sim 0.4$) vol% SiC are about 0.96 and 0.46 times Richardson-Zaki predictions respectively. An estimate of the aggregate-floc coefficient, C_{AF} from the abscissa intercept of the straight line portion of the plot gives about 2.4. The diameter, d_p, of liquid flow pores also estimated from the ordinate intercept of the straight line portion of the plot is about 1.4 mm.

4.4 CHEMICAL ANALYSIS

Figure 4.28 relates the SiC volume fractions, nominal and probe determined, to the chemically determined. The chemically determined values were higher than the those determined by the other two methods. The slope of the regression lines are about 0.9 and 0.8 respectively for the nominal and probe determined.

The variation of SiC volumetric fraction (by chemical analysis) with time for the 15 vol% SiC MMC, during the settling, is shown in Figure 4.29. The results run parallel with that obtained using the probe (figures 4.16 to 4.18). At 6 cm below the surface, the SiC content stayed approximately constant at 16 and 14.5 vol% respectively for the chemically and probe determined. After passing through the transition stage, they settled at about 3 and 2 vol% respectively after about 6000 seconds of settling. At 12 cm below the surface, the chemically determined started at a value slightly below 16 vol% and the probe determined, about 15 vol%. There were slight increases in both until about 4000 seconds of settling when they passed through the transition stage and both settled around 3 vol%, after about 10000 seconds of settling. At 18 cm below the surface, both did not indicate any drop in the SiC content. The chemically determined and probe determined stayed constant at about 17 and 16 vol% respectively, for about 2000 seconds and began to increase gradually to values of about 28 and 26 vol% respectively after 10000 seconds of settling.

Table 3, summarises the SiC concentrations at the various depths after the passage of the clarification front. SiC volumetric fraction at the specified depths in the 5 vol% SiC MMC reduces almost to zero. For the 10 vol% SiC MMC, the SiC content is much higher. The amount of SiC left in the clarified liquid is still higher for the 15 and 20 vol% MMCs. The average SiC content of the final sediment (table 3) for the 7.5, 15 and 20 vol% MMCs are only 27.9, 27.8 and 29.3 respectively. This suggest that the sediments are not very dense.

Table 3. SiC volumetric fractions (by chemical analysis) after passage of clarification front at various positions approximately in melt heights below surface.

Position	5 vol% SiC	10 vol% SiC	15 vol% SiC	20 vol% SiC
1/4 melt height	0.3	1.3	3.1	3.3
½ melt height	0.3	2.13	3.3	-
3/4 melt height	0.45	2.48	•	-

Table 4. Average SiC volumetric fraction (by chemical analysis) in the final sediment of 7.5, 15 and 20 vol% SiC MMCs.

7.5 vol% SiC MMC	15 vol% SiC MMC	20 vol% SiC MMC	
27.9	27.8	29.3	

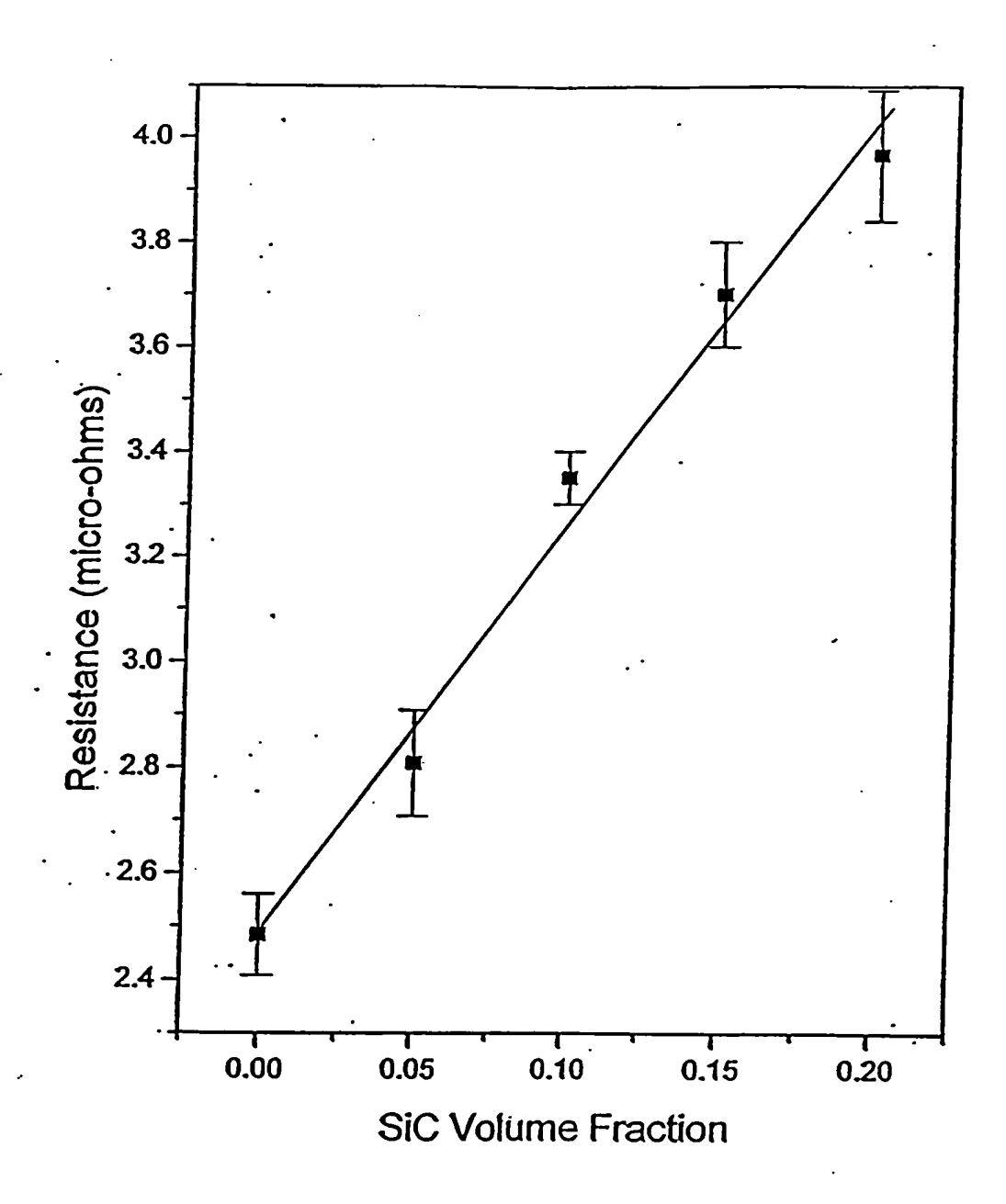
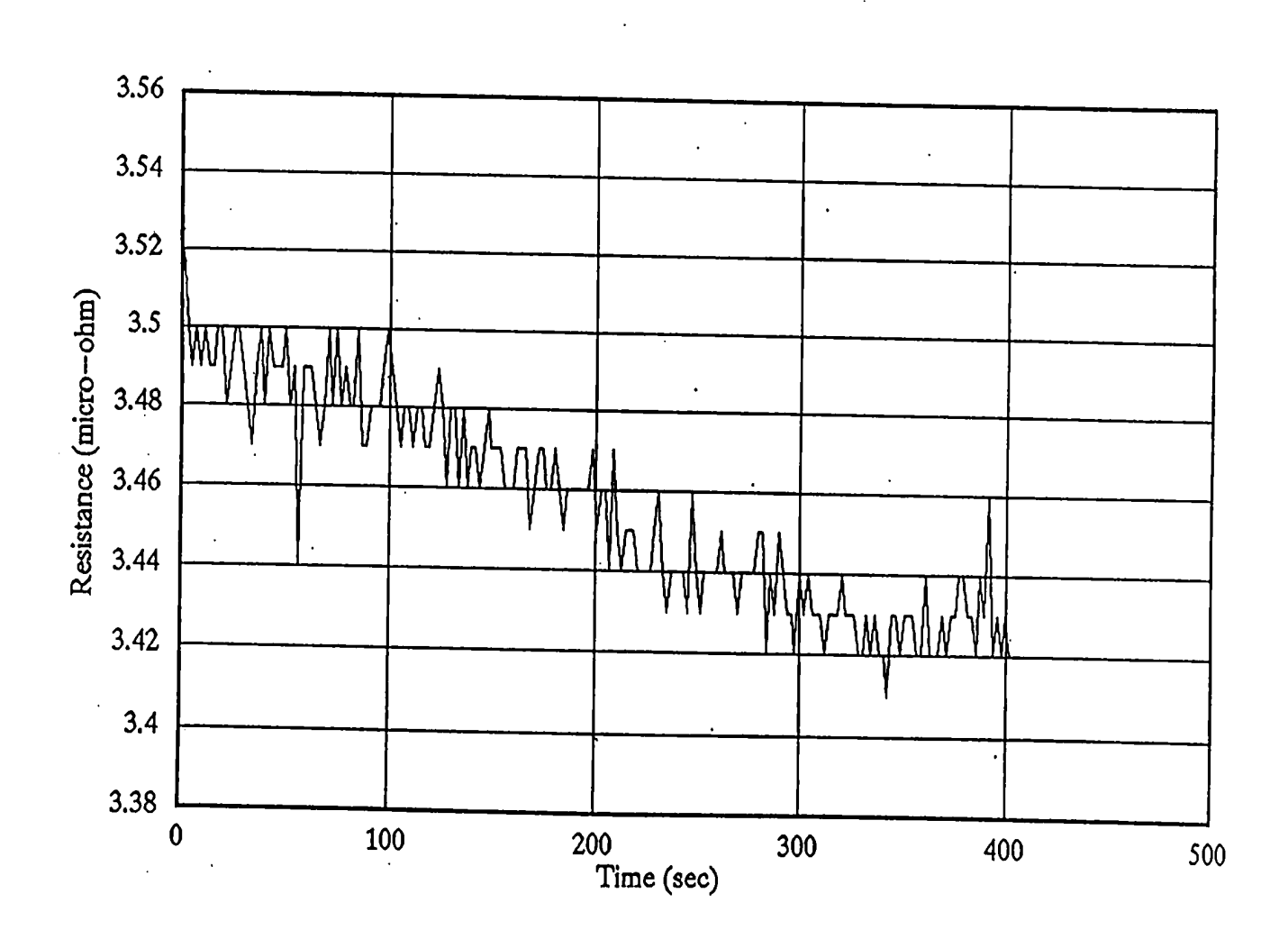


Figure 4.1 Variation of resistance with nominal SiC volume fraction.

Variation of resistance with time at 5 cm below the melt surface for 2.5



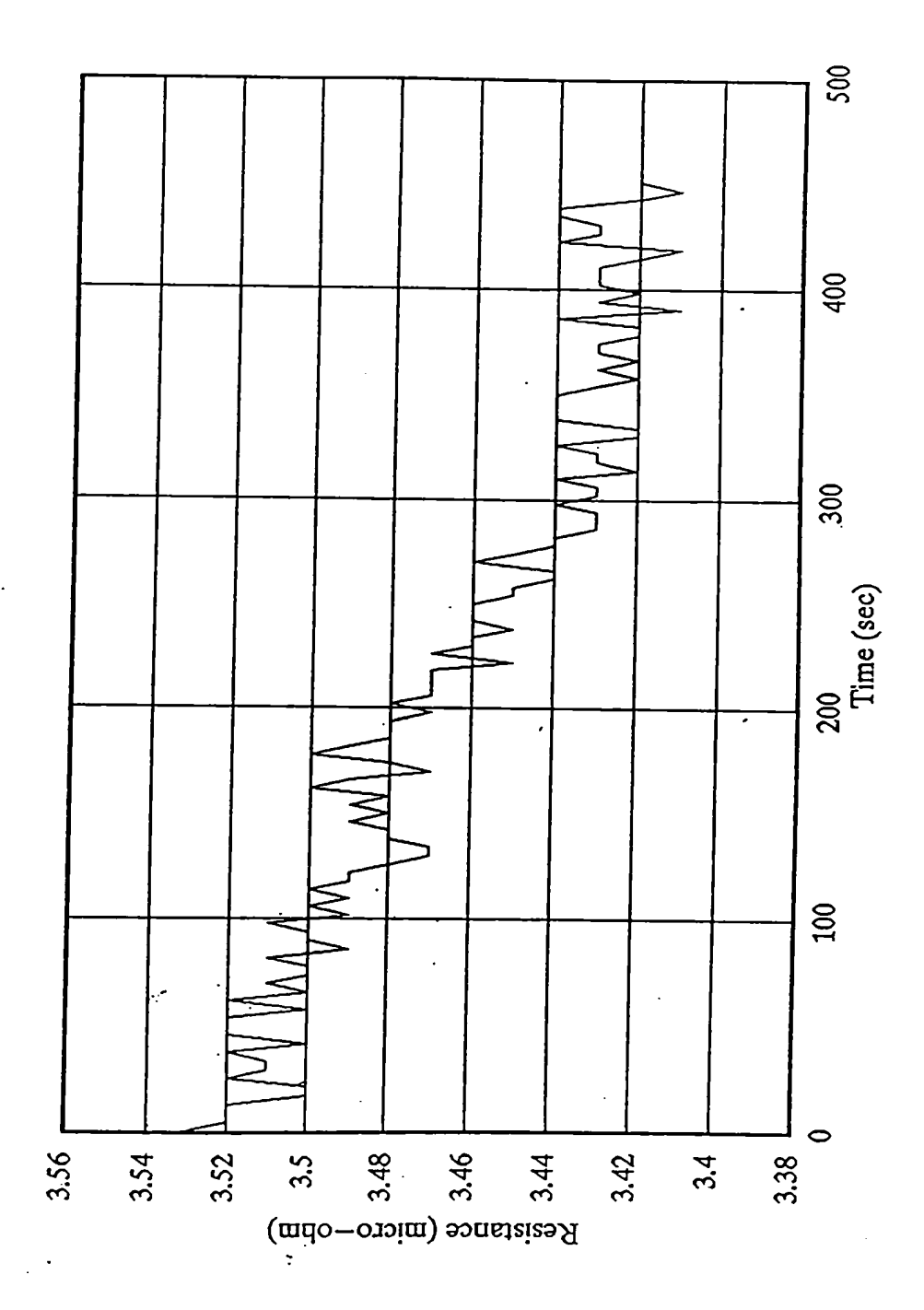
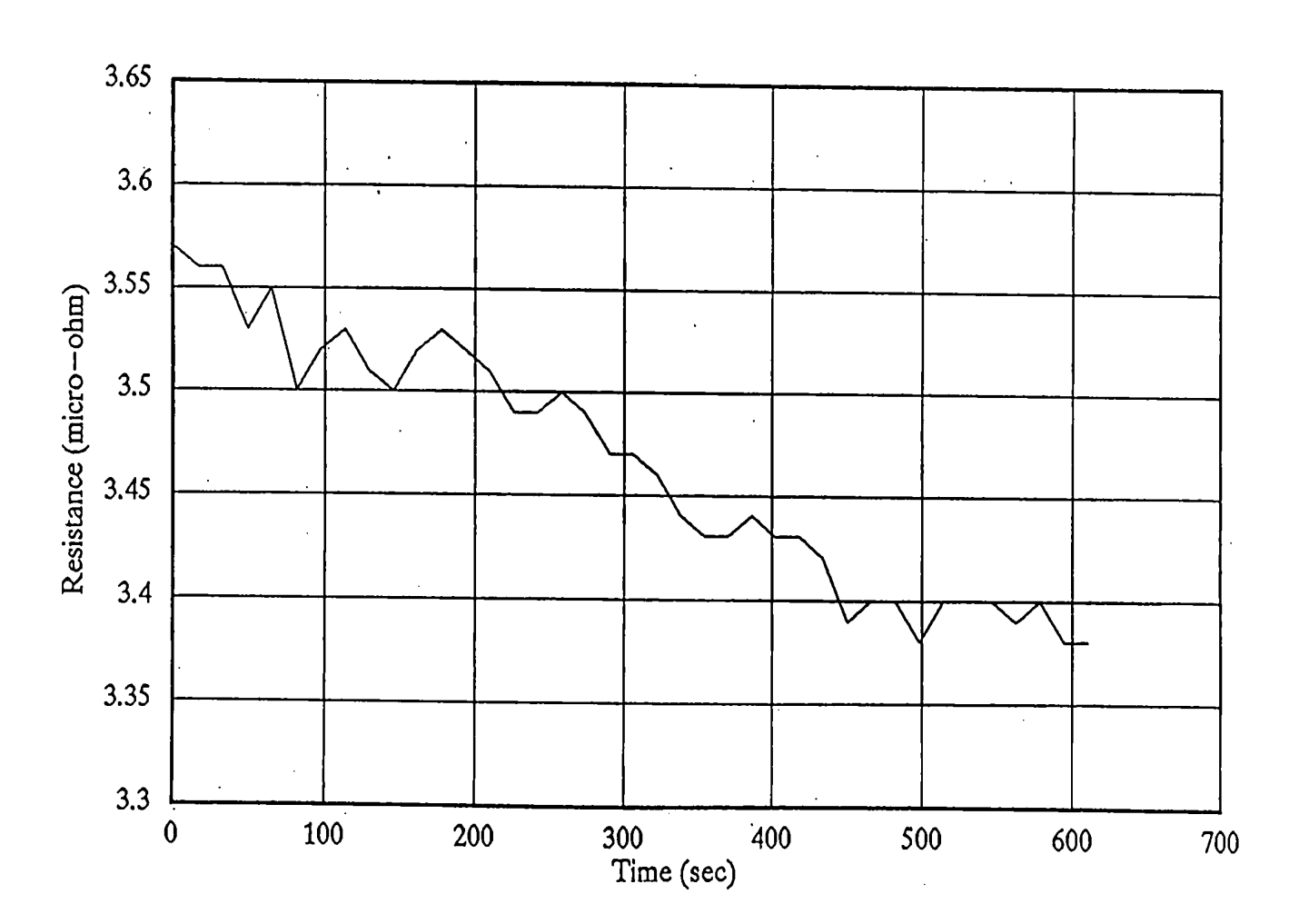
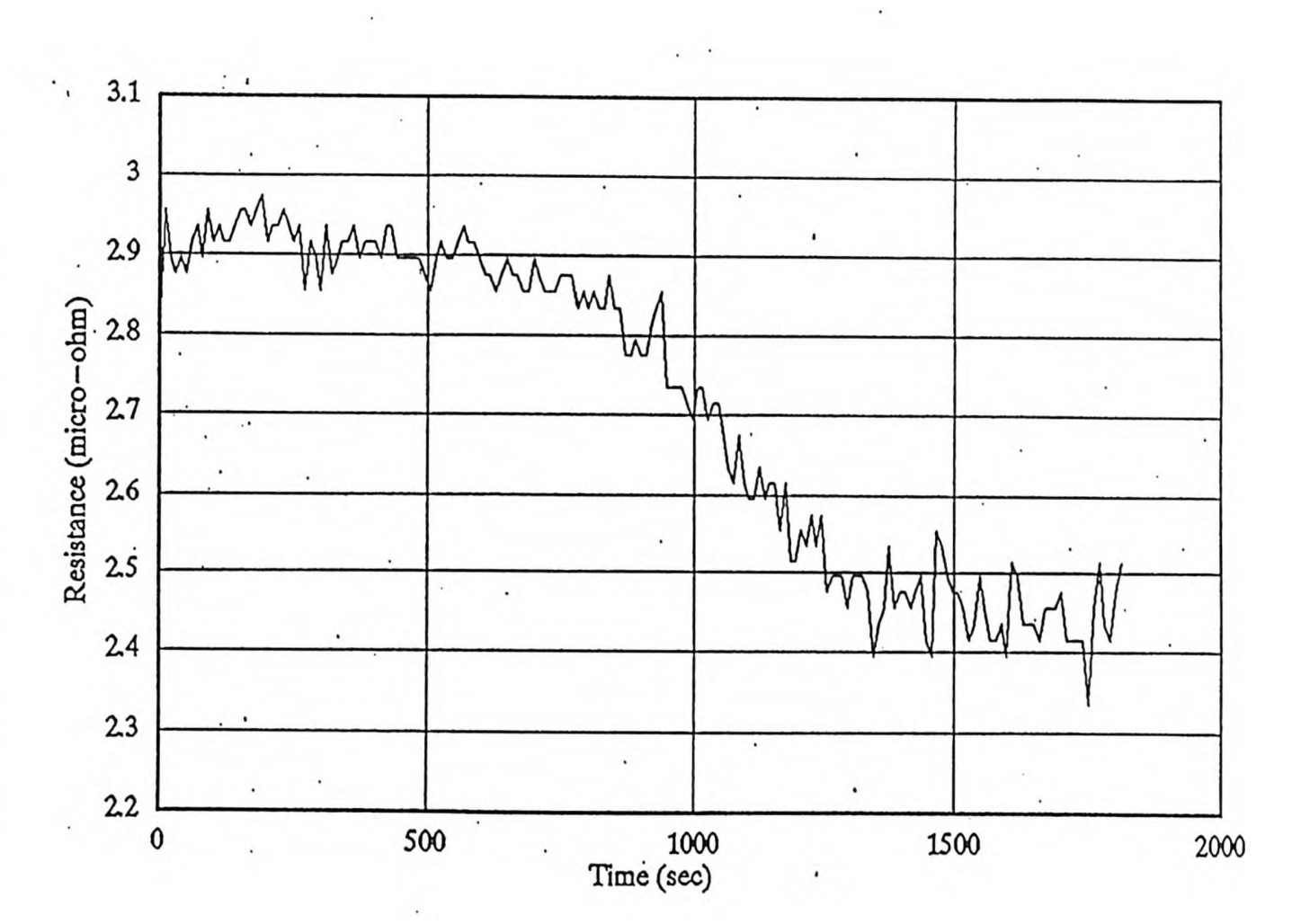


Figure 4.3 Variation of resistance with time at 10 cm below the melt surface for 2.5 vol% SiC MMC.

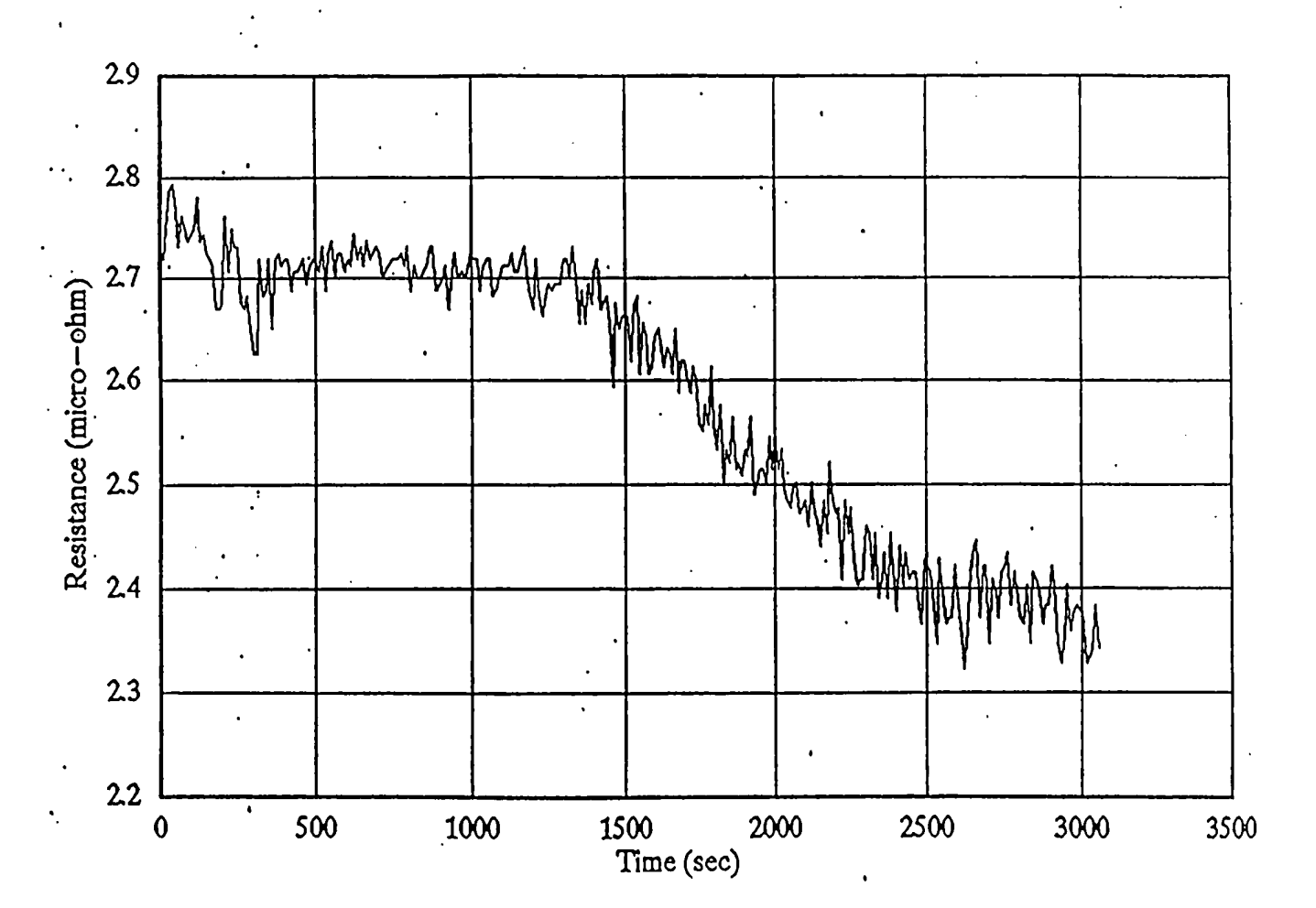
Figure 4.4 Variation of resistance with time at 15 cm below the melt surface for 5 vol% SiC MMC.



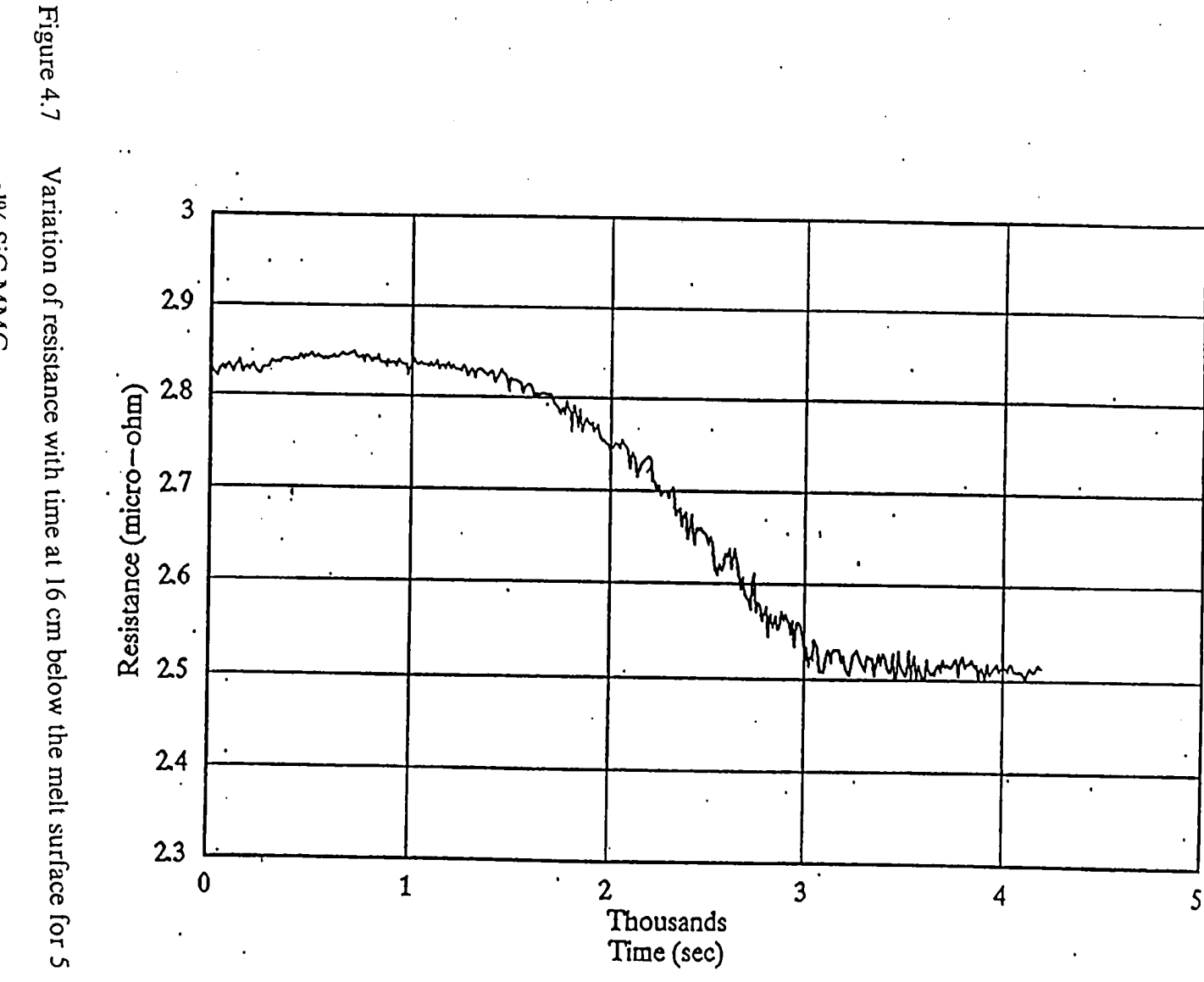
Variation of resistance with time at 5 cm below the melt surface for 5



62



Variation of resistance with time at 10 cm below the melt surface for 5



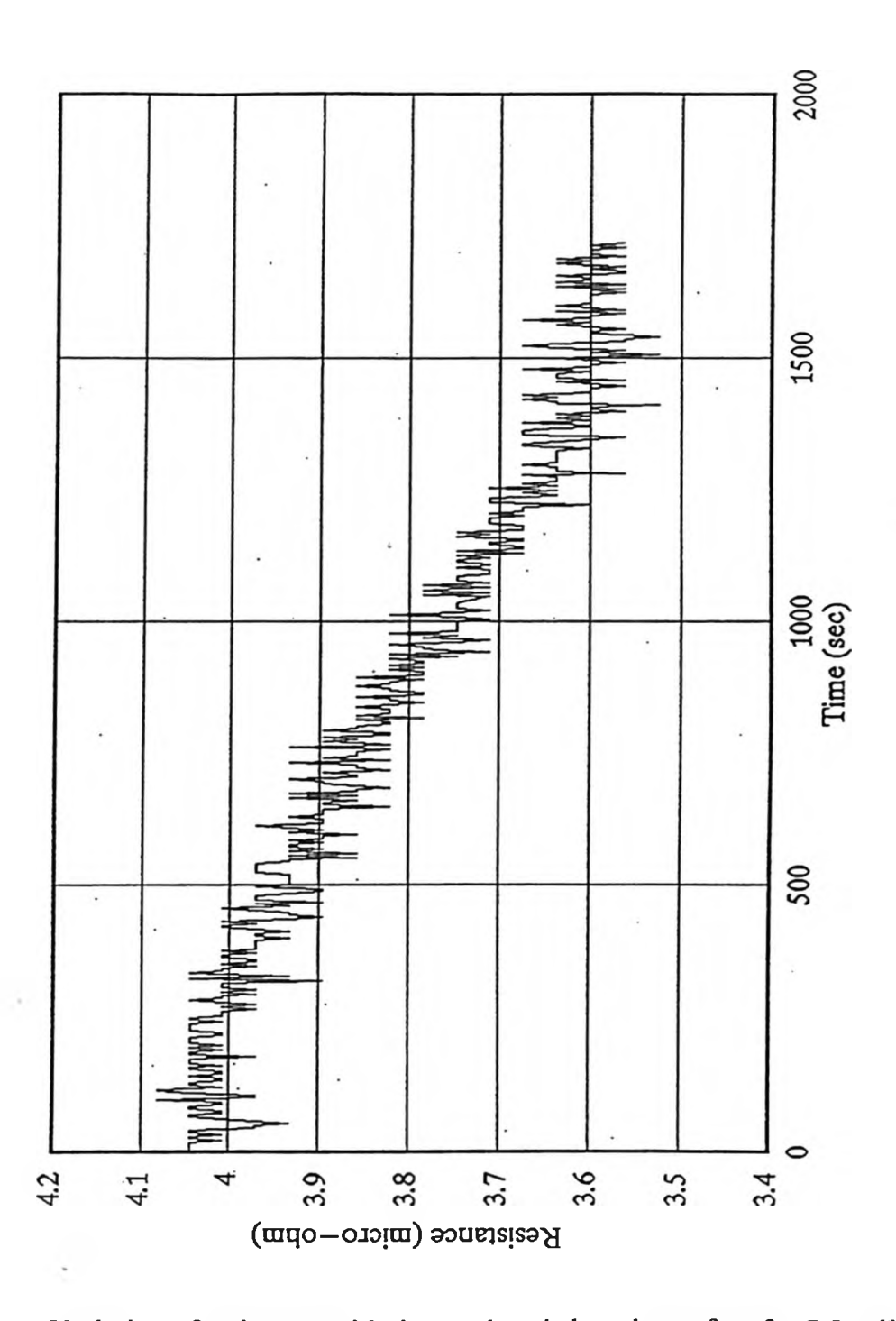


Figure 4.8 Variation of resistance with time at 6 cm below the surface for 7.5 vol% SiC MMC.

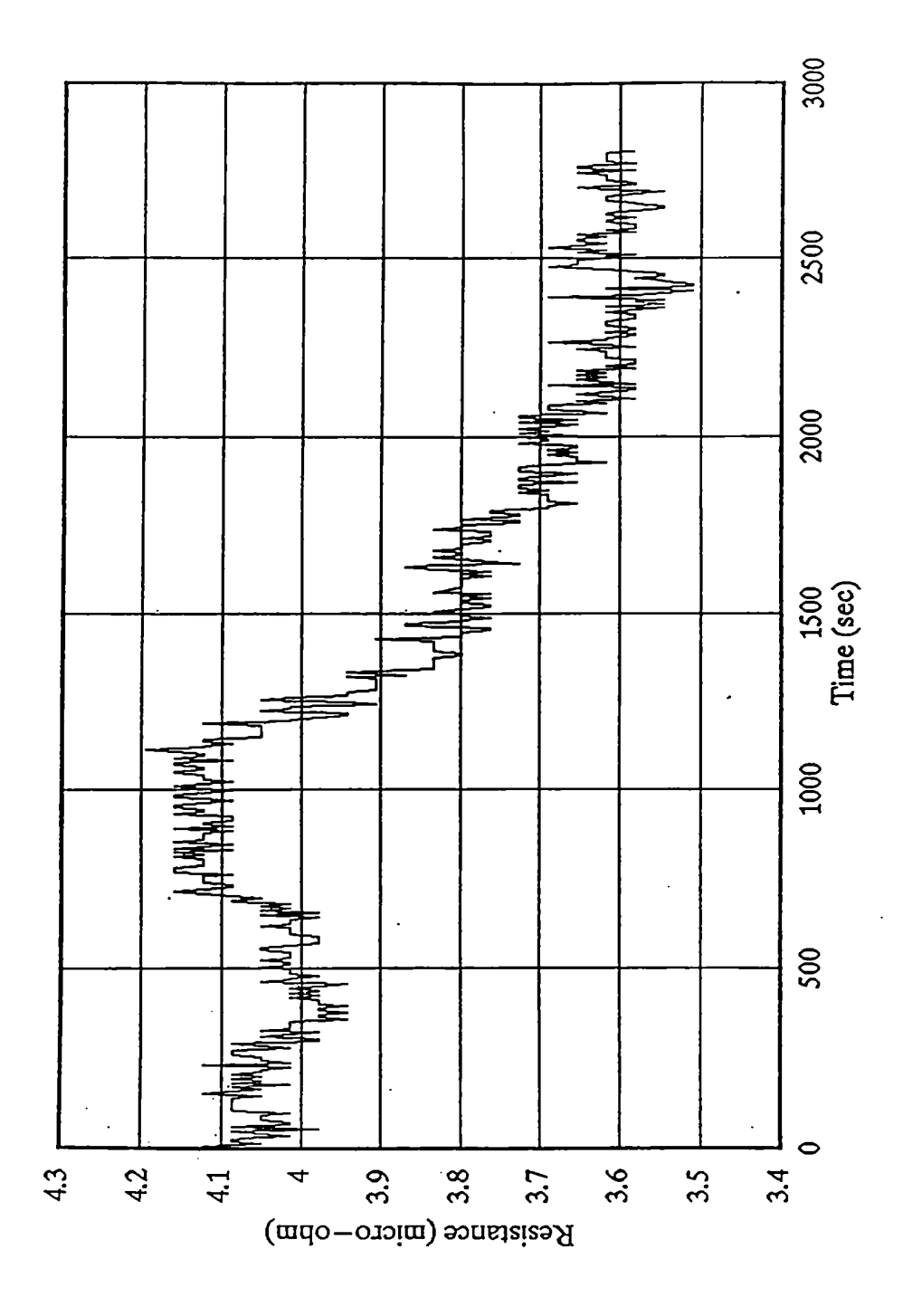
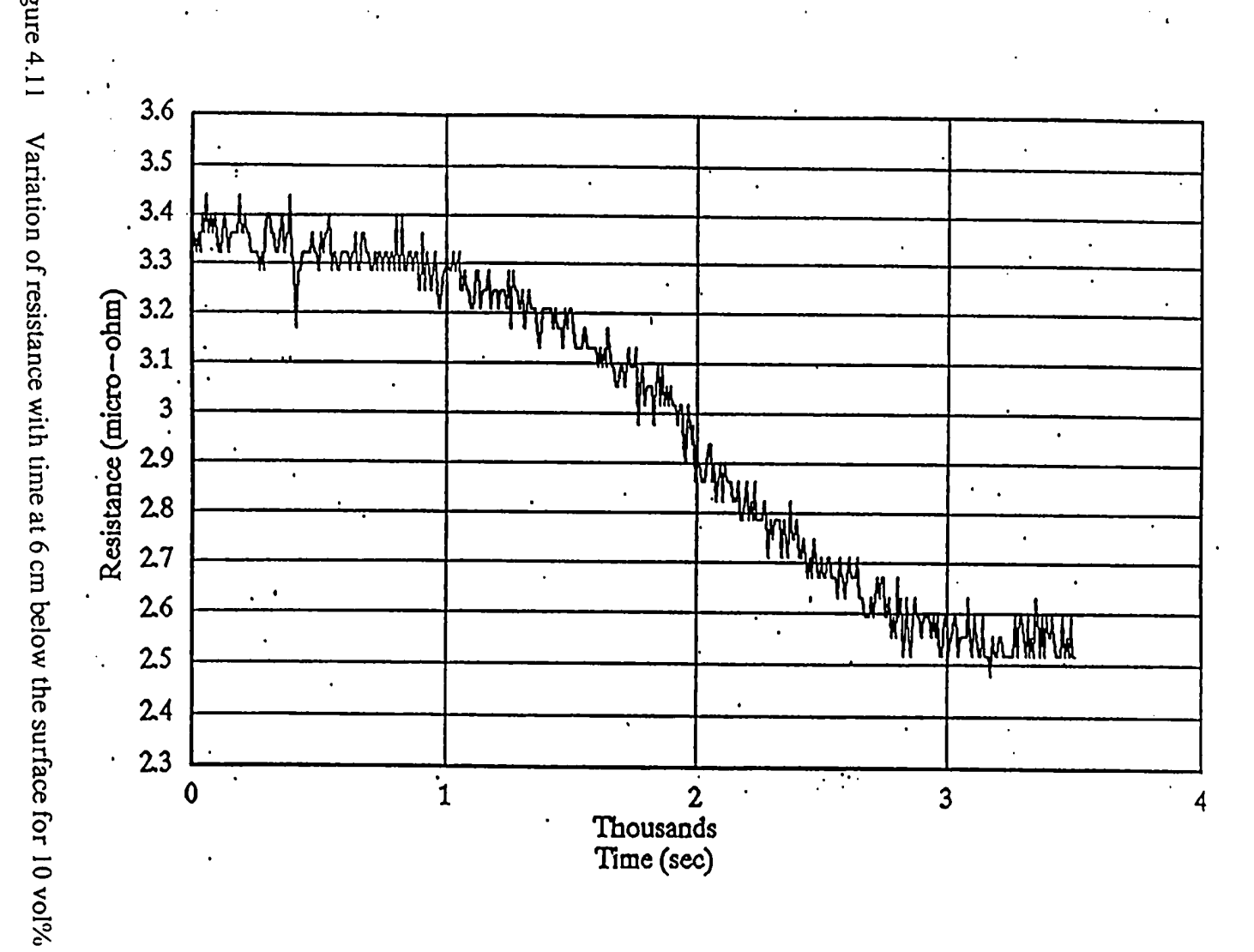


Figure 4.9 Variation of resistance with time at 12 cm below the melt surface for 7.5 vol% SiC MMC.

Variation of resistance with time at 17 cm below the melt surface for 7.5

4.5 4.4 4.3 Resistance (micro-obm) 4.2 4.1 4 3.9 3.8 3.7 3.6 Thousands Time (sec) 0 1 3

4



68

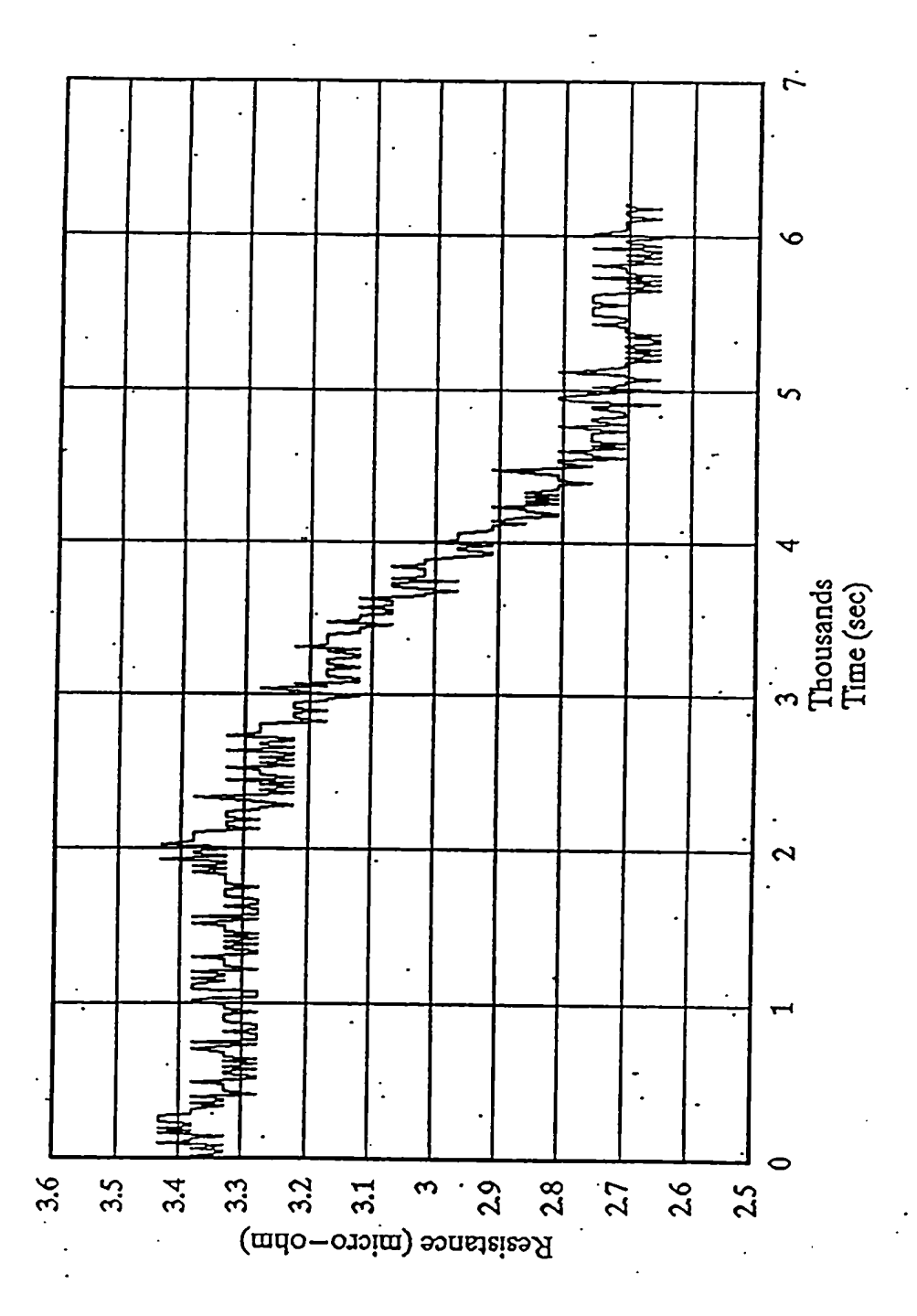


Figure 4.12 Variation of resistance with time at 12 cm below the melt surface for 10 vol% SiC MMC.

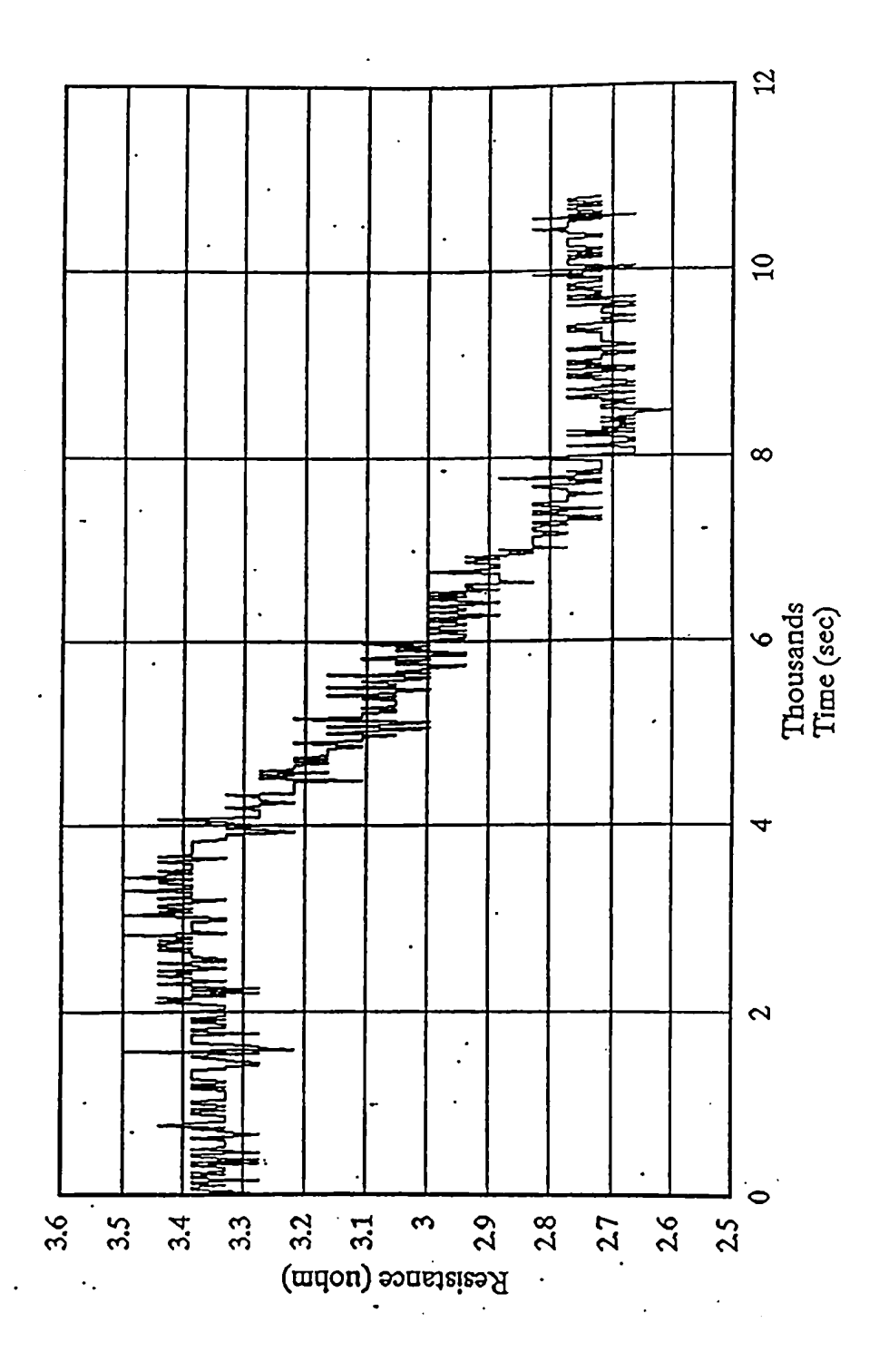


Figure 4.13 Variation of resistance with time at 17 cm below the melt surface for 10 vol% SiC MMC.

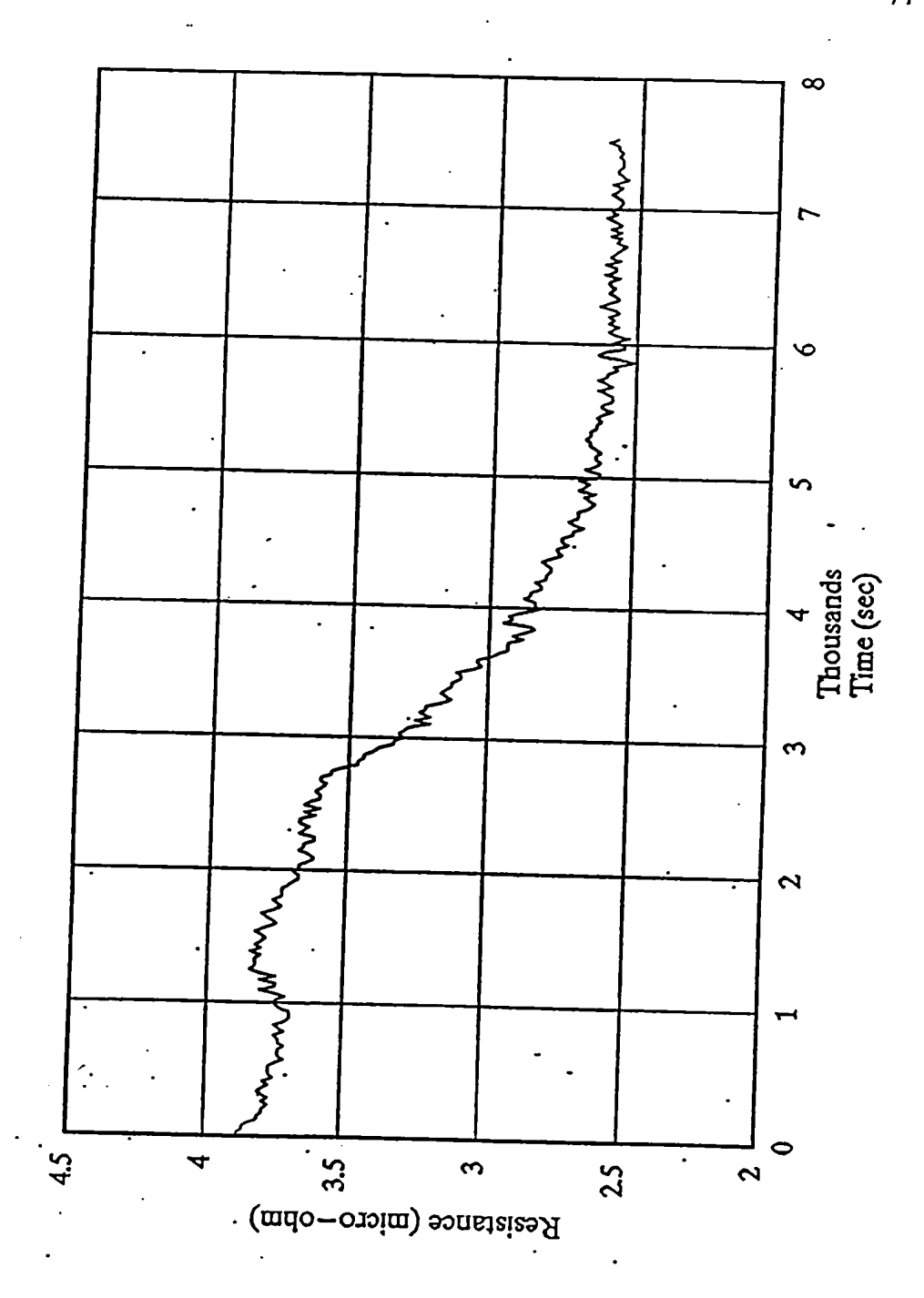


Figure 4.14 Variation of resistance with time at 6 cm below the melt surface for 15 vol% SiC MMC.

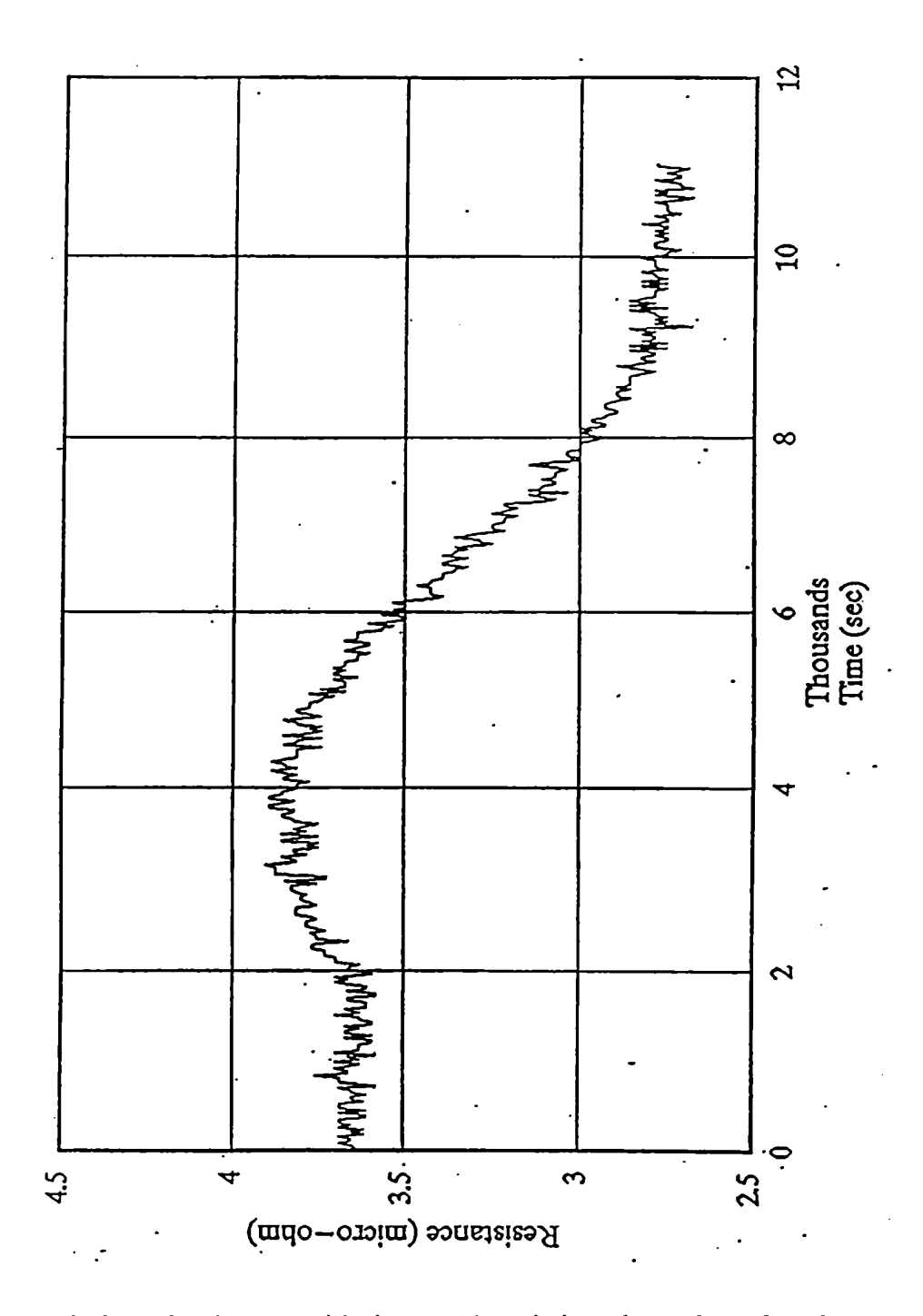


Figure 4.15 Variation of resistance with time at 12 cm below the melt surface for 15 vol% SiC MMC.

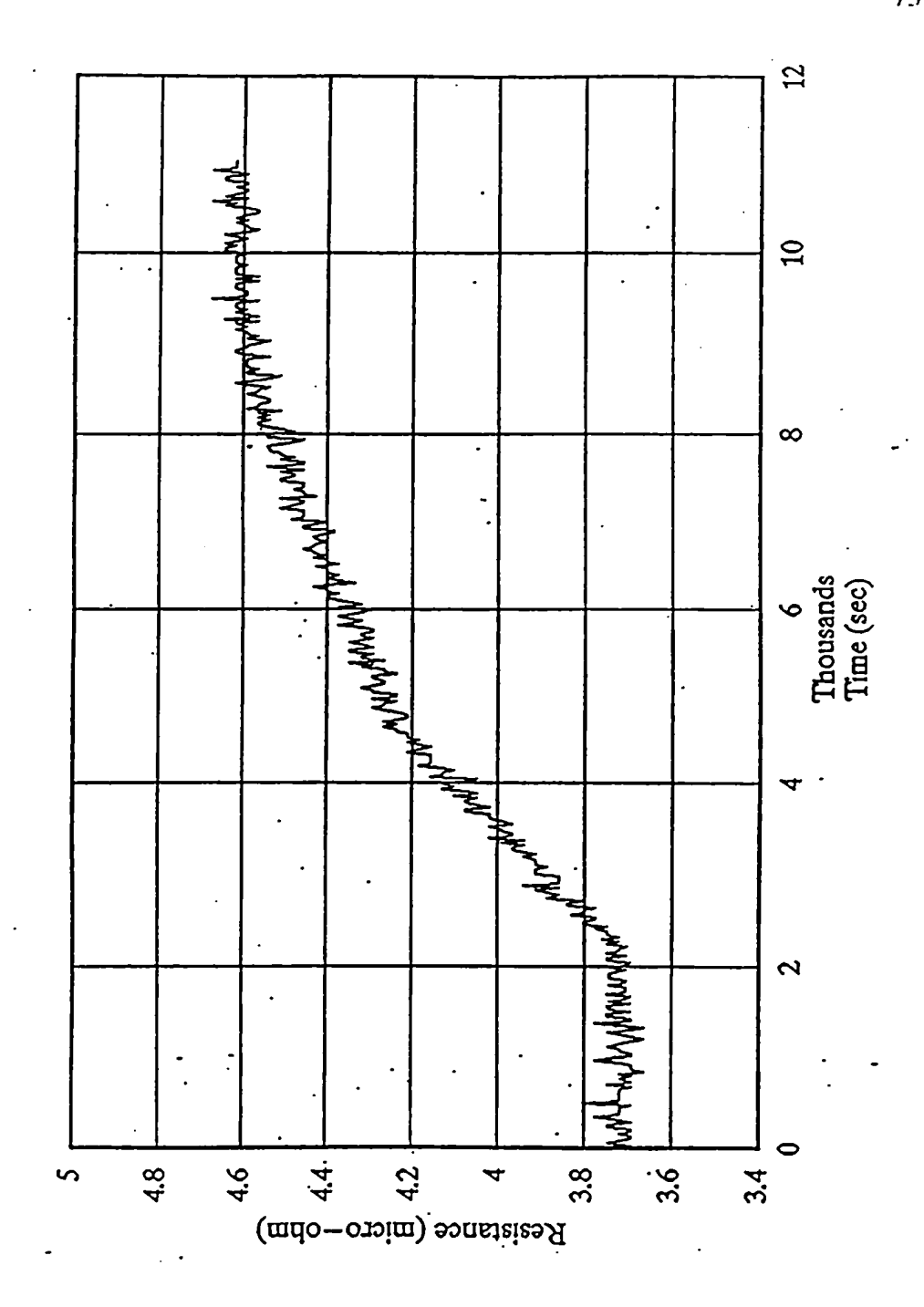


Figure 4.16 Variation of resistance with time at 18 cm below the melt surface for 15 vol% SiC MMC.

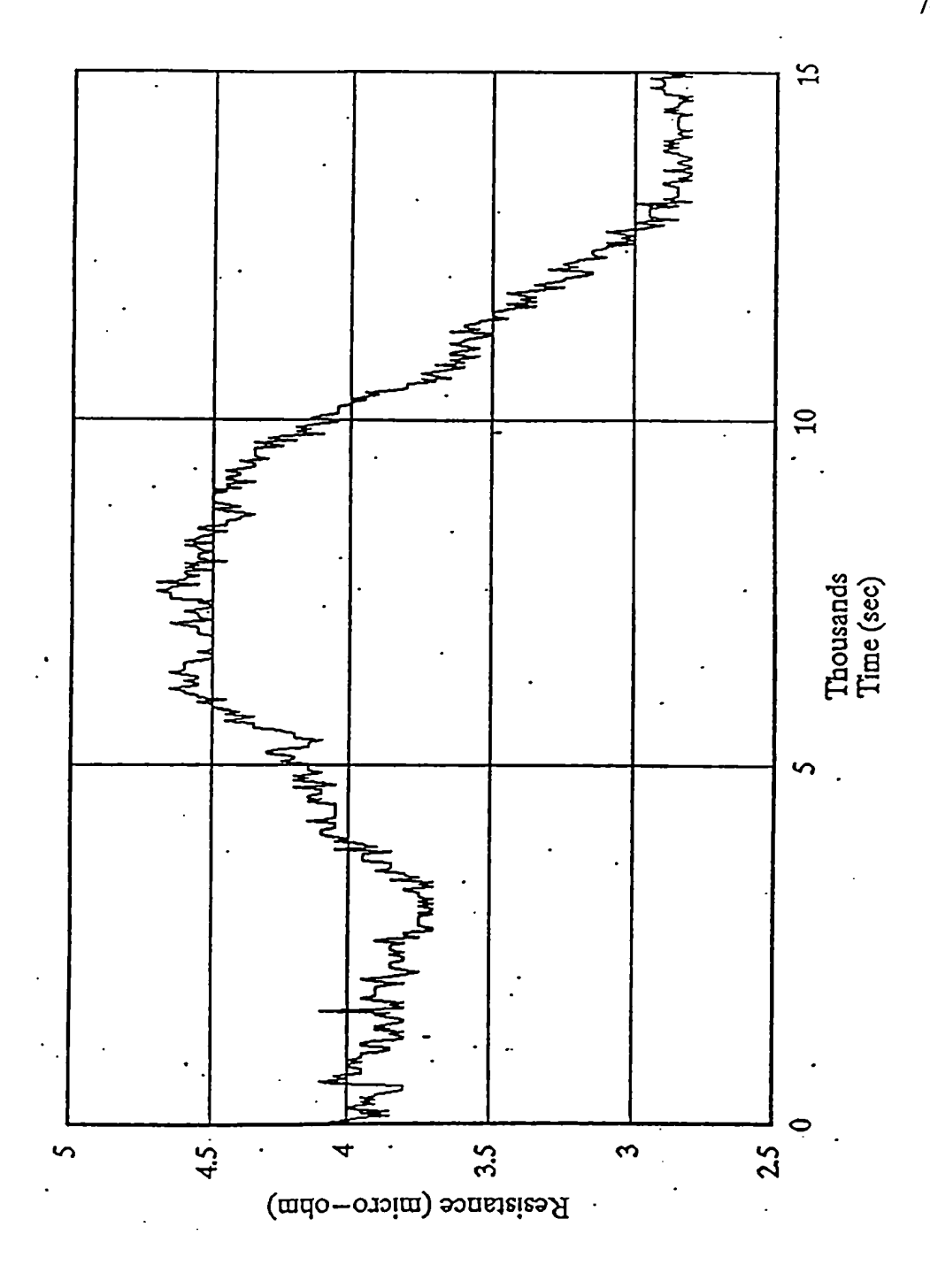


Figure 4.17 Variation of resistance with time at 7 cm below the melt surface for 20 vol% SiC MMC.

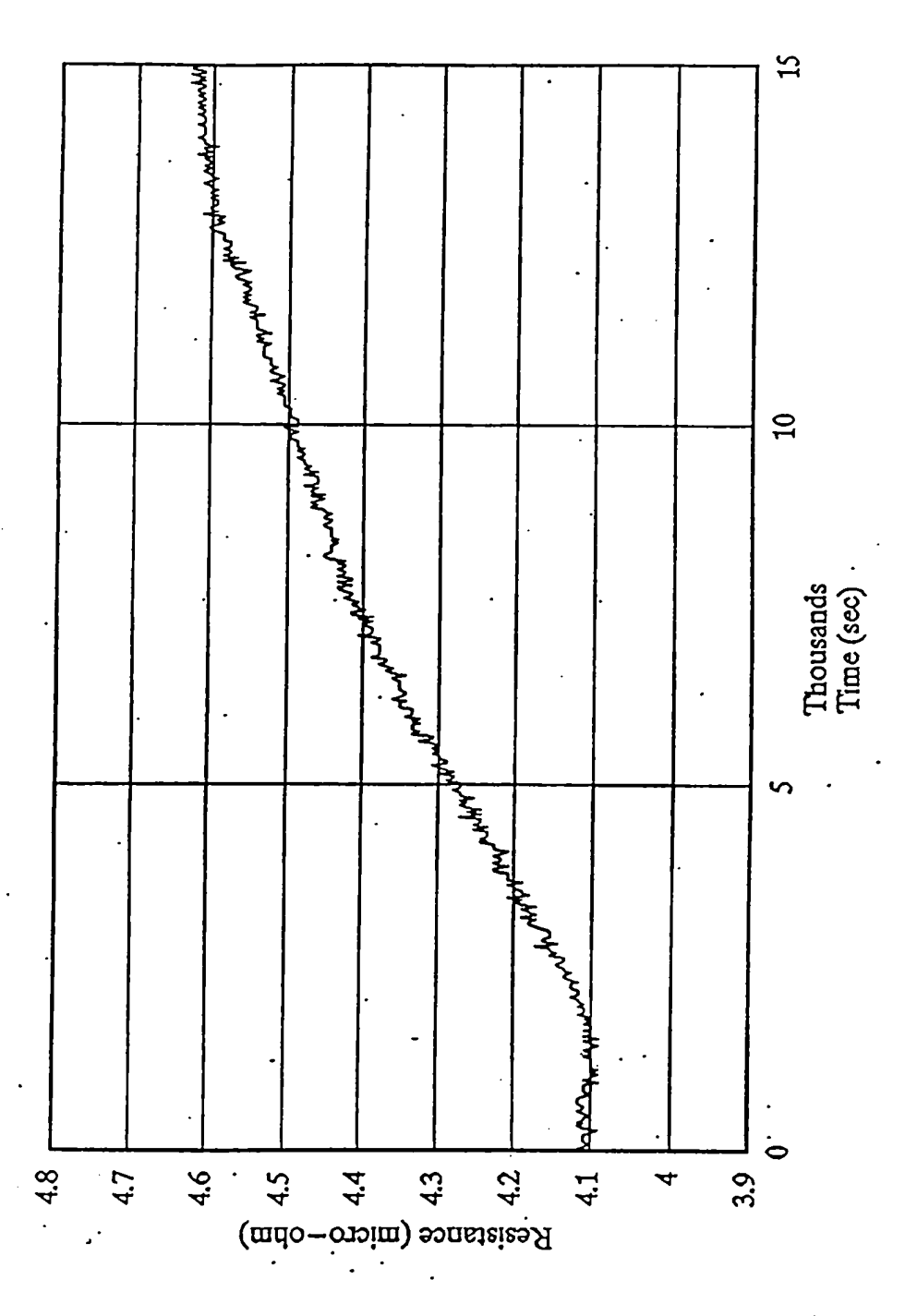


Figure 4.18 Variation of resistance with time at 13 cm below the melt surface for 20 vol% SiC MMC.

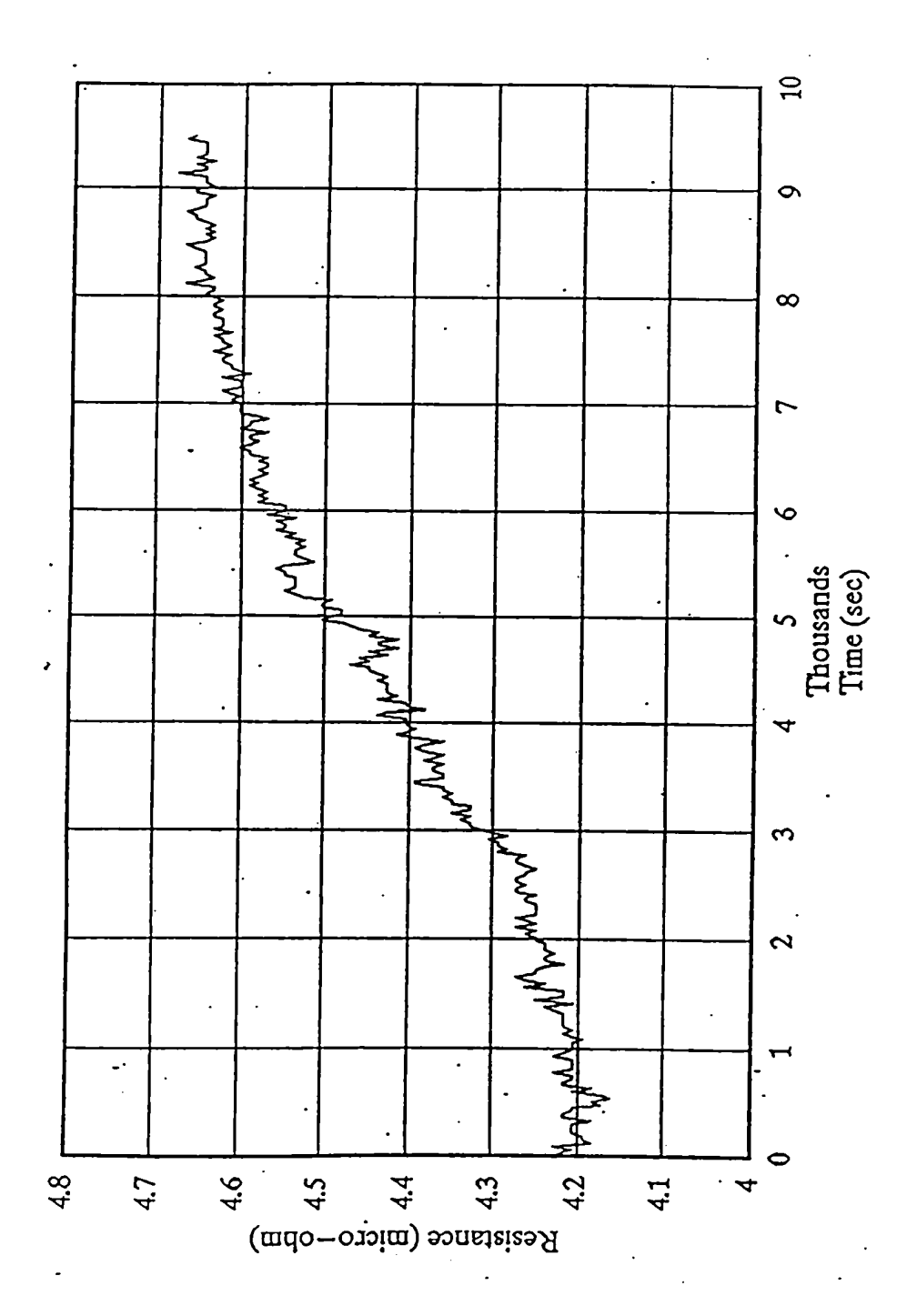


Figure 4.19 Variation of resistance with time at 19 cm below the melt surface for 20 vol% SiC MMC.

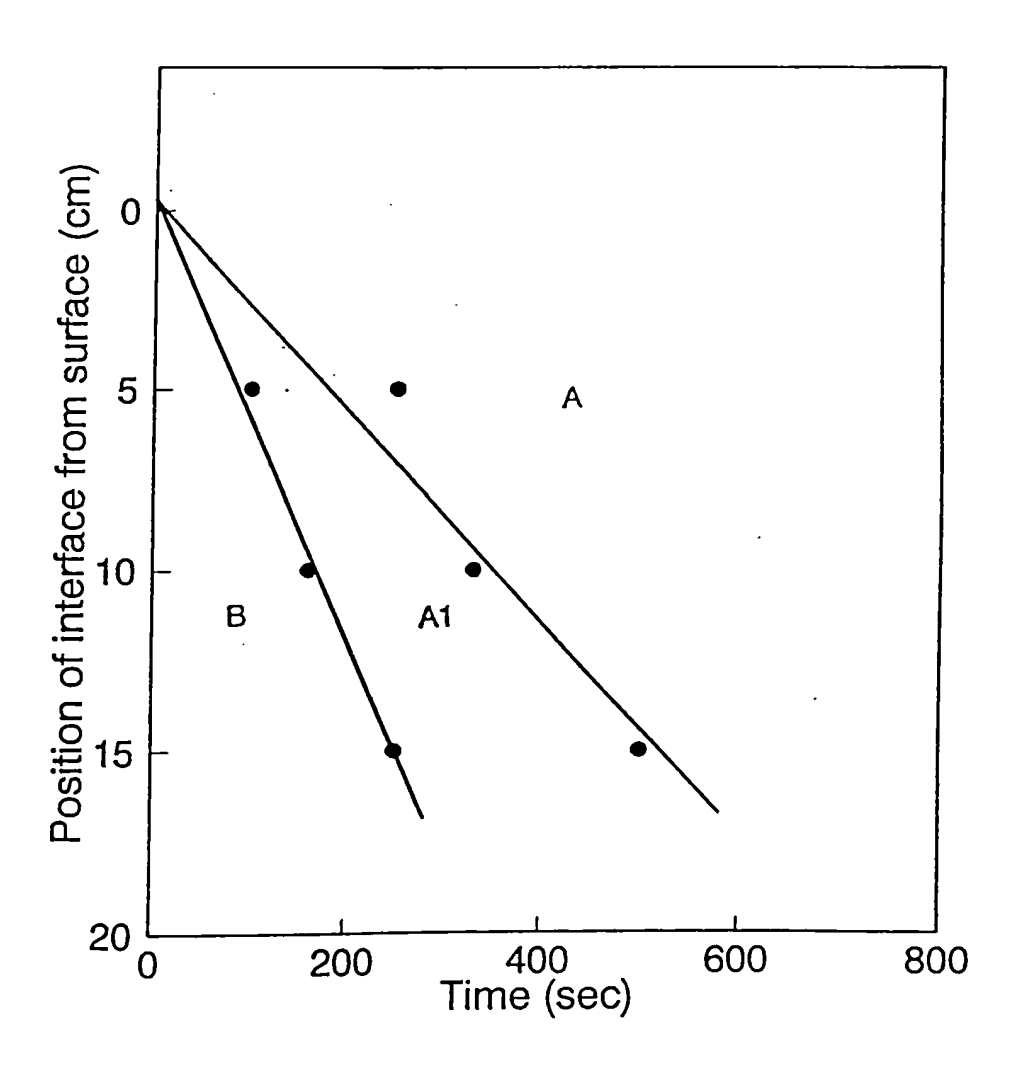


Figure 4.20 Time to pass from the initial volume fraction region B, to the clarified region A, for 2.5 vol% SiC MMC

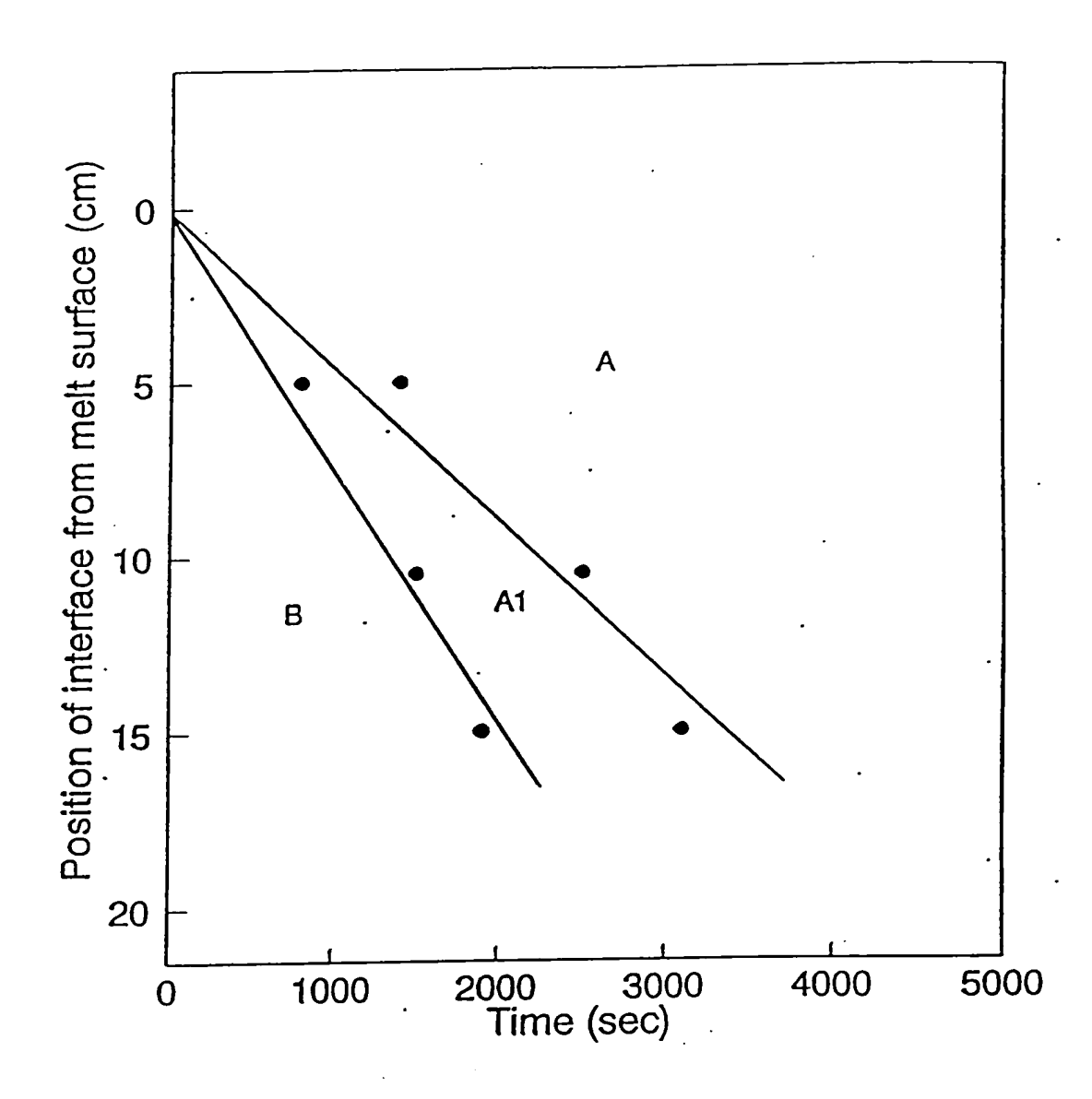


Figure 4.21 Time to pass from the initial volume fraction region B, to the clarified region A, for 5 vol% SiC MMC

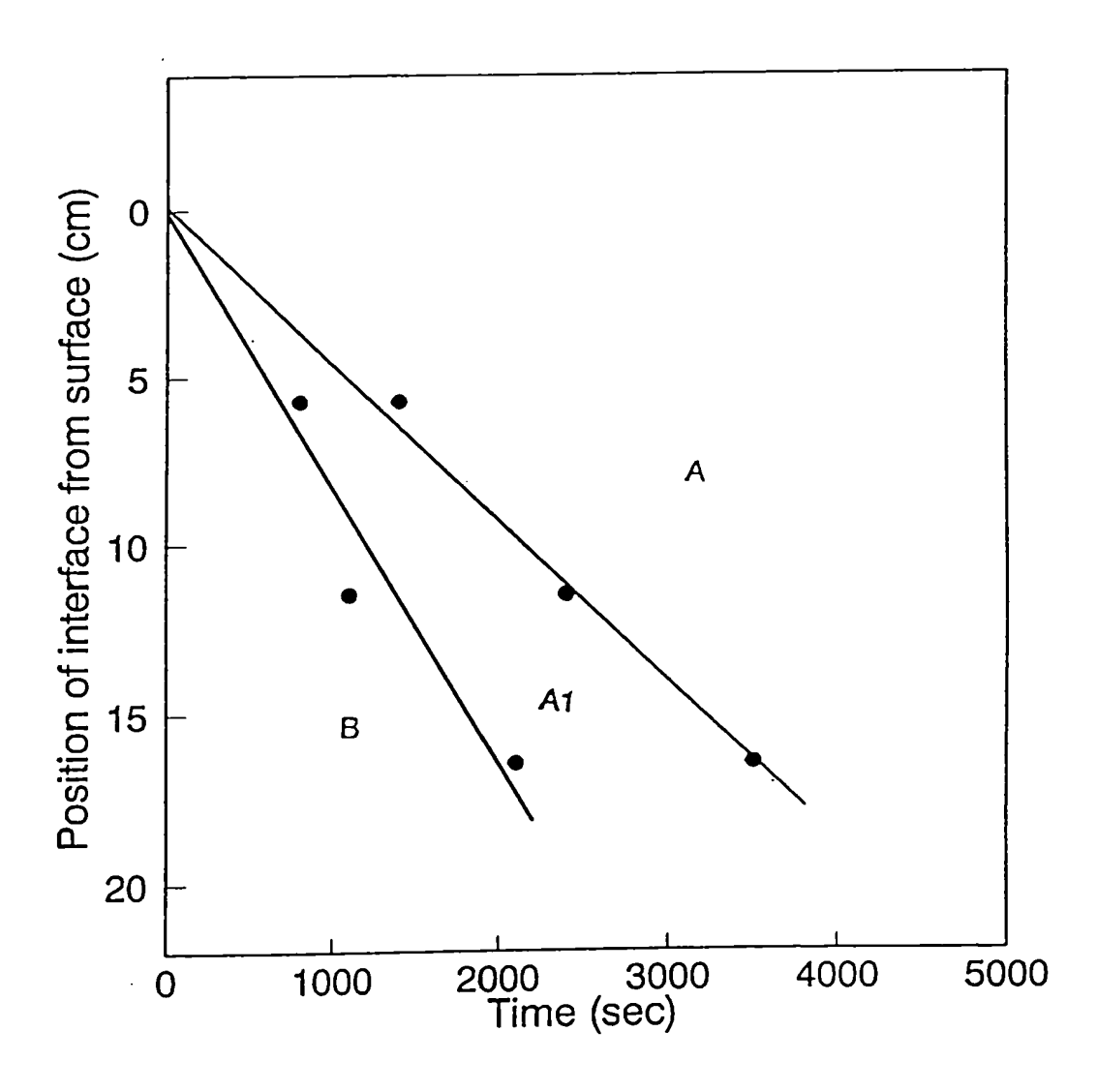


Figure 4.22 Time to pass from the initial volume fraction region B, to the clarified region A, for 7.5 vol% SiC MMC.

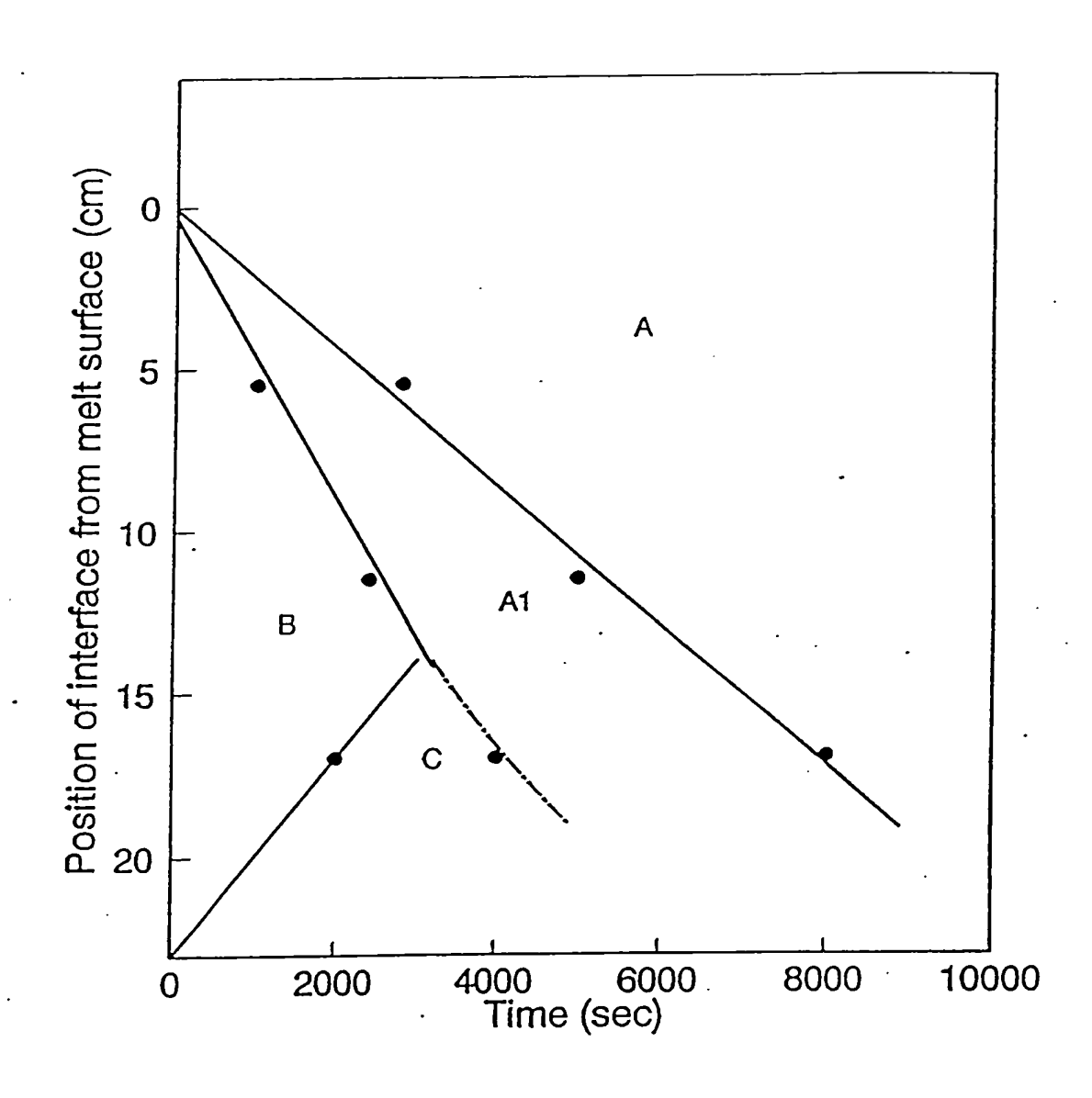


Figure 4.23 Time to pass from the initial volume fraction region B, to the clarified region, A for 10 vol% SiC MMC.

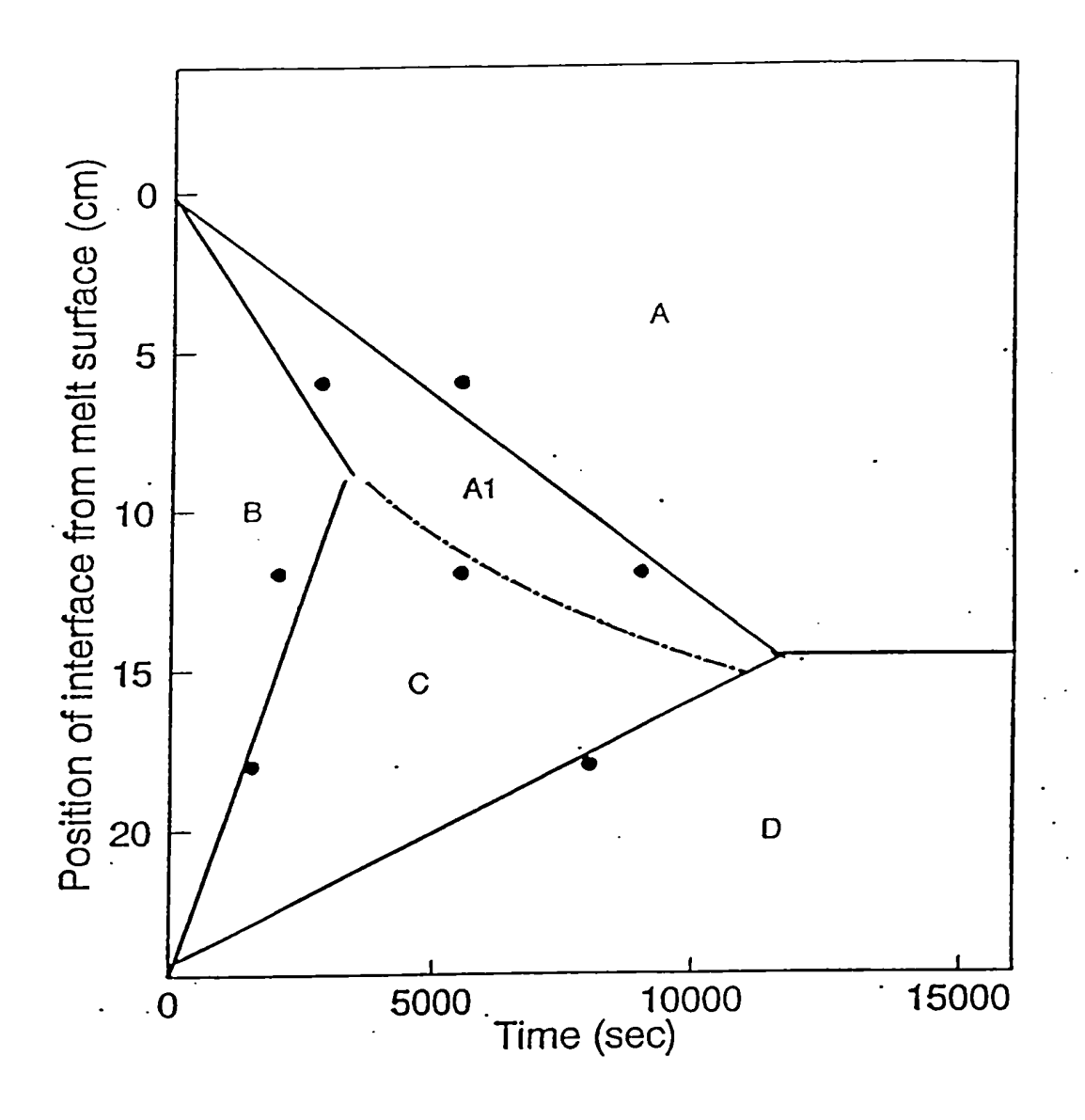


Figure 4.24 Time to pass from the initial volume fraction region B, to the clarified region A, for 15 vol% SiC MMC.

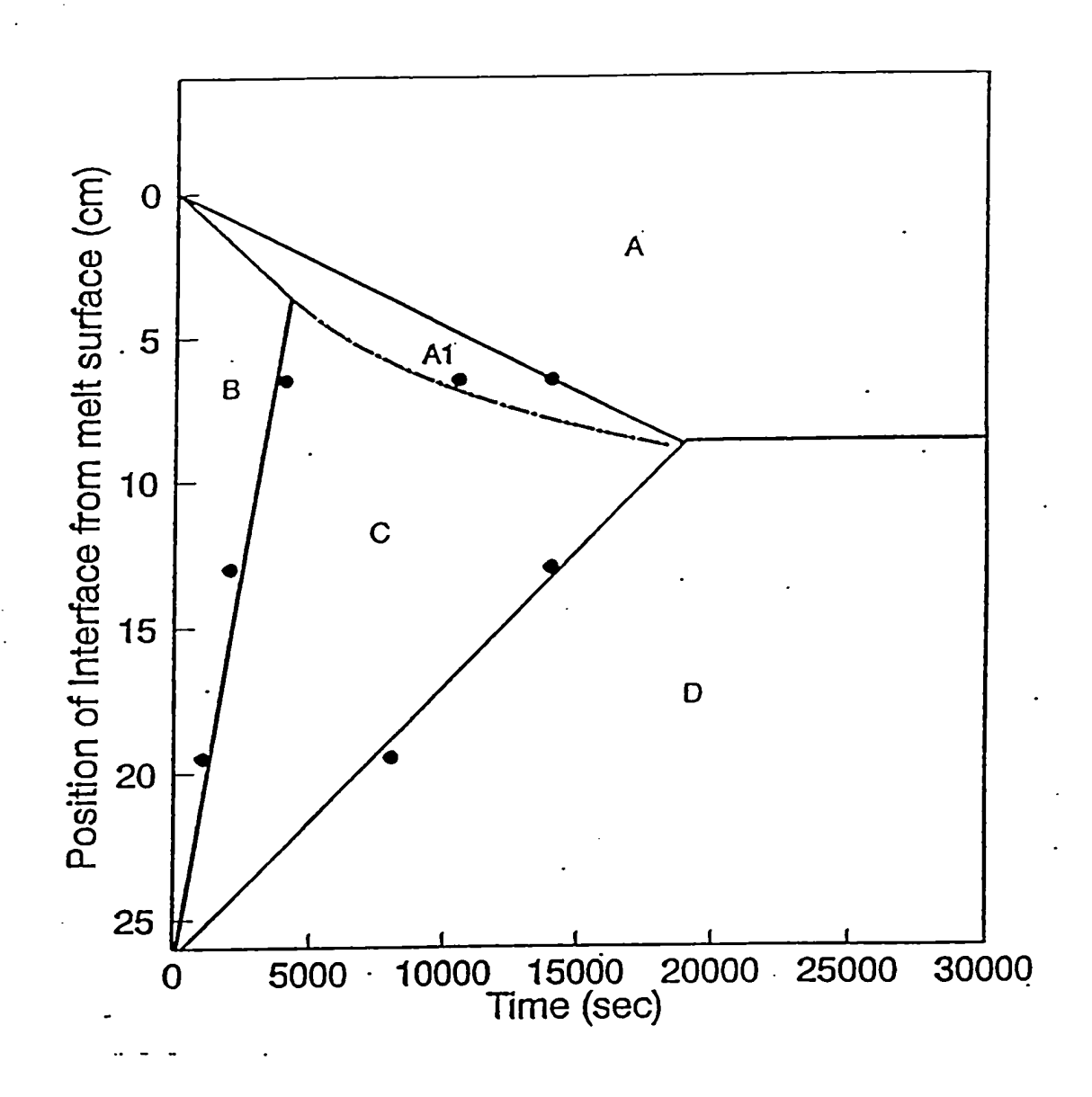


Figure 4.25 Time to pass from the initial volume fraction region B, to the clarified region A, for 20 vol% SiC MMC

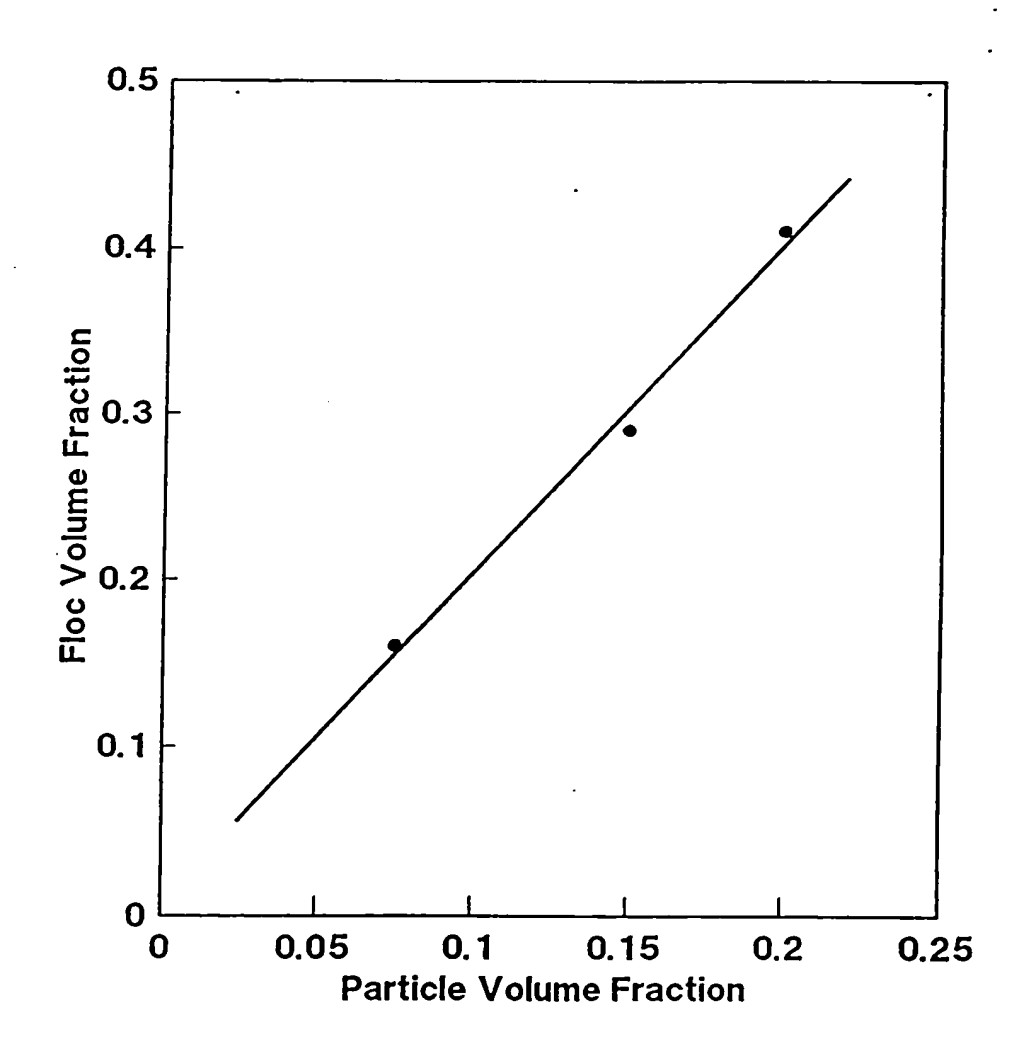


Figure 4.26 Plot of floc volume fraction against particle (SiC) volume fraction.

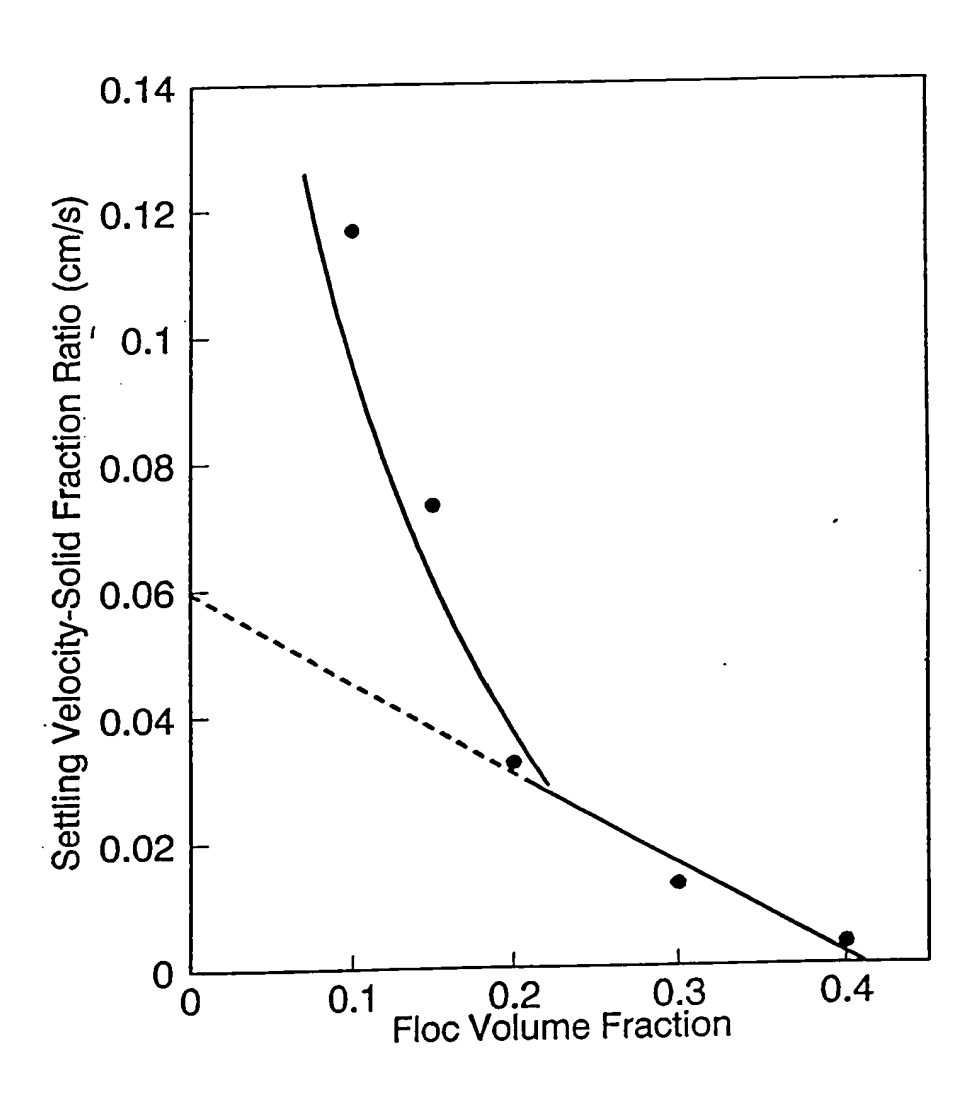


Figure 4.27 Plot of settling rate according to equation (48).

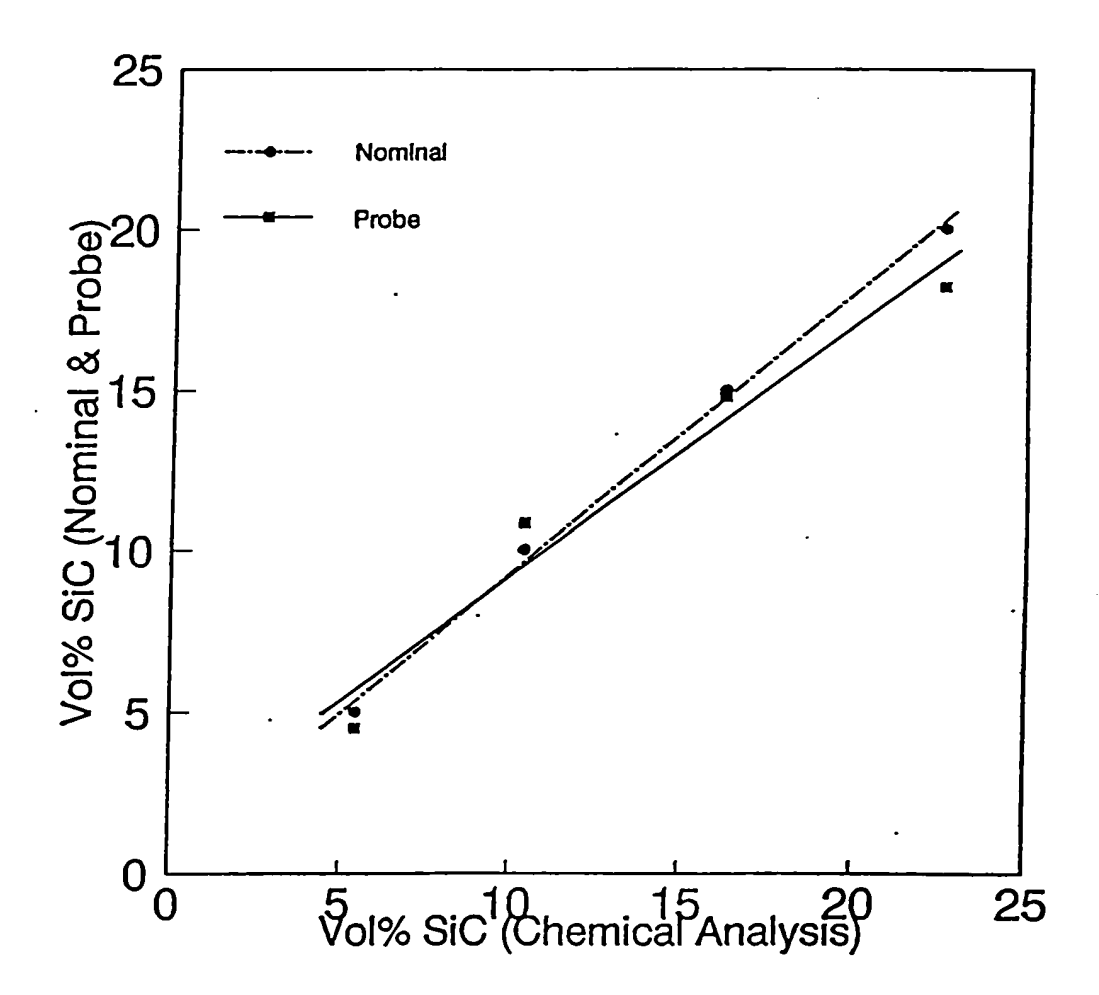


Figure 4.28 Comparison of nominal, probe and chemical estimations of SiC volume fractions in the MMCs.

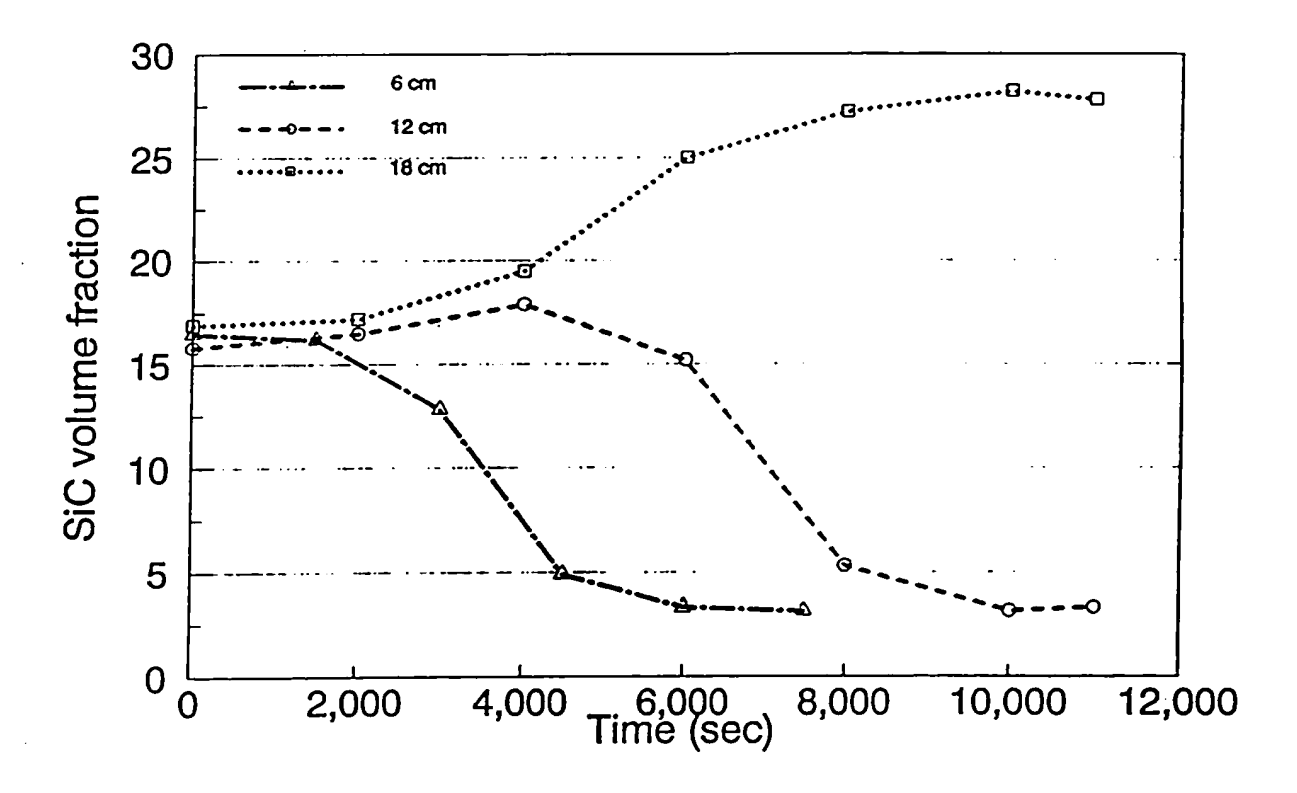


Figure 4.29 Variation of SiC volumetric fraction (by chemical analysis) with time for 15 vol% SiC MMC.

CHAPTER 5

DISCUSSION

5.1 THE PROBE

The most important challenge of this investigation was the means to monitor the sedimentation of the particles in an opaque system such as this, at a high temperature. The modified probe was a source of concern. It was less sensitive than the original [7]. Results were not reproducible sometimes, and this can be attributed to possible oxidation of the tungsten wires at the high temperature. The probe cannot be described as a non-intrusive one. The base measured $9 \, \text{cm} \times 6 \, \text{cm} \times 2.5 \, \text{cm}$. The suspicion was that such a large object in the melt had the potential to alter the flow behaviour around the probe location and significantly affect the results. However, the similarities between the general shapes of the probe outputs and that obtained entirely by chemical analysis for the 15 vol% SiC MMC eased these concerns.

To measure resistance by the four-point probe method, the micro-ohmmeter delivers constant current in the order of several tens of amperes. In this investigation, the current of about 20 amperes was delivered for several hundreds of seconds. It should be noted that the TECRAD DMO-350 is designed to deliver (d.c.) current in the form of pulses lasting for only 30 ms at a time and relaxes for at least 2 seconds between pulses. This reduces errors that may be introduced by polarization of the SiC particles and also eliminates errors arising from local overheating to ensure thermal stability at

probe location.

Resistances obtained at one-quarter and three-quarters of melt height below melt surface were in most cases slightly higher than at one-half melt depth below surface. In addition to the above mentioned problems of the probe, this may also be due to the fact that the closer the probe is to the surface or bottom of the melt the greater the chance of possible distortion of the electrical field of the measuring device. Hence the higher the resistance measured. These same reasons may be responsible for the slight differences between the initial SiC volume fraction determined by the probe and the nominal SiC volume fractions.

The differences in the SiC volumetric fractions obtained by chemical analysis and that obtained by the probe can be accounted for by contributing effects of the above mentioned problems of the probe and the fact that the probe readings are based on SiC volume fraction in liquid aluminum while those of chemical analysis are based on solid aluminum. When aluminum in the liquid phase at 660°C solidifies, there is as much as about 11% decrease in volume (ρ_{Al} (660°C) = 2400 kg/m³, ρ_{Al} (20°C) = 2698 kg/m³), also the coefficient of thermal expansion of aluminum (α_{Al} (300 - 800°K) = 23.2 - 33.8 × 10°6/°K) is more than four times that of silicon carbide, (α_{SiC} (0 - 1000°C) = 4.8 × 10°6/°K). These two factors can be responsible for the higher SiC volume fractions obtained by chemical analysis.

The resistance versus time curves shown in Figures 4.2 to 4.12 are typical for settling situations where the only significant change at the probe location is the passage

of the clarification front. In Figures 4.13 (10 vol% SiC, 17 cm below, melt height 23 cm), 4.15 (15 vol% SiC, 12 cm below, melt height 24.5 cm) and 4.17 (20 vol% SiC, 7 cm below, melt height 26 cm) an increase in resistance at the probe location is observed before the passage of the clarification front. This increase may be an effect of the rising sediment. In Figures 4.16 (15 vol% SiC, 18 cm below, melt height 24.5 cm), 4.18 and 4.13 (20 vol% SiC, 13 and 19 cm respectively, melt height 26 cm) where the probe does not register any decrease but only increased resistance, the probe is in a location where the dominant activity is the slow accumulation of the sediment.

5.2 INTERFACE POSITION VERSUS TIME CURVES

In all the interface versus position curves (Figures 4.20 to 4.25), settling from the initial volume fraction B to the clarified melt A, is not abrupt. There is a transition layer (zone A1) whose density may vary from that of B at the B/A1 interface to that of the clarified melt at the A/A1 interface. The thickest zone of 4 cm estimated at 5 cm below melt surface was in the 2.5 vol% SiC MMC and the thinnest of 3.13 cm in the 5 vol% SiC MMC. The mean thickness of all the zones in the six MMCs is about 3.5 cm and although no clear pattern of variation of zone thickness with SiC volume fraction could be deduced, the suspicion is that, unlike the transition zone in the MMCs of the coarse particles, the A1 zone thickness did not change with SiC concentration or perhaps, the change was too small to be accurately measured. The size of the zone in the MMCs of the fine particles is relatively small compared to that in the coarse particle MMCs. This seems to contradict the view that particle size distribution may be responsible for the

transition zone A1, in view of the fact that the standard deviation of the fine particle size is about 70% the average size and for the coarse particles only about 20% the average size.

The presence of the final sediment was sensed at a relatively lower SiC volume fraction in the fine particle MMCs than in the coarse particle MMCs. This is because the settled beds in the former were less dense and therefore much higher. The average concentration of SiC particles in the final bed of these MMCs was only about 0.28 volume fraction. This value is far below the 0.62, of random close packed arrangement (of spheres) typical of non-flocculated systems. In the coarse particle MMCs the average SiC volume fraction in the bed was about 0.54. Such a lower SiC concentration in the final sediment of the fine particle MMCs suggests the particles may have settled as flocs. At the mild stresses in gravity settling, the particles would not tumble into a close-packed arrangement.

Possible flocculation of the particles may explain the observed behaviour of the transition zone A1 in the fine particle MMCs. Flocs in the system are most likely to be formed during the mixing process. Under the condition of continuous agitation at constant intensity experienced during mixing, a "dynamic equilibrium" would be established between floc formation and floc destruction and flocs would approach an average stable floc size, which increases as particle concentration increases [6, 25, 26]. In other words, given enough time, the suspension would be composed of flocs of the same size. Practically, the flocs are not of uniform size, however, the size range has been observed to be fairly narrow, (in fact, narrower than the particle size range) [22]. This

appears to explain why the size of the zone A1 in the fine particle MMCs is relatively smaller (than those observed in the coarse particle MMCs) although particle size distribution is wider in the finer particles than the coarse ones. The narrowness of the floc size distribution will be fixed by the particle size distribution and since particle size distribution is (theoretically) the same for all the fine particle MMCs, regardless of the SiC concentration, we should expect the floc size distribution to be the same for all these MMCs. This may be responsible for the little (or no) change in the size of the transition zone A1 which was observed in the MMCs of fine particles.

Time taken during mixing to reach "dynamic equilibrium" will depend on the particle concentration, the lower the concentration, the longer the time. Mixing times were identical in all the MMCs and the exceptionally wide A1 zone in the 2.5 vol% MMC may be attributed to inadequate mixing time for that particular concentration. For this relatively low particle concentration, we expect collision frequency to be comparatively low and therefore might have required much longer mixing time than was given during the experiment.

5.3 SETTLING RATE DATA

The possibility of flocculation among the fine particles settling in the aluminum melt is further reinforced by the fact that the settling data did not fit the usual Richardson-Zaki equation typical of non-flocculating systems. Flocs rather than particles, therefore, may be considered as the basic flow units in the system. The height

of the settled bed, used to estimate the floc volume fractions at the various SiC volume fractions, could not be determined with accuracy due to the opaque nature of the Al/SiC system. However, values obtained were reasonably consistent with SiC particle mass conservation calculations. The linear relationship between particle concentration and floc concentration is apparently in reasonable agreement with published data [22, 26]. The value of 2 obtained for the floc-solid coefficient means that, in a floc, the fraction of solid (by volume) is about 0.5 (i.e. ½). Thus, a floc is composed of about 50% solid and 50% liquid by volume.

A plot of the settling rate data as seen earlier on, has two distinct regimes. The data do give a straight line for floc concentrations between 0.12 and 0.41. The aggregate-floc coefficient, C_{AF} , estimated from the plot is about 2.4. This means that (unless the aggregates are confined and strongly compressed) the flocs seem to cluster in such a way that the floc fraction within an aggregate is about 0.41 (i.e. ~1/2.4) This means that for approximately floc volume fractions of less than 0.41 (0.2 volume fraction of particles) the aggregates are composed of about 40% flocs and 60% liquid by volume respectively. Beyond floc volume fraction of 0.41, the plot predicts zero settling rate. Thus, there appears to be a limiting volume fraction of flocs, and for that matter, a limiting volume fraction of SiC particles, above which no settling occurs. The limiting SiC volume fraction of about 0.2 (0.41 floc volume fraction) obtained in this work is in reasonable agreement with the value of between 0.15 and 0.20 obtained by Setargew et al [27] for 15 µm SiC particles in aluminum.

The diameter d_p, of the flows pores of displaced liquid was estimated at about

1.4 mm. Essentially, the d_p and the C_{AF} do not change with concentration because both are fixed by the inter-particle bonding intensity [22]. The straight line portion of the settling data occurs at high concentrations and the aggregates are most likely to be in the form of a network structure. As concentration decreases, the area available for flow of displaced liquid increases. Neither d_p nor C_{AF} should change, so the number of pores per unit area must increase. Eventually, at floc volume fraction less than about 0.20 (0.10 solid volume fraction), the suspicion is that the pores become so numerous that a continuous aggregate is no longer possible and settling rates increase above the line predicted by equation (48). The aggregates thus, settle individually in this regime.

It is seen that settling rates decrease more rapidly with increasing concentration in the first half of the settling data than the straight line portion of the plot (Figure 4.27). This rapid decrease in settling rates appears to be inconsistent with the observation [25] that the average stable floc/aggregate size increases with increasing concentration. However, it should be noted that the floc effective density (and for that matter that of the aggregates) decrease significantly with increasing size [29], and this together with the increase in floc/aggregate volume fraction resulting from increasing concentration will have an effect that counters and may even overwhelm the increase in settling rate due to the size increase. This may be responsible for the observed rapid decrease in the settling rates. The very high settling rate observed at 2.5 vol% SiC, then, could be explained that the flocs/aggregates (in this MMC), although, comparatively small may have had comparatively high effective density.

5.4 MODELLING OF SEDIMENTATION OF FINE SIC PARTICLES IN ALUMINUM

The modelling of the settling behaviour of fine SiC particles, $14\mu m$, in aluminum, unlike that of the coarse $90\mu m$ particles, may not be simple due to the fact that the settling behaviour of these fine particles cannot be classified as non-flocculating. Assuming a flocculated system, therefore, small clusters of the fine SiC particles (plus enclosed aluminum liquid) or flocs would form the basic flow units in the settling process. These flocs attract themselves to form aggregates whose size is not a fundamental property of the system but grow by collision of the flocs and break down by action of shear forces. In any case, properties such as aggregate size, settling rates, and sediment volume fraction of the settling system, are controlled by,

- (i) floc volume fraction and,
- (ii) the strength of the attractive forces between flocs.

Therefore, modelling of the settling behaviour will rest heavily on the ability to quantify these two variables.

The model presented by Michael and Bolger for the settling of flocculated aqueous systems, well correlates the settling rates, of the fine SiC particles in aluminum, with floc volume fraction at high volume fraction of particles where the aggregates are most likely to settle together as a coherent network. Just beyond the "dilute" range, however, the experimental data deviates considerably from predictions of the model. Modelling of the settling behaviour of the fine SiC particles beyond the dilute range, therefore, may be handled separately for these two regimes.

5.5 FUTURE WORK

The overall objective of this work is to gain an understanding into the settling behaviour of fine SiC particles in liquid aluminum as it occurs during the processing of Al/SiC MMCs. Various precautionary measures were taken to reduce errors in the results as much as possible. Further measures are recommended to enhance the accuracy of any future work.

- Frequent replacement of the tungsten wires to reduce the influence of possible oxidation of the wires on the results.
- 2. Further reduction in the size of probe (base) if such a reduction can be achieved without sacrificing probe efficiency and/or sensitivity.

The experimental results, so far, indicate that the settling of the fine SiC particles in aluminum do not exhibit non-flocculating behaviour. Flocculating behaviour, therefore, has been assumed, based on the fact that the final bed has a density of only about 0.28 particle volume fraction and the agreement of the settling rate data at high SiC volume fractions with the Michael and Bolger's model for flocculated systems. It must be emphasized that this work is only the beginning of efforts to understand the settling of fine SiC particles in aluminum and so more work is needed to confirm these findings. The completely different settling behaviours exhibited by the coarse and the fine particles suggests that particle size has a strong influence in determining whether or not a system would flocculate (at least in the case of SiC particles in aluminum). However, there may be other contributing factors which might have been enhanced in the presence of the fine particles.

5.5.1 Settling Rates

The theory used in the analysis of the experimental results was proposed specifically for aqueous systems and based on the assumption that the diameter of the flow pores d_p and the aggregate floc coefficient C_{AF} remain constant. In the aluminum silicon carbide system, wetting of the particles by the aluminum melt is poor and time dependent and therefore has the potential to alter the inter particle bonding intensity and for that matter d_p and C_{AF}. The long mixing times during the experiments was a measure to ensure that wetting stabilized before the settling process began. In the DURALCAN process wetting stabilizes after about ninety (90) minutes of mixing. It is believed that the reinforcement particles in the DURALCAN process undergo some from of surface treatment before incorporation into the metal melt to enhance wettability. Comparison of the result of this work with settling data of DURALCAN MMCs should be of prime interest in any future work. This will help establish whether wetting was adequate in this work. Inadequate wetting can promote clustering of the particles and such a comparison can help to trace the source of the flocculation behaviour that was observed.

5.5.2 The Transition Layer

The presence of the transition region in the settling behaviour has been assumed to be caused by the floc or aggregate size distribution, which in a way may be traced from particle size distribution. Hanumanth et al [24] established in the case of the coarse

particle size distribution can give rise to such a transition layer, but their prediction as to how the size of the layer varies with SiC concentration in the MMC, was contrary to experimental observation. It is necessary to investigate this independently for the fine particles, because the possibility of clustering of these particles adds a new dimension to the problem. The role of particle size distribution in this may be investigated experimentally, by studying the settling of uniformly (or narrowly distributed) sized 14µm SiC particles in aluminum and compared with results of this work.

CHAPTER 6

SUMMARY AND CONCLUSION

The study of the settling of fine SiC particles during the processing may be summarised and concluded as follows;

- The settling of fine SiC particles in aluminum does not obey the Richarson-Zaki relation, characteristic of non-flocculated systems.
- (2) Two distinct settling regimes could be identified, a rapidly decreasing settling rate regime and a linear (less rapid decreasing settling rate) regime.
- (3) Concentration of SiC in final settled bed is very low, only about 0.28 as against 0.62 volume fraction, for random close packed arrangement characteristic of non-flocculated systems.
- (4) The fine SiC particles possibly exhibit an appreciable level of flocculation or clustering in aluminum.
- (5) At high volume fractions of SiC, the aggregate most likely settle as a coherent network structure and at much lower SiC volume fractions, settle as individual floc/aggregates.

REFERENCES

- 1. D.L. McDanels: *Metall. Trans.* **16A** (1985) 1105
- 2. T.G. Nieh: *Metall. Trans.* 15A (1984) 139.
- 3. J.K. Shang, W. Yu and R.O. Ritchie, Mat. Sci & Eng. 102A (1988) 181-192.
- 4. Processing of Ceramic and Metal Matrix Composites (Ed) H. Mostaghaci, CIM
 Conference of Metallurgists, Aug. 20-24, 1989, Pergamon Press, New York.
- 5. G.S. Hanumanth and G.A. Irons: Mixing and Wetting in Metal Matrix

 Composite Fabrication. In: Fabrication of Particulate Reinforced Metal

 Composites. (Ed.) J. Masonunave and F.G. Hamel, ASM Int., Ohio, (1990) 41.
- 6. M. Mada and F. Ajersch, Thixotropic effects in Semi-Solid Al-6%Si Alloy Reinforced with SiC Particles. In: Metal and Ceramic Matrix Composites; Processing, Modelling and Mechanical Behaviour. (Ed.) R.B. Bhagat, A.H. Clauer, P. Kumar and Ritter. The Minerals, metals and Materials Society, (1990) 337-350.
- 7. S. Lafreniere and G.A. Irons: *Int. Symp. on Production, Refining, Fabrication and Recycling of Light Metals*, Hamilton, ON, Canada, (Aug. 1990) 177-86.
- 8. C.S. Robinson, *Industr. Engng. Chem.*, 18 (1926) 869.
- 9. H.H. Steinour, *Industr. Engng. Chem.*, 36 (1944) 618.
- P.G.W. Hawksley, Symposium, "Some Aspects of Fluid Flow". Edward Arnold
 & Co., London.
- 11. G.J. Kynch: Trans. Faraday Soc., 48 (1952) 166-176.
- 12. G.B. Wallis: Symp. on Interactions between Fluids and Particles, Institute of

- Chemical Engineers, London, 9 (1962) 9-16.
- 13. J.F. Richardson and W.N. Zaki: Trans Inst. Chem. Eng., 32 (1954) 35-53.
- 14. B.V. Deryagin and L.D. Landau: Acta Physicochim. URSS, 14 (1941) 633.
- 15. E.J. Verwey and J.Th.G. Overbeek: *Theory of Stability of Lyophobic Colloids*, Elsevier, Amsterdam (1948).
- 16 H.C. Hamaker: *Physica*, 4 (1937) 1058.
- 17. M. Smoluchowski: Z. Phys. Chem. 92 (1917) 129.
- 18. T.R. Camp and P.C. Stein: J. Boston Soc. Civ. Eng. 30 (1943) 219.
- 19 J.L. Cleasby: J. Environ. Eng. 110 (1984) 875.
- 20 J. Gregory: Critical Rev. Environ. Control 4 (1989) 185-230.
- 21. N.H.G. Penners and L.K. Koopal: Colloids & Surf. 28 (1987) 67.
- 22. A.S. Michaels and J.C. Bolger: Ind. Eng. Chem. Engrs. 32, (1954) 24-33.
- 23. A.M. Gaudin and M.C. Fuerstenau: Eng. Mining J., 159 (1960) 110.
- 24. G.S. Hanumanth, G.A. Irons, and S. Lafreniere: *Metall. Trans.* **23B**, (1992) 753-763.
- 25. I. Reigh and R.D. Vold: J. Phys. Chem. 63 (1957) 1497.
- 26. S.G. Mason: Pulp and Paper Mag. Canada 49 (1948) 13.
- 27. N. Setragew, B.A. Parker and M.J. Couper: *Proc. of Advanced Composites '93*, Wollongong, Australia (Feb. 1993).
- 28. N. Tambo and Y. Watanabe: Water Research, 13 (1979) 409-419.

APPENDIX I MICROGRAPHS OF MMCs

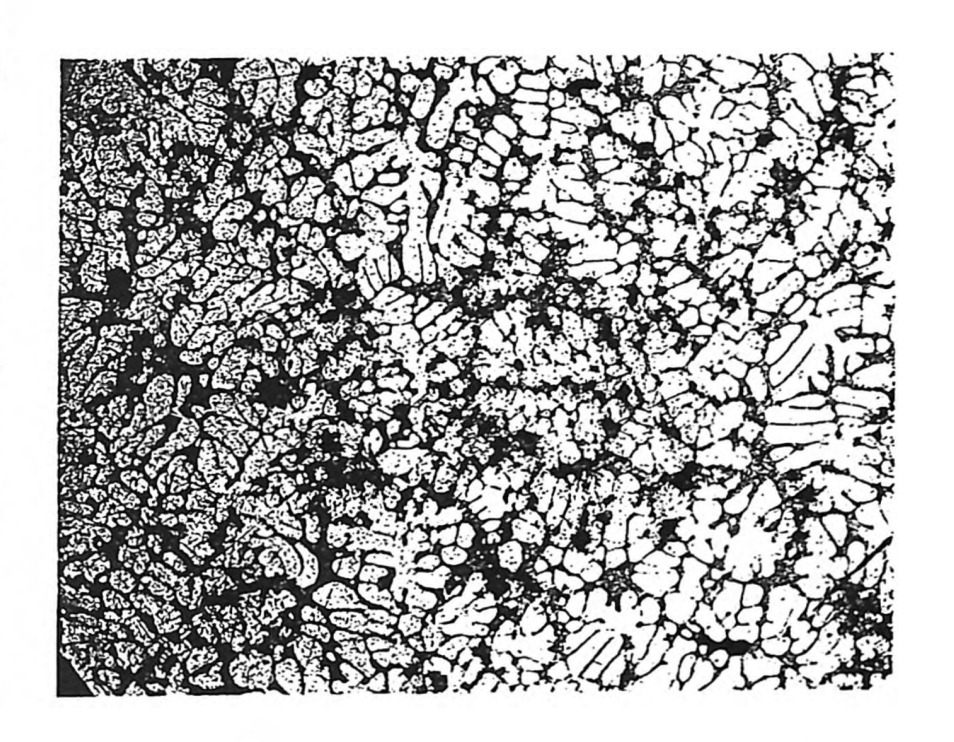


Figure I.1 Micrograph of 2.5 vol% SiC MMC (× 64).

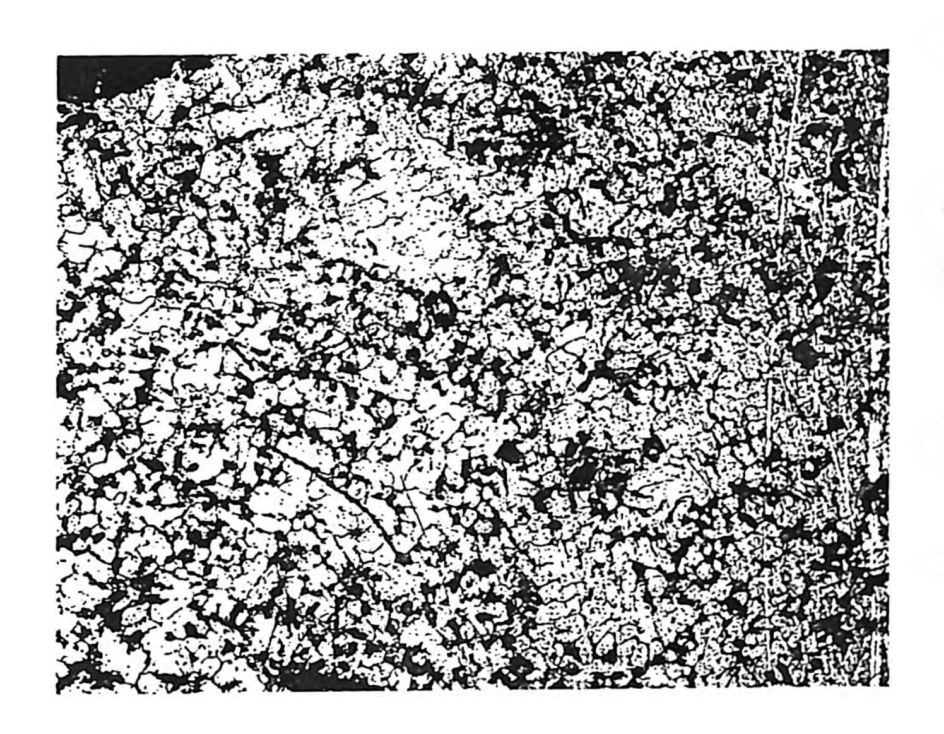


Figure I.2 Micrograph of 5 vol% SiC MMC (× 64).

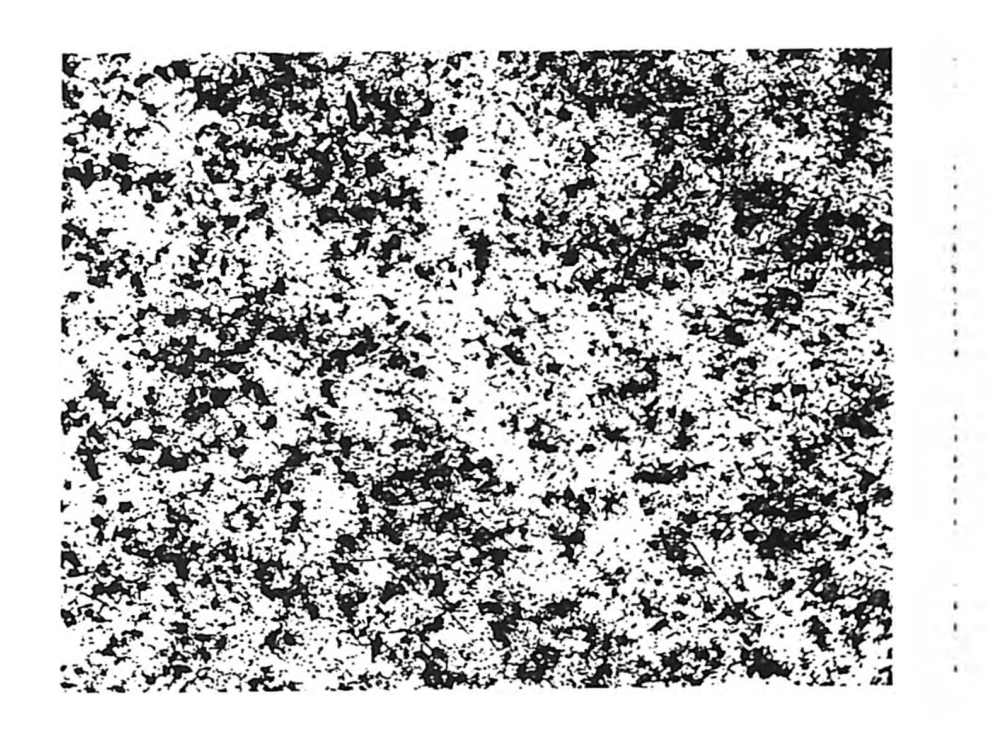


Figure I.3 Micrograph of 7.5 vol% SiC MMC (× 64).

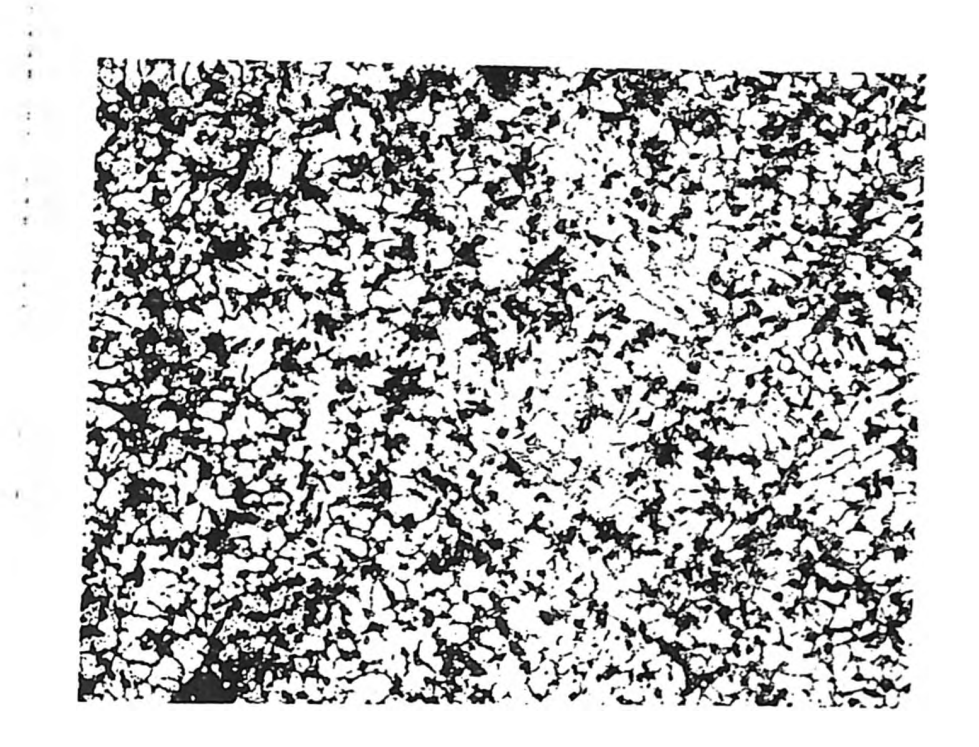


Figure I.4 Micrograph of 10 vol% SiC MMC (× 64).

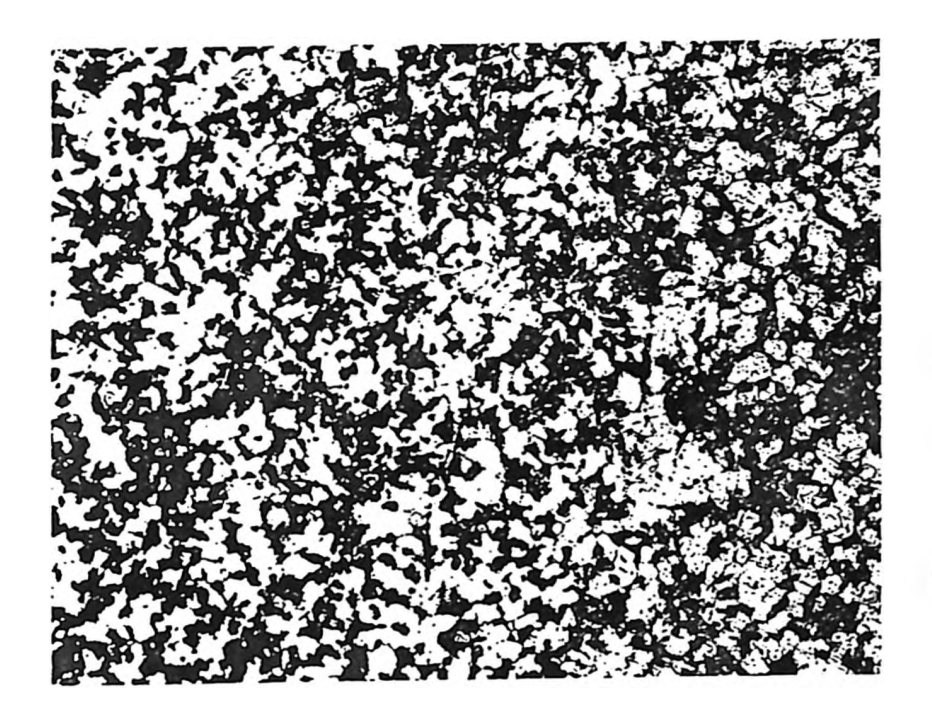


Figure I.5 Micrograph of 15 vol% SiC MMC (× 64).

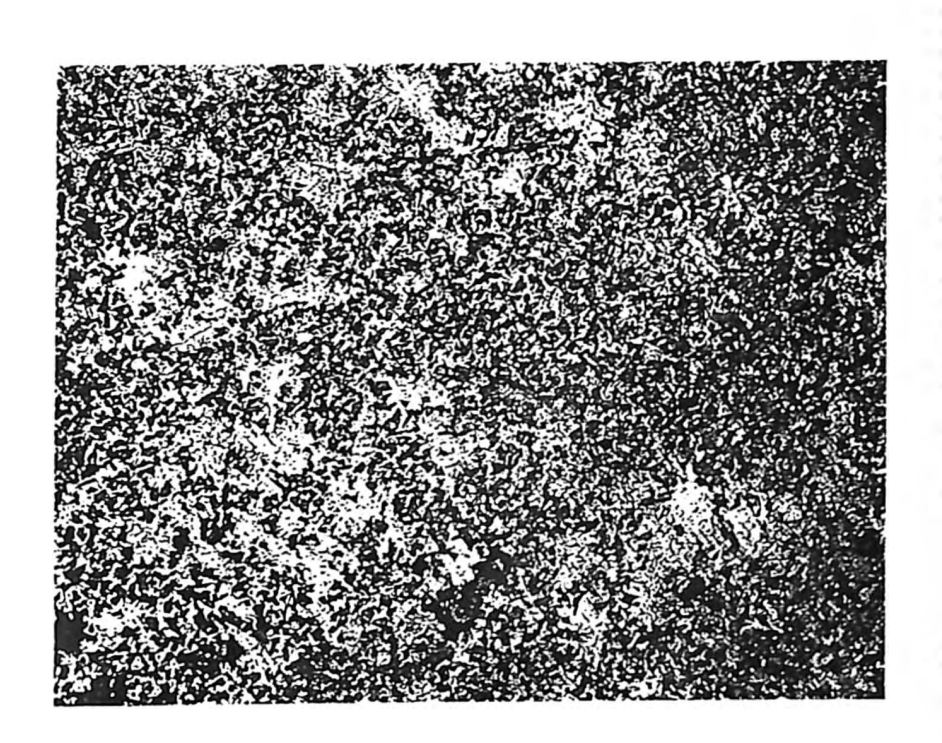


Figure I.6 Micrograph of 20 vol% SiC MMC (× 64).

APPENDIX II

II.1 POISEUILLE EQUATION

The Poiseuille equation or Hagen-Poiseulle law governs laminar flow in circular pipes. Figure II.1 shows, on the left side, a straight pipe of constant internal radius R and on the right is shown the circular cross-section. For laminar flow, the path of individual particles of fluid do not cross, and so the pattern of flow may be imagined as a number of thin concentric cylinders sliding over one another. The diagram shows a cylinder, of radius, r, moving from left to right with velocity u inside a slightly larger cylinder of radius, $r + \delta r$, moving in the same direction with velocity $u + \delta u$ (δu may of course be negative).

A stress will exist along the two layers of fluid due the difference of velocity between the two cylinders. At steady state flow the shear stress, τ , at radius, r, is given by:

$$\tau = \frac{r}{2} \frac{dp*}{dx} \tag{II.1}$$

where $p^* = p + \rho gz$, the piezometric pressure. In laminar flow the stress is purely due to viscous action and so is given by the equation which defines the coefficient of viscosity:

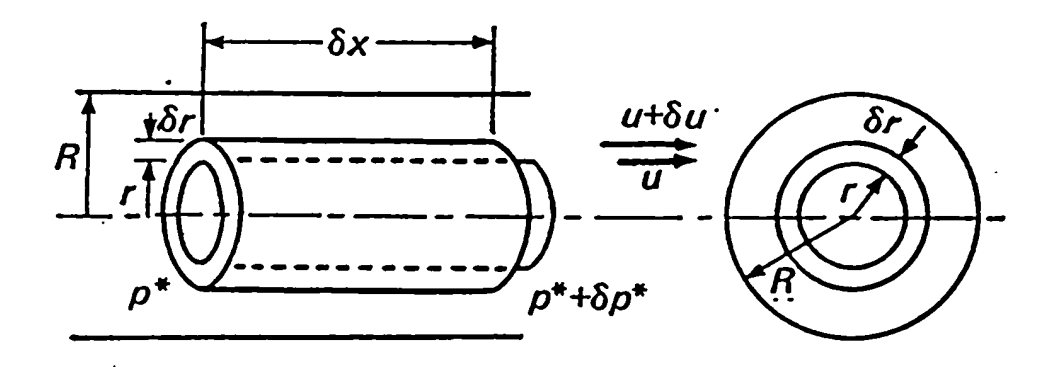


Figure II.1 Cylinder of radius r, moving inside a slightly larger cylinder of radius $r + \delta r$.

$$\tau - \mu \frac{\partial u}{\partial r} \tag{II.2}$$

As flow is steady and "fully developed" the velocity varies only with the radius, therefore the partial derivative may be written as a full derivative. Thus,

$$\mu \frac{du}{dr} - \frac{r}{2} \frac{dp*}{dx} \qquad i.e. \quad \frac{du}{dr} - \frac{r}{2\mu} \frac{dp*}{dx}$$
 (II.3)

If μ is constant, intergration with respect to r gives

$$u = \frac{r^2}{4\mu} \frac{dp^*}{dx} + A. \tag{II.4}$$

Now the constant of intergration A is determined from the boundary conditions. As there is no slip at the wall of the pipe, u = 0 where r = R. Consequently, A, must have the value $-(R^2/4\mu)(dp^*/dx)$ so the velocity at any point is given by,

$$u = -\frac{1}{4u} \frac{dp*}{dx} (R^2 - r^2)$$
 (II.5)

(Since p* falls in the direction of flow, dp*/dx is negative).

The discharge δQ through the annular space between radii r and r + δr is (velocity × perpendicular area) = u × $(2\pi \delta r)$.

$$\delta Q = -\frac{1}{4\mu} (\frac{dp*}{dx}) (R^2 - r^2) 2\pi r \delta r = -\frac{\pi}{2\mu} (\frac{dp*}{dx}) (R^2 r - r^3) \delta r$$
 (II.6)

The discharge across the entire tube is therefore,

$$Q = -\frac{\pi}{2\mu} \left(\frac{dp*}{dx}\right) \int_0^R (R^2r - r^3) dr$$

or,

$$Q = -\frac{\pi}{2\mu} \left(\frac{dp*}{dx}\right) \left(R^2 \frac{R^2}{2} - \frac{R^4}{4}\right) = -\frac{\pi R^4}{8\mu} \left(\frac{dp*}{dx}\right)$$
(II.7)

For a length 1 of pipe over which the piezometric pressure drops from p_1^* to p_2^* the equation may be written as

$$Q = \frac{\pi R^4}{8\mu l} (p_1 *^2 - p_2 *^2)$$
 (II.8)

The equation applies to both incompressible and compressible fluids since it concrens only an infinitesimal length δx of pipe and any change in density of fluid in this distance would be negligible.

II.2 KOZENY-CARMAN EQUATION

The relation deals with flow of fluids through porous materials. Under such conditions the velocity is usually so small and the flow passages so narrow that laminar flow may be assumed without any hesitation. Rigirous analysis of the the flow is not possible because the shape of the individual flow passages is so varied and so complex. Henry Darcy (1803-58) deduced that the steady mean velocity u in such a flow to be, where x refers to the average direction of flow, $\partial p^*/\partial x$ represents the rate of increase of

$$\overline{u} - C \frac{\partial p *}{\partial x} \tag{II.9}$$

piezometric pressure in this direction, and C is a constant at a given temperature for a particular fluid (free from suspended solid particles) and for the piece of porous medium concerned.

The value of C depends not only on the viscosity of of the fluid but also on the size and geometrical arrangement of the solid particles in the porous material. Josef Kozeny (1889-1967), in an attempt to predict a more precise expression for C, considered the porous material to be made up of separate small solid particles, and the flow to be, broadly speaking, in one direction only: thus, although the fluid follows a somewhat tortous path through the material, there is no net flow across the block of material in any direction other than (say) the x direction. Whatever the actual shape of the individual flow passages the overall result is the same as if, in place of the porous material, there were a large number of parallel, identical capillary tubes with their axes in the x direction. He then reasoned that, since the resistance to flow results from the requirement of no slip at any solid boundary, the capilary tubes and the porous medium be truely equivalent, only if, for a given volume occupied by the fluid, the total surface area of the solid boundaries were the same in each case.

The voidage or porousity, ε , is given by,

$$\varepsilon = \frac{Volume \ of \ voids}{Volume \ of \ voids + Volume \ of \ solids} = \frac{V_{v}}{V_{v} + V_{s}}$$
 (II.10)

whence

$$V_{\nu} = \frac{V_{s} \varepsilon}{(1 - \varepsilon)S} \tag{II.11}$$

Therefore

$$\frac{Volume \ of \ void}{Total \ surface \ area} = \frac{V_{\nu}}{S} = \frac{V_{s} \varepsilon}{(1 - \varepsilon)S}$$
 (II.12)

The corresponding value for a capillary tube of internal diameter d and length 1 is $(\pi/4)d^2l/\pi dl = d/4$. Thus if the set of capillary tubes is to be equivalent to the porous medium then each must have internal diameter,

$$d = \frac{4V_s \varepsilon}{1 - \varepsilon)S} \tag{II.13}$$

Now if all the flow passages in the porous material were entirely in the x direction, the mean velocity of the fluid in them would be u/ε (because only a fraction of the total cross-section is available for flow). The actual paths, however, are sinuous and have an average length l_ε which is greater than l_ε , the thickness of the porous material. Philip C. Carman (1907-) later pointed out that the mean velocity in the passages is therefore greater than if the passage were straight, and given by $(u/\varepsilon)(l_\varepsilon/l)$. Flow at this mean velocity in capilary tube would require a drop of piezometric pressure Δp^* given by Poiseuille equation (II.8):

$$\frac{\Delta p *}{l_{e}} - \frac{32\mu}{d^{2}} \frac{Q}{\pi d^{2}/4} - \frac{32\mu}{d^{2}} \frac{\overline{u}}{\epsilon} \frac{l_{e}}{l}$$
 (II.14)

Rearranging equation (II.14) and substituting equation (II.13) yields

$$\overline{u} - \frac{\Delta p *}{l_e} \frac{\varepsilon d^2}{32\mu} \frac{l}{l_e} - \frac{\Delta p *}{l} \frac{\varepsilon^3}{(1-\varepsilon)^2} \frac{V_s^2}{2\mu S^2} \frac{l^2}{l_e^2}$$
 (II.15)

$$\overline{u} = \frac{\Delta p * \varepsilon^3}{l} \frac{\varepsilon^3}{(1 - \varepsilon)^2} \frac{1}{\mu k (S/V_s)^2}$$
 (II.16)

where $k = 2(l_e/l)^2$. Equation (II.16) is known as the Kozeny-Carman equation and k as the Kozeny constant function.